Public Interest Energy Research (PIER) Program FINAL PROJECT REPORT

APPLICATION OF INSAR TO THE DETECTION OF SURFACE DEFORMATION IN THE GEOTHERMAL FIELDS OF IMPERIAL VALLEY, CALIFORNIA

Prepared for: California Energy Commission

Prepared by: Imageair, Inc.

MARCH 2010 CEC-500-2010-019

Prepared by:

Primary Author: Mariana Eneva PUBLIC INTEREST ENERGY RESEARCH
"Research Powers the Future"

Imageair, Inc. 10513 Caminito Westchester San Diego, CA 92126

Contract Number: PIR-04-006

Prepared for:

California Energy Commission

Pablo S. Gutierrez Contract Manager

Laurie ten Hope

Deputy Director

RESEARCH AND DEVELOPMENT DIVISION

Robert P. Oglesby Executive Director

DISCLAIMER

This report was prepared as the result of work sponsored by the California Energy Commission. It does not necessarily represent the views of the Energy Commission, its employees or the State of California. The Energy Commission, the State of California, its employees, contractors and subcontractors make no warrant, express or implied, and assume no legal liability for the information in this report; nor does any party represent that the uses of this information will not infringe upon privately owned rights. This report has not been approved or disapproved by the California Energy Commission nor has the California Energy Commission passed upon the accuracy or adequacy of the information in this report.

Acknowledgements

The following individuals and organizations have made significant contributions to this project:

Giacomo Falorni, Brian Young (TRE Inc., Canada): PSInSAR™ analysis of RADARSAT data.

Jacopo Allievi, Fabrizio Novali (TRE Italy): PSInSAR™ analysis of RADARSAT data.

Agram Piyush Shanker (graduate student from the InSAR group at Stanford University, supervisor Prof. Howard Zebker): PS InSAR analysis of ERS and ENVISAT ASAR data, SBAS analysis of ENVISAT ASAR data.

Dr. Robert Mellors (Dept. Geology, San Diego State University): DInSAR analysis of ALOS PALSAR data.

Dr. David Adams (Imageair, Inc.): Matlab codes for comparing InSAR results with leveling measurements.

Brian Berard (CalEnergy): provided proprietary reports and digital leveling data from the Salton Sea geothermal field.

Charlene Wardlow, Erik Osbun (Ormat): provided proprietary reports on leveling performed at the Heber geothermal field.

ESA (European Space Agency): approved Category-1 research data proposal for 205 ENVISAT ASAR scenes, which made it possible to download these data at a low cost.

ASF (Alaska Satellite Facility): approved a research data proposal for 60 RADARSAT scenes, which were made available at no cost to this project.

Please cite this report as follows:

Eneva, Mariana 2009. Application of InSAR to the Detection of Surface Deformation in the Geothermal Fields of Imperial Valley, California. California Energy Commission, PIER Program. CEC-500-2010-019.

Preface

The California Energy Commission's Public Interest Energy Research (PIER) Program supports public interest energy research and development that will help improve the quality of life in California by bringing environmentally safe, affordable, and reliable energy services and products to the marketplace.

The PIER Program conducts public interest research, development, and demonstration (RD&D) projects to benefit California.

The PIER Program strives to conduct the most promising public interest energy research by partnering with RD&D entities, including individuals, businesses, utilities, and public or private research institutions.

PIER funding efforts are focused on the following RD&D program areas:

- Buildings End-Use Energy Efficiency
- Energy Innovations Small Grants
- Energy-Related Environmental Research
- Energy Systems Integration
- Environmentally Preferred Advanced Generation
- Industrial/Agricultural/Water End-Use Energy Efficiency
- Renewable Energy Technologies
- Transportation

"Application of InSAR to the Detection of Surface Deformation in the Geothermal Fields of Imperial Valley, California" is the final report for the project "Application of InSAR to the Monitoring and Mitigation of Surface Subsidence from Increased Geothermal Development in the Imperial Valley, CA," Project Contract Number GEO-05-004, Work Authorization Number PIR-04-006 conducted by Imageair, Inc. The information from this project contributes to PIER's Renewable Energy Technologies Program.

For more information about the PIER Program, please visit the Energy Commission's website at www.energy.ca.gov/research/ or contact the Energy Commission at 916-654-4878.

Table of Contents

Preface
Abstract
Executive Summary
1.0 Introduction
1.1 Geothermal Fields in the Imperial Valley
1.2 Sources of Surface Deformation in Imperial Valley
1.3 SAR Interferometry – Definitions and Techniques
1.4 Previous Applications of InSAR to the Detection of Surface Subsidence
in Geothermal Fields
2.0 Project Methods
3.0 Project Results
3.1 Ground-Based Measurements in Imperial Valley
3.1.1 Leveling Measurements in the Geothermal Fields
3.1.2 GPS Measurements and Their Comparison With the Leveling
Data
3.2 Results From C-band RADARSAT Data
3.2.1 Methodology
3.2.2 SAR Data Selection
3.2.3 Master Image Selection
3.2.4 Phase and Amplitude Analysis
3.2.5 Estimation of the Atmospheric Effects
3.2.6 Post-Processing
3.2.7 PS Results
3.2.8 Summary of the Characteristics of the Study
3.2.9 Precision Assessment.
3.2.10 Sensitivity Versors
3.2.11 Observations
3.2.12 West-East and Vertical Movement Decomposition
3.2.13 Comparison with Leveling Data
3.3 Results from C-band ENVISAT Data (ASAR)
3.3.1 Results From the Application of the PSI Technique
3.3.2 Results From the Application of the SBAS Technique
3.4 Results from L-band PALSAR (ALOS Satellite)
3.4.1 DInSAR Method
3.4.2 Results
3.5 Potential of L-Band UAVSAR
4.0 Conclusions and Recommendations
5.0 References
Appendices (A-D)

List of Figures

Figure 1-1. Two satellite images showing study area (ASTER VNIR Level 1B)7-8
Figure 1-2. Map of the western U.SMexico border region
Figure 1-3. The epicenter location of the 2005 M5.1 earthquake shown on an ASTER optical image
Figure 3-1. Map of the greater area around the Salton Sea geothermal field (SSGF)20
Figure 3-2. Histogram of the vertical deformation rates derived from the benchmark leveling data, referenced to S-1246.
Figure 3-3. Spatial distribution of deformation rates from the leveling data relative to S-1246
Figure 3-4. Map with the locations of the GPS locations (http://sopac.ucd.edu)
Figure 3-5. Map showing the vectors of horizontal velocities in the study area (green arrows. Adapted from http://sopac.ucsd.edu
Figure 3-6. Model of possible horizontal tectonic movements at the benchmark locations in the W-E direction, relative to S-124625
Figure 3-7. (a) Filtered position time series for station P507. (b) Filtered and detrended time series of surface deformation from (a). From http://sopac.ucsd.edu
Figure 3-8. The Salton Sea area of interest (yellow outline) as seen from Google Earth
Figure 3-9. RADARSAT-1 satellite coverage of the study area by the ascending orbit (track 52) and descending orbit (track 116) imagery
Figure 3-10. Ascending orbit multi-image reflectivity (MIR) map of the Salton Sea area.
Figure 3-11. Descending orbit multi-image reflectivity (MIR) map of the Salton Sea area.
42

Figure 3-12. Detail of the study area as seen from an orthophoto, highlighting the high resolution of the imagery
Figure 3-13. Locations of the ascending (pink circle) and descending (green circle) orbit reference points and the reference benchmark S-1246 (red triangle)
Figure 3-14. Ascending orbit PS velocity map. The red triangle shows the location of the S-1246 reference benchmark
Figure 3-15. Descending orbit PS velocity map. The red triangle shows the location of the S-1246 reference benchmark
Figure 3-16. Ascending orbit PS elevations referenced to mean sea level
Figure 3-17. Descending orbit PS elevations referenced to mean sea level
Figure 3-18. Ascending orbit PS velocity standard deviation. Values are in mm/yr 44
Figure 3-19. Descending orbit PS velocity standard deviation. Values are in mm/yr45
Figure 3-20. Results of the PS alignment on a 50-cm orthophoto image46
Figure 3-21. Use of PS height information to determine if a PS is on the ground or at the top of a building. Red PS are located at the base of the structure, blue PS are higher up
Figure 3-22. Diagram illustrating the satellite acquisition geometry. See Table 3-2-8 for the actual values of the angles
Figure 3-23. The PS points on the east side of the image seem to be located in an agricultural field
Figure 3-24. Relatively high density of PS likely due to fallow fields52
Figure 3-25. Time series of a PS near the centre of the study area that is moving downwards
Figure 3-26. Standard deviation of PS velocity (ascending data) near the reference point (green circle), close to the S-1246 benchmark (red triangle)53

Figure 3-27. Standard deviation of PS velocity (descending data) near the reference point (pink circle), close to the S-1246 benchmark (red triangle)54
Figure 3-28. W-E component of the deformation. Positive (blue) values indicate eastward movement, while negative (red) values indicate westward movement
Figure 3-29. Comparison of the leveling data at benchmarkUG-80 and the surface deformation registered at ascending PS points within (a) 100 m and (b) 200 m from the benchmark
Figure 3-30. Same as Fig. 3-29, but with the descending PS points within 100 m from UG-80. This is very similar to the plot with PS within 200 m (not shown)
Figure 3-31. Projection of the leveling data (red triangles) onto RADARSAT LOS (red and blue lines). The numbers marking the different curves indicate hypothetical horizontal W-E movements in mm/yr, with positive numbers for movements to the east and negative numbers for movements to the west
Figure 3-32. Differences between the leveling rates projected onto the LOS and the deformation rates of the PS points within 200 m from benchmarks. These differences are indicative of W-E horizontal movements
Figure 3-33. Footprints of the ASAR scenes superimposed on GoogleEarth imagery. The descending footprints (tracks 84 and 356) are shown with pink rectangles. The ascending footprints (tracks 77 and 306) are shown with blue rectangles. The outlines of the Salton Sea (SSGF), Heber (HGF) and East Mesa (EMGF) geothermal fields are shown with light blue. Yellow line shows the border between the USA and Mexico. The large water body is Salton Sea
Figure 3-34. Examples of browse images from ASAR scenes from all available tracks - descending 84 and 356 and ascending 77 and 306. Footprints of the scenes are shown in Fig. 3-33
Figure 3-35. Time series of individual interferograms used to extract the rates shown next in Fig. 3-36a
Figure 3-36. Surface deformation rates (mm/yr) in the LOS (line-of-sight) direction over the Salton Sea geothermal field, relative to S-1246 (yellow triangle). Colored points are permanent scatterers, PS

Figure 3-37. Example of subsidence measured at adjacent leveling benchmarks UG-70 and U-5, along with the nearest ENVISAT PS time series. Leveling data are also representative in the LOS direction due to the steep look angle (~22°)70
Figure 3-38. Time series of deformation (in mm) relative to S-1246). Horizontal axis is time measured in days since May 4, 2003. Benchmark observations are marked by triangles and descending PS measurements within 150 m of that benchmark are marked by lines and circles. Vertical lines mark the occurrence times of the M5.1 earthquake in September 2005 and associated fore- and aftershocks
Figure 3-39. Deformation rates for benchmarks (triangles) and descending PS (circles). Only PS locations with RMSE < 6 mm/yr are plotted. Black arrow points to a benchmark, whose deformation time series was shown in Figure 3-38
Figure 3-40. Projection of leveling data (red triangles) onto descending ENVISAT LOS (red and blue lines). The numbers marking the different curves indicate hypothetical horizontal W-E movements in mm/yr, with positive numbers for movements to the east and negative numbers for movements to the west
Figure 3-41. Comparison of the leveling data at benchmarkUG-80 and the SBAS ascending deformation time series within (a) 100 m and (b) 200 m from the benchmark. Refer to Fig. 3-40 for assumptions including horizontal movements
Figure 3-42. Same as Fig. 3-41, but for the descending orbits76
Figure 3-43. Maps of deformation rates at SBAS cells. Top – ascending, bottom – descending. Benchmarks are shown with triangles. Color scale marks LOS rates in mm/yr, referenced to S-1246.
Figure 3-44. Maps showing coverage of descending data (left - paths 532 and 533) and ascending data (right - paths 211, 21, and 215). Yellow triangles denote geothermal areas in Imperial Valley. The open triangle shows the location of the Cerro Prieto geothermal field in Mexico
Figure 3-45. Left - Full unwrapped and masked interferogram (unwrapped phase) with the strongest signal observed. Subsidence signals associated with both East Mesa and Cerro Prieto in Mexico are clearly visible. Strong decorrelation exists over the vegetated areas, except for narrow streaks that are aligned with field edges, possibly associated with canals and streets

igure 3-46. Image centered on the Heber geothermal field. The wrapped phase shows
ossible indications of subsidence, but it is not obvious in the unwrapped LOS signal,
kely due to unwrapping difficulties in areas with isolated phase
igure 3-47. Interferogram covering the Salton Sea geothermal area. This area is particula
difficult to image due to rapid decorrelation over time. Farm fields seem to display
arying elevations in images with correlation, possibly due to vegetation growth or var
ations in soil moisture8
igure 3-48. Example of UAVSAR coverage of Salton Sea from May 3, 2008. Yellow rec-
angle shows study area. Flight Line ID 22001
ttp://uavsar.jpl.nasa.gov/flightplans/mar0308/8



List of Tables

Table 1-1. Parameters of satellites with SAR capabilities
Table 3-1-1. GPS deformation rates (in mm/yr) around the Salton Sea geothermal field (H- horizontal component relative to the Pacific Plate, V-vertical component)23
Table 3-1-2. Decomposition of the horizontal velocities at three PBO GPS stations25
Table 3-2-1. RADARSAT-1, track 52, ascending orbit scenes used in the analysis. Bn = normal baseline; Bt = temporal baseline. The image highlighted in red was used as the "master" image in the processing?
Table 3-2-2. RADARSAT-1, track 116, descending orbit scenes used in the analysis. Bn = normal baseline; Bt = temporal baseline. The image highlighted in red was used as the "master" image in the processing?
Table 3-2-3. Summary of output from the ascending orbit data?
Table 3-2-4. Summary of output from the descending orbit data?
Table 3-2-5. Measurement accuracies for PS located within 2 km from the reference point, based on the processing of at least 45 SAR images30,43
Table 3-2-6. Components of the ascending orbit RADARSAT-1 LOS versor for this study31,48
Table 3-2-7. Components of the descending orbit RADARSAT-1 LOS versor for this study
Table 3-2-8. Satellite viewing angles for both orbit geometries
Table 3-3-1. Parameters of SAR scenes used in the PSI analysis
Table 3-3-2. Factors describing the difference between leveling and PS rates72
Table 3-4-1. Primary ALOS data used in the study (A and D – ascending and descending orbits, respectively)
Table 3-4-2. Interferograms generated

Abstract

This final report presents results from the analysis of satellite radar data collected over the geothermal fields in the Imperial Valley, Southern California. Interferometric synthetic aperture radar (InSAR) techniques were used to detect surface deformation caused by geothermal fluid extraction. The data used were from the Canadian RADAR-SAT, European ENVISAT, and the Japanese ALOS satellites. Shorter wavelength (5.6 cm, so-called C-band) is used by the SAR instruments on the first two satellites, and a longer wavelength (23.6 cm, L-band) is used on the third satellite. The conventional InSAR method for identifying surface displacements is differential InSAR. When applied to Cband data, differential InSAR is only effective in relatively dry and non-vegetated areas, because short wavelengths do not penetrate vegetation effectively. For this reason, due to the agricultural fields covering some of the geothermal fields in Imperial Valley, the project focused on using newer InSAR techniques, such as PSI (permanent scatterers interferometry) and (small-baseline subsets), that were expected to work better with shortwavelength (C-band) data over vegetated areas. The results from the application of a specific PSI technique, PSInSAR TM , to the RADARSAT C-band data are in very good agreement with ground-based leveling measurements provided by CalEnergy for the Salton Sea geothermal field. Since longer wavelengths (L-band) are expected to penetrate vegetation, conventional differential InSAR was used with the ALOS L-band data. However, signals were detected only in geothermal fields not covered with vegetation. In view of these results, the PSI approach is strongly recommended for future monitoring of subsidence in the vegetated areas of Imperial Valley. PSI has the potential for costeffective multi-temporal coverage (up to \sim 10 times per year), providing information on both the vertical and horizontal components of deformation, whereas the leveling surveys capture only vertical movements, and only once per year.

Keywords: Subsidence, geothermal, InSAR, permanent scatterers, radar interferometry, surface deformation, Salton Sea, environmental impact, mitigation, Imperial Valley, Imperial County, Southern California



Executive Summary

Introduction

Satellite interferometric synthetic aperture radar techniques have been known for some time now to be very effective in detecting surface deformation. Synthetic aperture radar imagery used for this purpose has included short-wavelength data (~5.6 cm, or C-band) from the European satellites ERS-1, ERS-2 and ENVISAT, and from the Canadian satellite RADARSAT-1. Longer wavelength data from the Japanese satellites JERS-1 and ALOS (~23.6 cm, or L-band) have also been used. This is a remote sensing technique that uses radar satellite images. Radar satellites such as Ees-1, Ees-2, JERS-1, and so forth, constantly shoot beams of radar waves towards Earth that are documented after they're bounced off Earth's surface. As these waves bounce off Earth they provide information that can be used to obtain elevation or surface change.

The first conventional method developed for detection of surface deformation was differential interferometric synthetic aperture radar. In ideal conditions this type of satellite imagery is very sensitive and can detect changes at a very small scale to within a millimeter. If shorter-wavelength (C-band) data are used, differential interferometric synthetic aperture radar works only in relatively dry, non-vegetated areas. The longer wavelength (L-band) is expected to penetrate vegetation better, so L-band differential interferometric synthetic aperture radar offers greater hope for vegetated areas.

Recent advances in interferometric synthetic aperture radar resort to so-called *permanent* or *persistent scatterers*, hence these techniques are known as persistent scatters interferometry. The persistent scatterer points are usually man-made structures or exposed rocks that can be often identified even amidst vegetation. Thus compared with conventional differential interferometric synthetic aperture radar, the persistent scatters interferometry approach has much greater potential to extract information in vegetated areas, even when shorter-wavelength (C-band) data are used. The persistent scatters interferometry techniques make use of time series of synthetic aperture radar scenes to extract time series of surface deformation at the locations of the persistent scatters points. Deformation velocities, or deformation rates, can be further calculated from these observations (for example, in millimeters or centimeters per year). In ideal conditions, the persistent scatters interferometry estimates of deformation rates can achieve precision < 0.1 mm/year.

Other interferometric synthetic aperture radar innovations include the small baseline subsets techniques that may be also more effective in areas where conventional differential interferometric synthetic aperture radar fails.

The surface deformation detected by any interferometric synthetic aperture radar technique is first measured in the line of sight direction (line of sight to the satellite). Knowledge of the satellite orbit geometry, and especially when data from both descending and ascending orbits are available (instead of, satellite flies it the north-south or south-

north direction, respectively), makes it possible to infer vertical and horizontal components of the surface displacements.

Geothermal fluid extraction, that is, the associated injection and production, can and do result in surface changes or displacement. The surface displacements can be both vertical and horizontal. The vertical components can be uplift or sinking. Due to fluid extraction in geothermal areas, sinking is of primary concern. The currently operating geothermal fields in the Imperial Valley of Southern California (Salton Sea, Heber, and East Mesa) are no exception. Annual leveling measurements designed to capture the vertical movements (mostly settling) are conducted by the operators of these fields, CalEnergy and Ormat. Although measures are taken to reduce the possible environmental impact of surface changes, the intended increase of geothermal capacity in the near future may result in a larger effect on the surface. Thus it is important to devise precise and costeffective tools to monitor changes that go beyond the conventional ground-based leveling surveys. In this respect, interferometric synthetic aperture radar presents important opportunities in principle, but the extensive presence of agriculture in the area has been so far a deterrent to any routine applications using satellite data. This project looked to verify if any of the newer interferometric synthetic aperture radar techniques might yield results comparable with the measurements from the leveling surveys, and possibly even surpassing them. The results of this study unequivocally demonstrate that the PSI techniques are effective in this agricultural area and represent a viable tool to be extensively used in the future.

Purpose

This project was to find out if satellite synthetic aperture interferometry can be useful for the detection of surface changes resulting from the operation of the geothermal fields in the Imperial Valley of Southern California. This project is particularly important because planned increase in geothermal capacity in the area may require more attention to the potential environmental impact of the extraction of geothermal fluids and more aggressive mitigation efforts.

Project Objectives

Conventional differential interferometric synthetic aperture radar applied to short-wavelength C-band satellite synthetic aperture radar data was not expected to work in the geothermal fields covered by vegetation, so the focus was on evaluating the performance of more advanced techniques, such as persistent scatterers interferometry and small-baseline subsets. The differential interferometric synthetic aperture radar approach was used only with the longer-wavelength L-band data, which, unlike C-band, can penetrate vegetation. Comparisons with ground-based leveling measurements provided by the geothermal operators were used as the criteria to evaluate the outcome of the applications of the interferometric synthetic aperture radar techniques. In addition, the availability of satellite data from both ascending and descending orbits made it possible to detect both vertical and horizontal surface movements, while the ground-based

leveling surveys capture only vertical movements. Furthermore, comparisons with regional global positioning system measurements could be used to note tectonic changes in the geothermal fields.

Project Outcomes

The best results were obtained from the application of specific persistent scatterers interferometry technique; persistent scatterers interferometric synthetic aperture radar, to Cband RADARSAT-1 data collected over the Salton Sea geothermal field during a twoyear period (2006-2008). A total of 39 scenes were analyzed from both ascending (18) and descending (21) orbits, each providing ~10 measurements per year on average. During that same period, CalEnergy had two leveling surveys in the field at 79 benchmarks. Benchmarks are typically placed and maintained at various locations by the government or survey forms and are used to mark the exact elevation of a location. Leveling is the processes by which one determines the difference in elevation at two different benchmark locations. Several thousand persistent scatterers points were identified, at which the surface change rates were determined first in the line-of-sight direction (line-of-sight to the satellite), and then they were decomposed into vertical and west-east horizontal directions (or components). This was possible because the descending geometry of RA-DARSAT-1 was similarly sensitive to both components, while the ascending geometry was significantly more sensitive to the vertical than to the horizontal component. The persistent scatterers deformation rates within the vicinity of the 79 locations used by CalEnergy showed a very good agreement with the leveling measurements.

Furthermore, regional global positioning system measurements were used to infer marked tectonic movements, with significantly larger horizontal than vertical components. These tectonic movements represent the background on which sinking caused by geothermal fluid extraction are superimposed.

This analysis also made it possible to evaluate the assumption that a reference leveling benchmark, S-1246, used by CalEnergy in its leveling surveys in the Salton Sea geothermal field, does not move. For comparison, that same location was used as a reference for the PSI satellite measurements. However, the analysis performed in this project strongly indicates that this point actually subsides. Thus an observed uplift in some portions of the field was suggested to actually be settling occurring more slowly than the downward movement of leveling benchmark number S-1246.

Results from the application of another persistent scatterer interferometry technique and small-baseline subsets to the C-band data from the European Space Agency Environmental Satellite were more ambiguous. However, this was attributed to complexities and deficiencies of the application and not to intrinsic inferiority of either the type of synthetic aperture radar data or the particular persistent scatterer interferometry methods used in that case. Compared with the RADARSAT-1 data used in this project, the European Space Agency Environmental Satellite data covered a longer period, starting

in 2003, and continue to be collected over the Imperial Valley. They are also available from both ascending and descending orbits. Thus these data are recommended to use in future monitoring for surface changes resulting from geothermal extraction activities.

Since longer wavelengths are much likelier to penetrate vegetation than C-band, conventional differential interferometric synthetic aperture radar was applied to longer wavelength Advanced Land Observing Satellite data, also available from descending and ascending orbits. No signal was observed in the geothermal fields covered by heavy vegetation (Salton Sea and Heber), just as would be the case with shorter wavelength C-band. However, settling was evident in two other geothermal fields in the region – East Mesa in a non-vegetated area of the Imperial Valley, and Cerro Prieto in Mexico, to the south of the three U.S. fields.

Conclusions

This project proved the value of the persistent scatterer interferometry approach as a cost-effective tool to detect surface changes caused by geothermal extraction amidst extensive agricultural fields. The frequency of collection of synthetic aperture radar data largely exceeds that of the annual leveling surveys currently conducted in the geothermal fields of the Imperial Valley. Thus satellite synthetic aperture radar data can be effectively used for future monitoring of surface changes.

Recommendations

The routine future use of persistent scatterer interferometry deformation monitoring is strongly recommended for the geothermal fields of the Imperial Valley in Southern California. It may be possible to use persistent scatterer interferometry as stand-alone techniques or in conjunction with leveling and/or global positioning system measurements for verification purposes. If monitoring is desired in areas that do not have persistent scatterer points at present, corner reflectors could be installed in those areas for the purpose of future deformation monitoring. Furthermore, the use of the current reference leveling benchmark, S-1246, in the Salton Sea geothermal field could be reconsidered, as this study established that it is not really motionless. Although a true motionless reference location is not likely to be found, a location next to one of the regional global positioning system stations (Benchmark Number P507), which is the closest to the field, may be more suitable, because the amount of its movement would be known. Currently, one of CalEnergy's leveling benchmarks, RED-1, is installed in the proximity of P507 and thus could be adopted as a future reference point.

Benefits to California

It has been known for some time now that differential interferometric synthetic aperture radar is a very good and cost-effective technique to monitor large areas for surface deformation. However, its applications were restricted to relatively dry and non-vegetated areas. The results of this study demonstrate that another interferometric synthetic aperture radar approach, persistent scatterer interferometry, can effectively detect deforma-

tion also in agricultural areas. Thus, this study is beneficial to the planning of deformation monitoring in any other geothermal fields in California, and in particular fields amidst vegetation, that might have been so far considered out of reach of interferometric synthetic aperture radar. Since good results were obtained in a challenging agricultural area, such as the Salton Sea geothermal field, it is reasonable to assume that most fields in vegetated areas can greatly benefit from the application of similar persistent scatterer interferometry techniques.

1.0 Introduction

SAR interferometry has been successfully used to identify and measure surface deformation from a variety of natural and man-made causes, such as regional tectonic changes, earthquakes and water withdrawal. This project investigated the possibility to apply SAR interferometry techniques to detect surface deformation, mostly subsidence, associated with the geothermal fields in the Imperial Valley, California.

1.1. Subsidence Due to Geothermal Field Exploitation

Abundant field evidence shows that geothermal reservoir deformation can propagate to the surface and cause vertical and even horizontal displacements (Narasimhan and Goyal 1984). These displacements have important implications both for the local environment and the continued successful exploitation of the fields.

A geothermal project typically involves the extraction of steam and/or hot water to produce electricity, as well as for direct use. Due to environmental concerns (e.g. subsidence, groundwater pollution, etc.), the spent fluids are usually injected back into the geothermal reservoir. However, operational factors dictate that only a fraction of the extracted fluid is used for injection, ranging from a low of 20% for steam reservoirs to a high of 80% for hot water reservoirs. Thus, in most cases the operation of geothermal fields is associated with a net fluid withdrawal, generally resulting in a fluid pressure drop. The re-injection of spent fluid is also accompanied by a temperature drop in at least part of the reservoir. Thus changes in reservoir fluid content, reservoir fluid pressure, and formation temperature are the three main factors causing a redistribution of the stress and strain fields in the geothermal reservoir and the surrounding formations. One of the possible consequences of this redistribution is surface subsidence.

Although subsidence rates of tens of centimeters per year are encountered in some fields (e.g., 45 cm/yr at Wairakei, New Zealand), geothermally induced subsidence typically has annual rates in the centimeter range. For example, subsidence of 47-48 mm/yr was measured using leveling and GPS surveys in The Geysers in Northern California (Mossop and Segall 1997). However, even modest subsidence can have far reaching consequences, especially if the geothermal operations take place near agricultural fields, as in the Imperial Valley.

Deformation accompanying reservoir depletion may also activate movements along preexisting faults, leading to seismicity (e.g., Narasimhan and Goyal 1984). Microseismic activity associated with production and injection has been documented for a number of geothermal fields, such as the Cerro Prieto field (Glowacka and Nava 1996) just south of the region studied in this project. Seismic activity near Salton Sea in 2005 has also been suggested by some to be attributable to geothermal extraction. However, the most detailed study of this swarm by Lohman and McGuire (2007) does not make such a connection.

1.2. Geothermal Fields in the Imperial Valley

Geothermal power generation in the Imperial Valley began in 1979. The currently active geothermal fields in the Imperial Valley are the Salton Sea, Heber, and East Mesa (Figure 1-1), with a total existing capacity of 538 Mega watts (MW). However, the remaining geothermal potential of the area is estimated at 2,025 MW (*PIER Geothermal Database* - GeothermEx 2004). The whole region is characterized by a high heat flow, at > 100 mW/m² (Lachenbruch et al. 1985). The hot underground reservoirs likely originated ~4 to 6 million years ago when the peninsula of Baja California separated from the mainland of Mexico and hot mantle material flowed to the shallower levels where the crust thinned along the system of faults now known as the San Andreas (Elders and Sass 1988).

The *Salton Sea geothermal field (SSGF)*, operated by *CalEnergy, Inc.*, is located on the southern end of the Salton Sea and is the largest in the Imperial Valley. The SSGF is also the hottest in the Imperial Valley and one of the hottest water-dominated systems in the world (260° C to 320° C water at 700-1000 m depth). Temperature measured in wells reach ~350°C by ~2 km depth (Hulen and Pulka 2001). The thermal gradients are very high, rising across the area from near regional (0.09°C/m) to extreme (0.8°C/m). The reservoir fluid is also characterized by very high salinity. Based on heat flow studies in a series of shallow and deep wells, the field has been described as an elongated area about 4 km wide and 12 km long. The SSGF power generating plants have a total capacity of about 350 MW. One of the SSGF production wells is the largest in the Imperial Valley and is capable of producing 990x10³ kg/hr of fluid (Boardman 1998). The remaining potential of the filed is estimated at 1,400 MW.

The *Heber geothermal field (HGF)*, owned and operated by *ORMAT Nevada, Inc.*, is located about 8 km south of El Centro, California, and just south of Heber, California, in the southernmost part of the Imperial Valley. The reservoir ranges in depth from 610 to 1830 m and produces a moderate-temperature (180°C), low-salinity fluid (Boardman 1998). Reservoir modeling studies (*Analysis of Potential Surface Subsidence and Uplift,* 1992) were used to design a system of alternating injection and production wells to control reservoir fluid pressure and thus minimize subsidence. Part of the field subsides while another part appears to rise. The HGF electrical generating plants are with a total capacity of 115 MW, while the estimated remaining potential is 27 MW.

The *East Mesa geothermal field (EMGF)* is also operated by *ORMAT Nevada, Inc.* Unlike the two previous fields, it is on federal land in the eastern part of the Imperial Valley, 24 km east of El Centro. The reservoir is water-dominated, at depths between 1830 m and 2280 m, and with temperatures in the range 145°C to 180°C (Boardman 1998). The EMGF plants have a capacity of 73 MW, with a remaining potential of 75 MW.

1.3. Sources of Surface Deformation in the Imperial Valley

The subject of this report is surface deformation possibly associated with the geothermal fields in the Imperial Valley. The operation of these geothermal fields is indeed associated with such deformation, and there are concerns that with increased production in the near

future, subsidence may become a larger problem than it has been so far. In this connection, the geothermal companies in the Imperial Valley are obligated to carry out annual

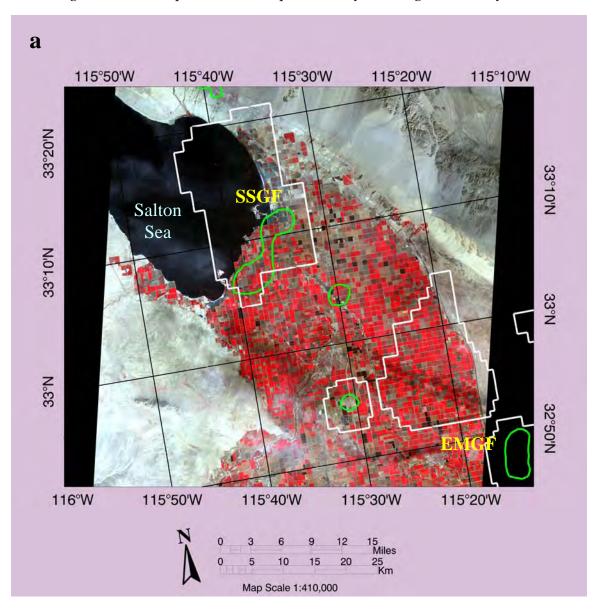


Figure 1-1. Two satellite images showing study area (ASTER VNIR Level 1B). Red indicates vegetation (RGB representation: R is centered at 0.807 mm, G at 0.661 mm, and B at 0.556, i.e. ASTER bands 3, 2, and 1, respectively). The three geothermal fields are marked as follows: SSGF (Salton Sea), EMGF (East Mesa), and HGF (Heber). Green outlines mark production areas. White outlines mark known geothermal resource areas (KGRAs). (a) Northern part of study area. (b) Southern part of study area. Brown line marks national border. Note different agricultural pattern in the US compared with Mexico. Source:

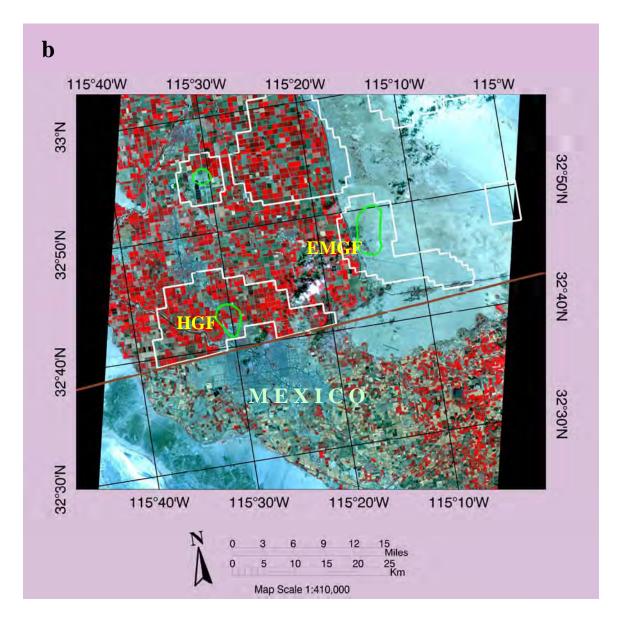


Figure 1-1. Continued (b).

geodetic surveys and to report their results to the *Imperial County/Surveying & Engineering Department* and the *California Department of Conservation/Division of Oil, Gas and Geothermal Resources (DOGGR)*. Leveling data from these surveys and related reports have been made available to this project. To minimize direct effects on agriculture, the production and injection wells are located in drilling islands so that some of the wells are drilled directionally under farm fields (Signorotti and Hunter 1992).

It is important to understand that there exist other sources of subsidence in the vicinities of the geothermal fields. Elsewhere in the world, subsidence from underground water pumping is very widespread. However, groundwater in the Imperial Valley is too saline for irrigation and most other uses, so water from Colorado River is primarily used. Still,

Mellors and Boisvert (2003) used SAR interferometry to show subsidence due to water pumping from wells on a farmland near the Coyote Creek Fault, apparently drawing water from a shallow aquifer with lower salinity. It is not known if more water extraction of this kind is going on in the Imperial Valley.

A more important source of deformation in the Imperial Valley is tectonic activity. This region is characterized by active faulting and rifting, crustal extension and thinning, magmatism, regional subsidence, and sedimentation. Several prominent tectonic features are encountered in the region, each contributing to its complex environment. The Salton Trough is a broad structural depression between the San Andreas and San Jacinto faults, extending northwest from the Gulf of California. This rift zone created a desert basin, bounded by mountains and overlain by sediments up to 6 km thick. The local tectonic setting is transitional from the extensional tectonics of the Gulf of California to the transform tectonics of the San Andreas Fault System (e.g., Sturz et al. 1998).

Furthermore, seismicity is pronounced and occurs on both major faults and cross-faults in the area (Petersen et al. 1991; Magistrale 2002). Several seismically active, mostly right-lateral strike-slip faults, transect the area (Figure 1-2). The southern stretch of the well-known San Andreas Fault Zone, with a slip rate of up to 49±3 mm/yr (Bennett et al. 1996), approaches the region from the northwest. Data from the Southern California GPS network (http://www.scign.org) show an east-west gradient in the plate motion vectors west of the San Andreas and suggest considerable strain in the region. Two large earthquakes in 1940 and 1979, Mw6.9 and Mw6.4 respectively, ruptured the Imperial Fault Zone. Its average slip rate has been estimated at 15 to 20 mm/yr (Peterson and Wesnousky 1994) and at 35±2 mm/yr (Bennett et al. 1996). To the north, the Brawley Fault Zone is known for its complexity, high heat flow, and thin crust. Along with a rapid slip rate, these factors contribute to earthquake swarms and probably aseismic creep. A 1975 swarm of events (Johnson and Hadley 1976) with magnitudes below 5.0 left a surface trace exceeding 10-km length, with a maximum vertical displacement of 20 cm. Another notable fault, the Superstition Hills Fault, was ruptured by a 1987 M_w6.6 event, producing a 50-cm offset within the first day, and up to 1-m total offset in the months to follow. This event also ruptured a nearby fault and triggered slip on the Imperial, San Andreas, and Coyote Creek faults. The Coyote Creek fault is one of the southern strands of the San Jacinto Fault and was last ruptured by a 1968 Mw6.5 event (Borego Mountain earthquake). Further to the south, the Cerro Prieto Fault Zone in Mexico accumulates a total slip of 42±1 mm/yr (Bennett et al. 1996) and last ruptured in 1934.

A recent swarm of more than a thousand earthquakes occurred in August 2005 very close to the Salton Sea geothermal field (Figure 1-3). The maximum magnitude was M5.1. The swarm occurred at the Obsidian Buttes, near the southern San Andreas Fault and has been investigated in detail by Lohman and McGuire (2007). They found that the swarm activity can explain only 20% of the geodetically observed deformation in the region, and suggested that aseismic fault slip was the primary process driving this seismic

activity. The authors used models of earthquake triggering by aseismic creep to explain both the time history of the seismicity and a migration velocity of about 1 km/h exhibited by this and several other earthquake swarms (in 1966, 1975, and 1981) in the Salton Trough.

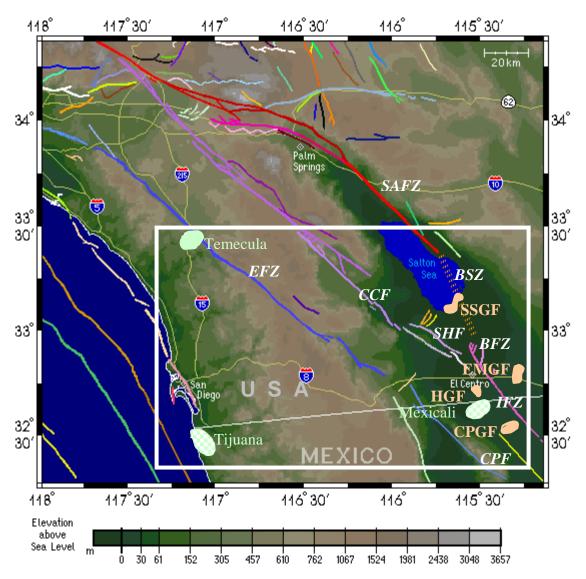


Figure 1-2. Map of the western U.S.-Mexico border region. Adapted from the SCEC map "Faults in California/Southern Region" (http://www.data.scec.org/faults/faultmap.html). Geothermal fields and their names are marked in light orange: SSGF – Salton Sea; HGF – Heber; EMGF – East Mesa; and CPGF – Cerro Prieto. Areas of subsidence from underground water withdrawal and their names are marked in light green - filled pattern for known areas (Temecula), checkered pattern for suspected areas (Tijuana and Mexicali). Fault names are marked in white: SAFZ – San Andreas Fault Zone; IFZ – Imperial Fault Zone; CPF – Cerro Prieto Fault; EFZ – Elsinore Fault Zone; CCF – Coyote Creek Fault; SHF – Superstition Hills Fault; BFZ – Brawley Fault Zone; and BSZ – Brawley Seismic Zone.



Figure 1-3. The epicenter location of the 2005 M5.1 earthquake shown on an ASTER optical image. Red areas show vegetation. Yellow and blue outlines show the known geothermal resource and the production areas of the Salton Sea geothermal field (SSGF), respectively. Black line marks the Brawley seismic zone (BSZ). Source: ?

The latest earthquake swarm in the area started in late March 2009 near Bombay Beach on the east side of Salton Sea, with the largest magnitude of M4.8. More than 460 events have been recorded. The swarm continues at time of writing. A 4-D representation can be seen at http://www.youtube.com/watch?v=cAJn8lmPEuw&feature=channel_page. It is noteworthy that the southernmost portion of the San Andreas fault, which is in the area of the Salton Sea is assumed to be ripe for a large earthquake (Fialko 2006).

Other sources for surface deformation in the Imperial Valley are irrigation of the extensive agricultural fields in the area and soil compaction. This area is one of the leading agricultural areas in California. The climate of Southern California contributes to year-round agricultural activities in the region. Water for irrigation comes from Colorado River, supplying water for about 500,000 acres of farm land. The level of the Salton Sea is sustained by an inflow of municipal and industrial drainage, as well as the agricultural irrigation drainage.

1.4. SAR Interferometry – Definitions and Techniques

The strong points of any radar include day-and-night and all-weather capabilities, none of which are possible for optical systems. Unlike the point geodetic measurements using traditional, ground-based methods, radar observations from a flying platform can provide semi-continuous spatial coverage, and the possibility of frequent monitoring (e.g., every 35 days for the European satellites).

A brief review is provided here of synthetic aperture radar (*SAR*), platforms with SAR instruments on board, and interferometric SAR (InSAR) and related techniques, starting with simplified explanation of terminology and proceeding to more details. "Aperture" relates to the size of the radar antenna on a platform. The platform is generally a satellite or an airplane. The aperture would have to be physically rather large in order to achieve acceptable measurement resolution. Instead, radar data are processed in such a way that advantage is taken of the motion of the platform that carries the radar instrument. Hence, a large aperture is "synthesized." For example, the physical size of the antenna on the European satellites is ~10 m, but the synthesized antenna is equivalent to a 4-km aperture. If SAR data are collected at two different times, the two images can be compared to create an interferogram (hence, *InSAR*), in which topography and surface displacement (if any) show up as phase differences in the form of fringe patterns. Comparing two interferograms makes it further possible to exclude topography and estimate only surface deformation, which is the subject of differential InSAR (Diff InSAR or DIn-SAR). Thus, InSAR is generally used to measure topography and DInSAR is used to measure surface displacements (e.g., from earthquakes, volcanoes, land subsidence), although the term "InSAR" is often used generically in both cases. The InSAR and DIn-SAR techniques have been discussed in many publications (e.g., Bürgmann et al. 2000; Rosen et al. 2000; Massonnet and Feigl 1998; Jakowatz et al. 1996; Zebker et al. 1994). The effect of topography can be removed from the interferograms either by using a digital elevation model (DEM) or interferometric pairs with a known absence of surface change. Thus surface deformation associated with subsidence, for example, can be measured from radar images taken at two different times, together with either a third image (e.g., Zebker et al. 1994) or a digital elevation model (DEM) to account for topography. These are known as three- and two-pass differential interferometry, respectively.

Several letters are commonly used in remote sensing to indicate different wavelengths. In connection to SAR, the most popular wave bands are P (wavelength \sim 1 m), L (\sim 1/4 m), C (\sim 5-6 cm), X (\sim 3 cm), and Ku (\sim 2 cm). The longer the wavelength, the likelier it is to penetrate vegetation, but the vertical resolution of the displacement measurements generally decreases with wavelength.

Table 1-1 shows details of past, current, and planned satellite missions with SAR instruments on board. ERS-1/2 and ENVISAT are European, RADARSAT-1/2 are Canadian, and JERS-1 and ALOS are Japanese satellites. Side-looking spaceborne synthetic aperture radar maps a continuous swath as the satellite moves along its orbit track. Both the amplitude and phase of the radar echoes are measured, as they come from independent patches on the ground, a few to tens of meters in size. The size of these pixels and their combination (so-called "multilooking") determines the spatial resolution of the radar, as shown in the last column of Table 1-1. Initially, due to more precise knowledge of the ERS orbits (Scharroo et al. 1998), most InSAR studies were using SAR data from ERS-1 and ERS-2, succeeded by ENVISAT. ERS-2 ceased to be useful for differential interferometry after January 2001. RADARSAT-1 data were not good for DInSAR earlier but

became suitable after the fall of 2000. ERS, ENVISAT and RADARSAT all use the C-band (5.6-cm wavelength, ~5 GHz radar frequency). This wavelength does not penetrate vegetation efficiently because it is comparable with the predominant size of tree leaves. The old Japanese JERS-1 and the new ALOS use wavelengths (23.6 cm, radar frequency ~1.3 GHz) that penetrate vegetation better than the C-band. Thus the C-band is more prone to temporal decorrelation (i.e., incoherent changes over time) than the L-band and, at least for conventional DInSAR, works best for relatively arid regions, uncomplicated topography, and urban areas.

Table 1-1. Parameters of satellites with SAR capabilities

Satellite	Time of Operation/ Launch	Freq. Band	Polari- zation	Cycle, days	Alti- tude, km	Look Angle, deg	Swath Width, km	Resolu- tion, m
ERS-1	1991-2000	С	VV	35 (3)	~785	23	100	~25
ERS-2	1995-present	С	VV	35	~785	23	100	~25
ENVISAT	2002-present	С	HH/VV	35	~800	14-45	56-405	25-1000
RADARSAT-1	1995-present	С	HH	24	~800	10-59	50-500	~8-100
RADARSAT-2	2007-present	С	multi	24 (3)	~800	10-59	10-527	~3-100
JERS-1	1992-1998	L	HH	44	~580	35	75	~18
ALOS	2006-present	L	multi	46 (2)	~690	10-50	70-360	10-100

Source:?

The airborne SAR instruments date back to the 50's, starting from the military and moving onto the commercial area. Commercialization of traditionally military airborne SAR applications has been slow, due to lack of understanding of its possible benefits, and costs associated with building the SAR instruments (e.g., Erwin 2001). Jakowatz et al (1996) give details on airborne SAR.

In DInSAR, the spatial resolution is the same as that in the topographic measurements, but the vertical resolution is by orders of magnitude better. The spaceborne version is known to be capable of identifying sub-centimeter surface displacements with a mmprecision. Airborne DInSAR used to be considered unsuitable for detection of surface deformation, because due to atmospheric winds airplane trajectories could not be determined as accurately as satellite orbits. However, nowadays airborne DInSAR is quite applicable to detection of surface displacement, even though it has remained largely untapped in this respect. Airborne DInSAR would not improve on the already very high precision of detection of vertical displacements from satellites but can provide much better spatial resolution. The key technology developments in the last decade that make this possible are as follows: (1) greatly improved navigation systems that enable the airborne platform to fly the same course multiple times; (2) adaptive algorithms that make it possible to estimate any registration and stretching corrections necessary to achieve the high correlation required for coherent exploitation of image pairs; and (3) readily available high-quality SAR imagery and the ability to control the collection of the appropriate image pairs.

There exist a number of airborne SAR systems. An example of recent advances is the Lynx system resulting (Burroughs 1999) from collaboration between *Sandia National Lab*

and *General Atomics*. It is a very advanced, fine-resolution, and lightweight SAR system, designed to be mounted on both manned and unmanned (e.g., Predator) aerial vehicles. The operating frequency is 16.7 GHz (Ku-band, 2 ~ wavelength), providing ~3 cm resolution imagery at distances of up to 25 km, and ~10 cm resolution up to 55 km away, with the Lynx flown at an altitude of ~7,600 m. This fine resolution makes it possible to detect very small surface changes, such as footprints in a soft terrain (Burroughs 1999). In fact, most of the interest of the military for airborne SAR has been wrapped around its capability to identify target movement with high accuracy. Such systems, however, are likely with limited applications for surface changes that take place over much longer periods of time because loss of coherence occurs much faster for shorter wavelengths.

The only airborne system that holds great promise for detecting surface deformation of slower rates is UAVSAR (Unmanned, or Uninhabited, Aerial Vehicle SAR) using L-band. It is a result of a NASA-funded project at the *Jet Propulsion Laboratory* (Principal Investigator Dr. Scott Hensley). The first data have been already collected, including over parts of Salton Sea; however, they have not been made public. These rapid advances may eventually lead to decreased costs of collection of airborne SAR data suitable for DInSAR, and perhaps it will be possible to order data collections over sites of interest in the future.

The interference pattern in the SAR interferograms reflecting surface displacement consists of fringes, with each fringe representing a range change (displacement in the lineof-sight, or LOS, direction) of half a wavelength. This translates into 10 mm, 28 mm, and 125 mm for Ku-, C- and L-band, respectively. An important requirement for DInSAR to work is for the perpendicular components of baselines (distances between the satellite orbits or airplane trajectories of the two passes) to be rather small. What is "small" depends on the wavelength and the altitude of the platform. For example, while perpendicular baselines generally smaller than ~200 m (better yet < 100 m) are preferable for ERS or ENVISAT SAR (C-band) interferometry, 600 to 1000 m is a good baseline for JERS-1 or ALOS (L-band). Furthermore, a surface displacement must have a significant component along the line-of-sight (LOS) direction to be resolvable by DInSAR, since the look angles are generally steep. When the look angle (i.e., the angle measured from a vertical line from the SAR platform to the ground) is small, LOS captures vertical movements better than horizontal movements. This means that subsidence, in particular, can be rather accurately detected. This is valid for ERS-1/2, which had a fixed small look angle (~23°), and for any of the other satellites when the look angle is adjusted to be optimal for subsidence. (see ranges of look angles in Table 1-1.)

Surface displacement occurring between two passes translates into a phase difference that can be measured by DInSAR. The simplified equation expressing this relationship is $d\phi/\Delta\varrho=4\pi/\lambda$, where $d\varphi$ is the phase change, $\Delta\varrho$ is the displacement measured along the line connecting the ground and the satellite (i.e., line of sight, LOS), and λ is the microwave length used by the SAR instrument. This relationship shows, somewhat counter

intuitively, that the amount of surface change captured by InSAR does not depend on the altitude of the platform. This and other details of the technique, omitted here, lead to the unprecedented power of DInSAR to detect rather small surface deformations. DIn-SAR is much more sensitive to such changes than to the topography. For example, for the ERS or ENVISAT satellites, 1-m of topography results in a phase signature of ~4.3°, while a 1-m surface displacement results in a 3000 times larger effect on the phase. Thus while InSAR can be used to determine topography to an accuracy of meters (from satellites) or tens of centimeters (from airplanes), displacements can be theoretically determined at the sub-centimeter level with millimeter precision.

In view of the above, the spatial and vertical resolution of spaceborne InSAR used for determining DEM's has been 25-30 m and ~15 m, respectively. Airborne InSAR has provided a superior altitude precision (~0.5 m), at spatial resolutions as small as 1 m all the way down to 10 cm. However, the linear size of the area covered by an airborne SAR scene is of the order of 100s of meters or smaller, while the coverage of spaceborne SAR is much larger, generally 75 km to 100 km. (See Table 1-1).

Although DInSAR is capable of capturing sub-centimeter surface deformation with mm-precision in ideal conditions (e.g., dry and low-vegetated areas for C-band), the measurements can be adversely affected by various errors (e.g., atmospheric propagation effects, satellite orbit errors, temporal decorrelation). Thus comparison with ground measurements where available, such as leveling and GPS, plays an important role in validating the InSAR observations.

An innovative development of the InSAR technique has been based on so-called "persistent" or "permanent" scatterers (PS). There have been several techniques developed by different groups (e.g., Hooper et al. 2004; Hooper and Zebker 2007; Ferretti et al. 2000, 2001, 2007). As a generic name for these techniques, **PSI** will be used throughout the text; i.e., PS interferometry. PS InSAR has been also widely used in the literature, but this term is not used in this report in order to not confuse it with a specific technique, PSIn- SAR^{TM} , developed at the Politecnico di Milano University, Italy. (See more details in Section 3.2 in Chapter 3.) In conventional DInSAR displacements are measured through the radar phase change that is made with a pixel-resolution of ~80 m² and with a full cycle of phase change at ½ of the radar wavelength (i.e., 2.8 cm for the C-band radar with a 5.6 cm wavelength) in the radar line-of-sight (LOS). In contrast, the PSI techniques use individual radar reflectors that are generally smaller than the resolution pixel cell and that remain coherent over long time intervals. These are suitable to extract displacement time series as if numerous small benchmarks have been used. The PSI methods have several advantages over DInSAR, such as good phase coherence from most radar scenes regardless of the perpendicular baselines, possibilities for long-baseline interferometry with up to 1.6 km separation, and removal of atmospheric phase from the displacement phase signal. The PSI techniques can work in areas where conventional DInSAR fails. For example, C-band DInsAR is only good in relatively non-vegetated, dry areas, while PSI

can successfully extract deformation time series for numerous coherent targets (PS points) amid the vegetation. Moreover, when at least 45 scenes are used, a precision of <0.1 mm/yr of the deformation rates has been documented (Ferretti et al. 2007). There are a number of PSI applications reported in the literature by now (e.g., Bell et al. 2008; Bürgmann et al. 2006; Funning et al. 2007; Furuya et al. 2007). These techniques were also used in this project (Eneva and Shanker 2007; Eneva et al. 2009), and the results are included in Sections 3.2 and 3.3 of Chapters 3.

Another relatively new interferometric technique makes use of Small Baseline Subsets (*SBAS*) and was described in detail by Lauknes (2004). This technique relies on a combination of differential interferograms created by using SAR image pairs with small orbital separations (baselines), which reduces spatial decorrelation. A multi-temporal data set is used that is divided into several small baseline subsets, separated by large baselines. A singular value decomposition technique is further applied to "link" the separate small baseline subsets, thus increasing the temporal sampling rate. Atmospheric and orbital artifacts are filtered out based on the availability of both spatial and temporal information. Several applications of the SBAS technique have been reported (e.g., Berardino et al. 2002; Pepe et al. 2005). This method was also used in this project, and results are reported in Section 3.3 of Chapter 3.

1.5. Previous Applications of InSAR to the Detection of Surface Subsidence in Geothermal Fields

There are several published applications of differential radar interferometry to geothermal fields. Carnec and Fabriol (1999) and Hanssen (2001) used ERS SAR images prior to August 1997 collected over the Cerro Prieto geothermal field just south of the Imperial Valley fields. Carnec and Fabriol modeled the subsidence using a combination of Mogi sources (i.e., assuming elastic deformation in a half-space from simple point sources), as was previously done for The Geysers (Mossop and Segall 1997). One of the interferometric pairs in Carnec and Fabriol's work covered approximately five months during which a M3.4 event with a normal fault mechanism occurred in the field at ~2 km depth. Since a maximum of 6.6-cm of subsidence was measured (i.e., ~16 cm/yr), which is higher than the 12 cm/yr measured with other methods (Glowacka et al. 1999), the earthquake may have contributed to the subsidence. This is plausible, given that a 1966 M3.4 event at depth ~1.1 km in the Imperial Valley produced a 9.3-km long surface rupture (Brune and Alen 1967). Shorter time intervals will be needed for radar interferometry to distinguish whether vertical displacements are due to small earthquakes.

Massonnet et al. (1997) used two ERS SAR scenes from 1992 and 1994 to show 75 mm of subsidence in the East Mesa geothermal field. Compared with the other Imperial Valley geothermal fields, East Mesa is in arid environment and is relatively distant from population and agricultural areas. Coso, in Eastern California, provides another prominent example of a geothermal field where subsidence was observed with InSAR (Fialko and Simons 2000; Wicks et al. 2001). Up to ~35 mm/yr subsidence was detected in interfero-

grams covering the period between 1992 and 1997. Wicks et al. modeled the deformation with both Mogi sources and a planar elastic dislocation (Okada 1985), while Fialko and Simons used multiple prolate spheroidal sources. Another InSAR result from a geothermal field is from the Euganean geothermal field in Italy (Strozzi et al. 1999), where ERS SAR scenes between 1992 and 1996 were used to detect a subsidence rate as low as 4 mm/yr.

All radar interferometry applications listed above used ERS C-band SAR data. Two applications of L-band SAR data from JERS-1 are also relevant to the proposed work. One detected annual subsidence of up to 10 cm/yr in Jakarta, Indonesia, due to water extraction (Hirose et al. 2001), and the other identified uplift of up to 19 cm after steam injection and subsidence of 17 cm following production, both between two consecutive passes of the satellite (44 days for JERS-1), in the vegetated area of the Cold Lake oil field, Albert, Canada (Stancliffe and van der Kooij 2001). This indicates that both archived JERS-1 SAR data and the PALSAR instrument on ALOS could be useful over vegetated and agricultural areas, but no such studies specifically over geothermal fields have been reported in the literature.

Numerous examples of applications of InSAR to surface subsidence due to nongeothermal causes have accumulated over the last decade. Regardless of the cause, these are all examples indicating that InSAR is a viable tool for detection of surface deformation in general, of which subsidence over geothermal fields is just one particular example.

2.0 Project Methods

While the East Mesa geothermal field is located in relatively dry and non-vegetated area, agricultural lands are ubiquitous in the Imperial Valley and cover up the other two geothermal fields (Salton Sea and Heber). Farmland is expected to cause decorrelation problems for C-band that could make it impossible to detect surface deformation with conventional DInSAR. For the latter to detect deformation in such areas, the temporal separation between the images would have to be too short, such as two consecutive images (i.e., 35 days apart for ENVISAT or ERS). Indeed, Lohman and McGuire (2007) found such a 35-day pair enclosing the occurrence times of the largest of the events in 2005 earthquake swarm near Salton Sea. The coherence was good enough to capture a LOS displacement of ~14 cm that the authors attributed to the displacements caused by the swarm (mainly the largest M5.1 event) and a likely accompanying aseismic slip.

However, the deformation rates due to geothermal activity are much smaller and could not be detected over such short time periods, so a longer temporal separation between SAR images, e.g. 9 to 12 months, would be needed. C-band easily decorrelates with such long temporal baselines over agricultural areas. Therefore, it became clear that instead of conventional DInSAR, PSI and SBAS techniques have to be applied to analyze ENVISAT and RADARSAT C-band data over Salton Sea and Heber. The PSI techniques used with the ENVISAT data over Salton Sea were developed at Stanford University (e.g., Hooper et al. 2007; Shanker and Zebker 2007). The same group was also involved with the SBAS application to the same data. Another PSI technique was used with the RADARSAT data, PSInSAR™ (Ferretti et al. 2001, 2007). Particular attention was paid to the comparison of these results to ground-based measurements from both leveling data surveys and the regional GPS network. The available ground-based measurements are described in Section 3.1 of Chapter 3, PSInSAR™ results from the RADARSAT data and comparison with the ground-based measurements are described in Section 3.2 of Chapter 3, and PSI and SBAS results from the ENVISAT data are discussed in Section 3.3 of Chapter 3. Appendices A and B give more details on the observations from Section 3.2 of Chapter 3, and appendices C and D show additional results from Section 3.3 of Chapter 3.

Since the various applications to the data over Salton Sea took many trials and errors, a decision was made to not tackle other areas (such as Heber) until good results are obtained over the first study area. Therefore, Sections 3.2 and 3.3 of Chapter 3 of this report are limited to the description of PSI and SBAS results from the Salton Sea geothermal field.

L-band data from ALOS were also analyzed. Because of the longer wavelength, vegetation is better penetrated and better coherence was hoped for compared with C-band. That is, traditional DInSAR could work in this case, unlike for C-band from ENVISAT and RADARSAT. However, longer wavelengths are more limited in capturing small deformation, so it was not clear in advance whether L-band DInSAR would provide useful results. DInSAR is much less time consuming than PSI, so in this case interferograms

were calculated and examined over all three geothermal fields in the Imperial Valley, as well as the Cerro Prieto geothermal field in Mexico, south of the main study area. The ALOS results are reported in Section 3.4 of Chapter 3.

Furthermore, it was expected that UAVSAR L-band data collected over Salton Sea would become available during this project. Although repeat SAR scenes were indeed collected over that area, they have not been made available to the public yet. Thus in Section 3.5 of Chapter 3 the discussion was limited to the description of the potential of UAVSAR for future measurements of surface deformation.

3.0 Project Results

3.1. Ground-Based Measurements in the Imperial Valley

As part of this project, proprietary leveling measurements were supplied by the geothermal companies operating the Imperial Valley geothermal fields, *CalEnergy* and *Ormat*. The purpose was to compare these measurements with the results obtained from InSAR. This report focuses on a comparison of satellite InSAR results from the Salton Sea geothermal field with ground-based leveling data from 2003-2009 supplied by *CalEnergy*. In addition, some regional GPS measurements were also evaluated in an effort to address the fact that observations of surface deformation by any means are affected by both geothermal activity and regional tectonics in the greater vicinity of the fields. Figure 3-1 shows relevant information for the area of Salton Sea that is discussed below.

3.1.1. Leveling Measurements in the Geothermal Fields

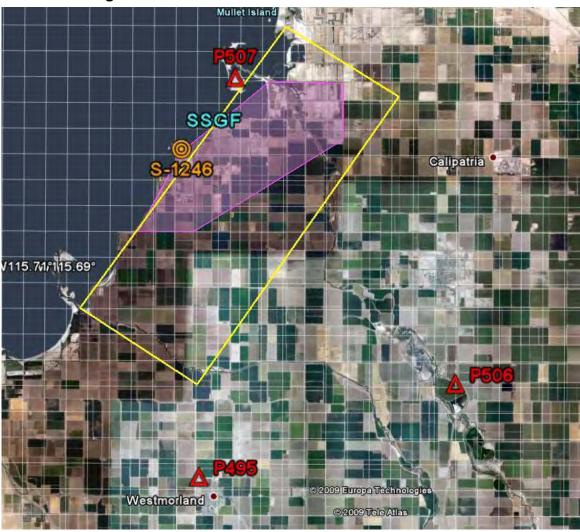


Figure 3-1. Map of the greater area around the Salton Sea geothermal field (SSGF). Study area is shown with yellow rectangle. Pink polygon marks the area with leveling benchmarks. The location of the reference benchmark, S-1246, is shown with orange circle. GPS stations are marked with red triangles. (background from GoogleEarth). Source:?

The geothermal companies in the Imperial Valley are obligated to carry out annual geodetic surveys and to report their results to the *Imperial County/Surveying & Engineering Department* and the *California Department of Conservation/Division of Oil, Gas and Geothermal Resources (DOGGR)*. Both *CalEnergy* and *Ormat* have supplied leveling reports and contour maps. In addition, *CalEnergy* has supplied proprietary digital leveling data for the period 1998 - 2009 and supporting digital documents.

CalEnergy had leveling surveys done at Salton Sea in June 2003, June 2004, June 2005, May 2006, October 2007, and March 2009. Over the years, the number of leveling benchmarks at Salton Sea has changed somewhat, with a network of 79 existing monitoring stations being surveyed over the last several years. The area covered by this network is shown in Fig. 3-1 (pink polygon). In all surveys, one of the benchmarks, S-1246 (at Obsidian Butte), was used as a reference and was thus considered motionless. Not all of the 79 stations have measurements in all years. For example, during the 2007 survey, seven monuments had been destroyed, or were not found, or were damaged. During the 2009 survey five of the previously missing monuments were reset. All this explains further figures comparing InSAR results and leveling data, where leveling observations for some of the stations do not exist in some years.

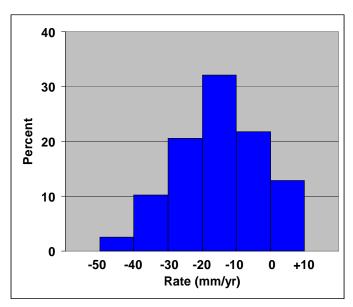


Figure 3-1-2. Histogram of the vertical deformation rates derived from the benchmark leveling data, referenced to S-1246.
Source: ?

The distribution of annual rates of vertical deformation at Salton Sea is shown in Figure 3-1-2. This figure shows that most rates indicate subsidence, and that they rarely exceed -40 mm/yr. However, about 13% of the benchmarks appear to move upwards, but all this is relative to S-1246. The maximum upward rate is +5.4 mm/yr. Note that even if all benchmarks subside, but some benchmarks move downward more slowly than S-1246, there would be the appearance of uplift at their locations (Possible movement of the reference benchmark is discussed further below). Figure 3-3 shows in a

map sketch the spatial distribution of these rates. It is evident that all relative uplift is observed in the northwestern part of the area covered by the benchmark network. Again, this may be just slower subsidence than that at the location of the reference benchmark, S-1246.

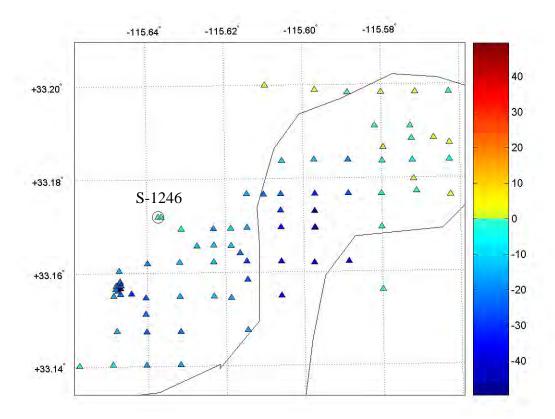


Figure 3-3. Spatial distribution of deformation rates from the leveling data relative to S-1246. Color scale shows rates in mm/yr. Outline traces the Salton Sea geothermal field (from a shapefile included in a geothermal database that may be too old, hence so many benchmarks are outside the outlined area). Source: ?

Ormat has also supplied leveling data, for the Heber geothermal field. These include hard copies of reports and contour maps from their annual leveling surveys. The Heber network consists of 137 benchmarks. All measurements were referenced to benchmark A-33 located on the All American Canal headwall structure at California Hwy 98. These data are also very valuable but were not used in this report.

3.1.2. GPS Measurements and their Comparison With the Leveling Data

The available GPS measurements in the Imperial Valley, especially at locations surrounding the Salton Sea geothermal field, were carefully examined. Data from the Scripps Orbit Permanent Array Center – SOPAC – at the University of California San Diego (http://sopac.ucsd.edu) were used for this purpose. The GPS measurements are made by the PBO (Plate Boundary Observatory) network, operating for about 3.5 years, and the CRTN (California Real Time Network) stations, operating for about 10 years.

Site <u>coordinates</u>, <u>velocities</u> and <u>time series</u> are created by a SOPAC refined model (Nikolaidis 2002) that takes into account offsets (co-seismic or otherwise), linear velocity, exponentially decaying term for post-seismic relaxation, and annual and semi-annual fluctuations. Input data provided to the model are the daily processed site positions calculated at SOPAC using the software packages specifically designed for the purpose.

Figure 3-4 shows the locations of the GPS stations in the region. Horizontal and vertical regional velocities are shown in Figure 3-5. The horizontal velocities are relative to the Pacific Plate and are rather significant compared with the vertical rates. Table 3-1-1 lists the velocities for the nine stations closest to the Salton Sea geothermal field.

Table 3-1-1. GPS deformation rates (in mm/yr) around the Salton Sea geothermal field (H-horizontal component relative to the Pacific Plate, V-vertical component).

Vel.	P502	P503	P506	P507	P508	P495	P499	CRRS	GLRS
Н	41.67	19.94	42.24	42.40	42.47	28.39	39.11	25.39	42.61
V	-1.23	-2.53	-8.67	-13.37	+0.29	-3.12	-2.20	-0.31	-0.31



Figure 3-1-4. Map with the locations of the GPS locations (http://sopac.ucd.edu). Source:?



Figure 3-5. Map showing the vectors of horizontal velocities in the study area (green arrows). Triangles mark the GPS stations. Numbers next to stations show horizontal velocities relative to the Pacific Plate and vertical velocities, both in mm/yr. Black lines mark known faults. Yellow rectangle shows the study area of the Salton Sea geothermal field. Yellow circle marks the location of the reference benchmark S-1246. Adapted from http://sopac.ucsd.edu.

As seen from Figs. 3-1, 3-4 and 3-5, P507 is the closest PBO GPS station to the reference benchmark used in the Salton Sea leveling surveys, S-1246, at a distance of 3.8 km. Another one of the 79 leveling benchmarks, RED-1, used by *CalEnergy*, is nearby P507. The next closest stations are P506 and P495, at 16.2 km SW and 17.4 km SE from P507, respectively. Incidentally, the maximum subsidence from all PBO GPS in the area is noticed at these three stations, highlighted in yellow hues in Table 3-1-1. Measurements at GPS stations further away, although mostly indicating subsidence, are much smaller.

This shows that subsidence in the field due to fluid extraction is occurring superimposed on the largest regional subsidence in that area attributable to tectonic movements.

It is thus reasonable to use the regional movements registered at the three closest stations to make inferences about the likely regional movements (i.e., unrelated to the geothermal activity) in the area covered by the 79 benchmarks. However, this assertion is not solid enough for P507, as this GPS station is very close to the field.

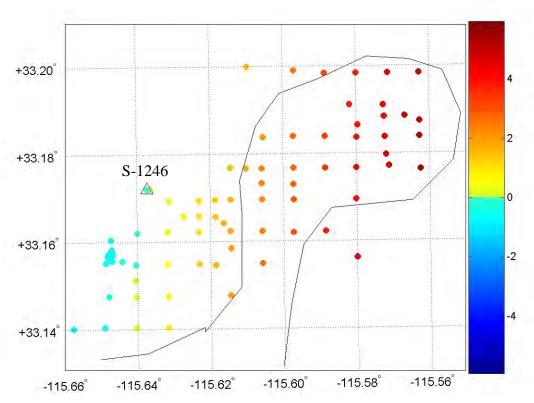


Figure 3-1-6. Model of possible horizontal tectonic movements at the benchmark locations in the W-E direction, relative to S-1246. Color scale shows these rates in mm/yr. Positive values mean movement eastward, negative values mean movement westward.

Figure 3-6 shows a model of the W-E component of the regional horizontal movements at the benchmarks, relative to S-1246. This model is calculated using simple linear interpolation from the GPS observations at P507, P506, and P495. Table 3-1-2 shows the de

Table 3-1-2. Decomposition of the horizontal velocities at three PBO GPS stations.

Station	H _{W-E}	H _{S-N}
P507	+20.52	-37.10
P506	+29.98	-29.76
P495	+21.63	-18.39

composition of the horizontal velocities from the velocity map (Fig.3-5) into W-E (used for the modeling in Fig. 3-6) and S-N components for the three GPS stations (not shown). The two components are positive when movement is indicated to the east and north, respectively.

Source:?

This modeling gives an idea about the horizontal movements (relative to S-1246) attributable to tectonic movements. The emphasis on the W-E component is due to the ac-

quisition geometry of the satellite data. The geometry for the ENVISAT data (from both descending and ascending orbits) and the RADARSAT data from the ascending orbit are such that mostly vertical movements are captured and to some extent horizontal movements in the W-E direction. The geometry of the RADARSAT data from the descending orbit is different, almost equally sensitive to vertical movements and the W-E component of the horizontal movements. Neither the ENVISAT nor the RADARSAT geometry is sensitive to the S-N component of the horizontal movements. Therefore, Fig. 3-6 emphasizes the possible W-E horizontal component attributable to tectonic movements at the benchmark locations, all measured relative to the reference benchmark S-1246. As seen in the figure, these components indicate mostly eastward movement (positive values), with increasing rates to the east (up to 5 mm/yr), but also some westward movements in the western part of the plot (~ –1to –2 mm/yr). These combine to indicate that the tectonic environment in the area of the benchmark network is extensional. Any deformation due to the geothermal activity is superimposed on that extensional regime.

Making a similar estimate as that in Fig. 3-6 but for the vertical tectonic movements is more challenging. The reference benchmark S-1246 has been considered motionless for the purpose of leveling measurements, and therefore the InSAR results presented further are also referenced to that point, for the sake of comparison between the two types of measurements. However, a simple comparison with the GPS data indicates that S-1246 likely subsides. The vertical velocity (deformation rate) at P507 measured over the last 3.5 years is ~ -13.4 mm/yr (Fig. 3-5). In contrast, the leveling at the RED-1 benchmark used by CalEnergy, located next to P507, indicates a relatively steady uplift at +5.4 mm/yr, measured over the last 6 years. Since this is referenced to S-1246, such a discrepancy indicates that S-1246 might be subsiding at a rate of -18.8 mm/yr. This might have been revealed if, say, it were part of the PBO GPS network. Recall from Fig. 3-1-3 that the leveling data at other benchmarks in the northern-eastern corner of the area also show uplift or almost no change with time. As already suggested, this may be simply due to the fact that they subside at a slower rate compared with the reference point S-1246. It is not known if rates of -13.4 mm/yr at P507 and -18.8 mm/yr at S-1246 can be attributed only to tectonic causes or more likely are mixed with the geothermally induced subsidence. Indeed, both locations are very close to the geothermal field, especially S-1246, and the indicated absolute subsidence rates at their locations appear the largest in the whole region. For these reasons, no attempt was made to model the vertical tectonic movements at the benchmark locations in a way similar to what was done for the W-E horizontal regional velocity components in Figure 3-6. The SOPAC website (http://sopac.ucsd.edu) also contains position time series for all GPS stations. Figure 3-7 shows an example of such a time series of the horizontal (S-N and W-E) and vertical components at P507. The slopes of these time series (Fig. 3-7a) represent the horizontal and vertical velocity components. Note that horizontal velocities estimated from the slopes of the position time series are different from those shown on the map in Fig. 3-5 and in Table 3-1-1 because they are not referenced to the Pacific Plate. However, there is no difference between the vertical velocities. The detrended time series (i.e with trends

removed) display annual and semi-annual changes (Fig. 3-6b). It would be of interest to see if the InSAR results can resolve such periodic fluctuations as well. Details of the model parameters are also shown in the figure. The appearance of these time series is common for most GPS stations. The time series for some stations indicate jumps from earthquakes; one example is the time series for P506 (not shown here) that shows a jump at the time of the M5.1 earthquake in September 2005.

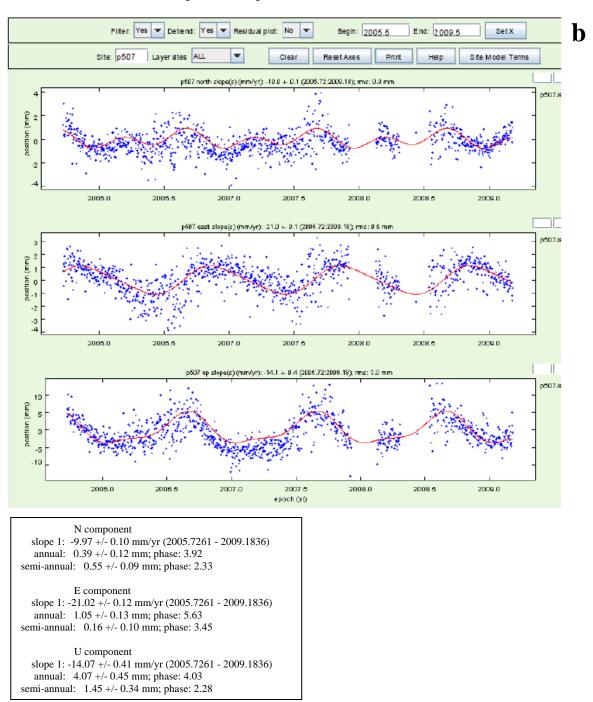


Figure 3-7. (b) Filtered and detrended time series of surface deformation from (a). The three velocity components are shown from top to bottom as in (a). Modeling parameters are shown in box above. Slopes are rates in mm/yr. Note that these numbers are calculated daily and they change, although not significantly (hence the slight difference with the vertical velocity at P507 in Fig. 3-1-3 above). Horizontal components are not referenced to the Pacific Plate, so horizontal velocities are not comparable to the numbers shown in Fig. 3-1-3. From http://sopac.ucsd.edu. Source:

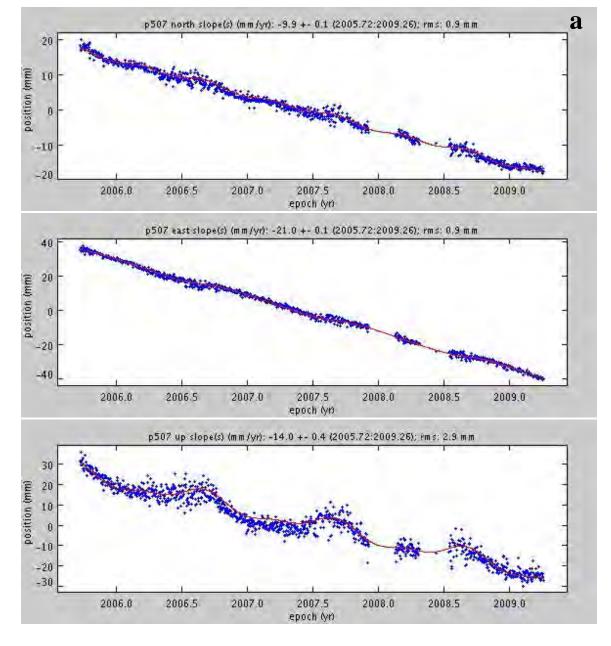


Figure 3-7. (a) Filtered position time series for station P507. From top to bottom: W-E horizontal component, S-N horizontal component, and vertical component. Positive movements are in direction to the east, north, and upwards, respectively. Fitting curves in red are used for detrending the series in (b). Slopes indicate horizontal and vertical velocity components. From http://sopac.ucsd.edu.

3.2. Results from C-band RADARSAT Data

The analysis of SAR data from the Canadian RADARSAT-1 satellite was performed by TRE Canada. Like the ASAR data from ENVISAT, these data are C-band, and thus a regular DInSAR is not expected to work in this heavily vegetated region, so the TRE's proprietary PSInSARTM algorithm was applied for the purpose. This algorithm is one of several existing PSI (persistent scatterer interferometry) techniques. Figure 3-8 shows the area that was studied, encompassing the whole Salton Sea geothermal field.



Figure 3-8. The Salton Sea area of interest (yellow outline) as seen from Google Earth. Also shown is the reference point (green marker), S-1246, used as reference for the leveling. Source: ?

3.2.1. Method

The identification of permanent scatterers (PS) in a series of RADARSAT images comprised the following sequence of steps. First, all radar data archives were screened to determine the most suitable source of raw data for the particular area of interest and to select all the high quality images within the chosen dataset. As the signal echo from a single point target contains many returning radar pulses it appears defocused in a synthetic aperture radar (SAR) raw image. The first processing step was therefore to focus all the received energy from a target in one pixel. The images were then precisely aligned to each other, or co-registered, and analyzed for their suitability for interferometry. The main parameters analyzed in this stage were the normal (perpendicular) baseline and the temporal distribution of the images. Then a number of statistical analyses followed on the phase and amplitude characteristics of the backscattered radar signal

that return to the satellite. If a concentrated number of signals reflect off a particular feature within a pixel and backscatter to the satellite, the feature is referred to as a scatterer. When the same scatterer appears in all, or most, of a data set of SAR images of a particular location, then the scatterer is deemed to be permanent. At this stage it was possible to identify a subset of pixels, referred to as permanent scatterer candidates (PSC), that were used to estimate the impact on signal phase of ionospheric, tropospheric and atmospheric effects, as well as possible orbit errors. Once the signal phase is corrected for these effects, any remaining change in the signal phase is expected to directly reflect surface change.

3.2.2. SAR Data Selection

Imageair, Inc. submitted a research data proposal to the Alaska SAR facility, which was fortunately approved. That made it possible to download RADARSAT data at no cost to this project. This was a significant advantage, because RADARSAT data are otherwise rather expensive. Two suitable RADARSAT datasets were identified, one acquired from an ascending orbit and the other from a descending orbit (Figure 3-9). The ascending dataset consists of 26 scenes acquired in S1 beam mode, on track 52. The descending dataset consists of 30 scenes acquired in S6 beam mode, on track 116. However, due to some technical problems at ASF, some of the existing scenes could not be downloaded within the limits of this project, although they may become accessible in the future. So the actual numbers of scenes used in the analysis were 18 ascending and 21 descending images, covering the periods of 05/20/2006 - 04/22/2008 and 05/24/2006 - 04/19/2008, respectively. Tables 3-8 and 3-9 show lists of the data used. These reduced numbers of scenes were still promising, because in general, in order to measure displacement to millimeter accuracy, a minimum stack of 15 images is required, which is satisfied in this case. Fortunately, none of these available images had to be discarded during the initial stages of processing: That is, all 39 scenes were found to be suitable for the PS analysis.

Table 3-8. RADARSAT-1, track 52, ascending orbit scenes used in the analysis. Bn = normal baseline; Bt = temporal baseline. The image highlighted in red was used as the "master" image in the processing.

#	Date	Sensor/mode	Bn (km)	Bt (days)
1	20/05/2006	RSAT-S1	0.761	-360
2	13/06/2006	RSAT-S1	0.096	-336
3	07/07/2006	RSAT-S1	0.975	-312
4	31/07/2006	RSAT-S1	0.027	-288
5	24/08/2006	RSAT-S1	0.441	-264
6	17/09/2006	RSAT-S1	0.012	-240
7	11/10/2006	RSAT-S1	0.132	-216
8	28/11/2006	RSAT-S1	0.100	-168
9	15/01/2007	RSAT-S1	0.072	-120
10	04/03/2007	RSAT-S1	0.386	-72
11	28/03/2007	RSAT-S1	0.060	-48
12(M)	15/05/2007	RSAT-S1	0.000	0

31

13	08/06/2007	RSAT-S1	0.079	24
14	02/07/2007	RSAT-S1	0.077	48
15	17/12/2007	RSAT-S1	0.327	216
16	10/01/2008	RSAT-S1	0.004	240
17	03/02/2008	RSAT-S1	0.260	264
18	22/03/2008	RSAT-S1	0.107	312

Table 3-2-2. RADARSAT-1, track 116, descending orbit scenes used in the analysis. Bn = normal baseline; Bt = temporal baseline. The image highlighted in red was used as the "master" image in the processing.

#	Date	Sensor/mode	Bn (km)	Bt (days)
1	24/5/2006	RSAT-S6	0.16	-336
2	17/6/2006	RSAT-S6	0.14	-312
3	11/7/2006	RSAT-S6	0.24	-288
4	4/8/2006	RSAT-S6	0.05	-264
5	21/9/2006	RSAT-S6	0.14	-216
6	15/10/2006	RSAT-S6	0.03	-192
7	8/11/2006	RSAT-S6	0.20	-168
8	2/12/2006	RSAT-S6	0.02	-144
9	26/12/2006	RSAT-S6	0.02	-120
10	12/2/2007	RSAT-S6	0.04	-72
11	8/3/2007	RSAT-S6	0.31	-48
12	1/4/2007	RSAT-S6	0.08	-24
13(M)	25/4/2007	RSAT-S6	0.00	0
14	19/5/2007	RSAT-S6	0.04	24
15	12/6/2007	RSAT-S6	0.14	48
16	6/7/2007	RSAT-S6	0.02	72
17	30/7/2007	RSAT-S6	0.07	96
18	21/12/2007	RSAT-S6	0.25	240
19	7/2/2008	RSAT-S6	0.00	288
20	2/3/2008	RSAT-S6	0.17	312
21	26/3/2008	RSAT-S6	0.04	336



Figure 3-9. RADARSAT-1 satellite coverage of the study area by the ascending orbit (track 52) and descending orbit (track 116) imagery. Yellow rectangle marks study area. White arrows show direction of footprints of satellite movement. Source:?

3.2.3. Master Image Selection

PSInSAR™ requires that one image (or scene) in each dataset has to become both a geometric and temporal reference to which all the other images are then related. This image is referred to as the "master" image, and the remaining scenes are "slave" images. The master image was chosen according to the following criteria: (1) it minimizes the spread of normal baseline values for the slave images; (2) it minimizes the temporal baseline values between the master and each slave image; and (3) it minimizes the effects of signal noise arising from changes in vegetation cover and/or small changes in the look angle of the satellite from one scene to another. The master images used in this analysis are highlighted in red in Table 3-2-1 and 3-2-2. These tables also show the normal (vertical) and temporal baseline values (Bn and Bt) associated with each "slave" image. These two parameters are fundamental to any interferometry study. In any SAR dataset, there are factors that can impede the application of interferometry. These include extensive and dense vegetation, water coverage, irregular temporal distribution of images, and too long intervals between successive images. For the Salton Sea area, the presence of agricultural fields, the relatively limited number of man-made structures, and the relatively low number of images tend to reduce the density of PS.

3.2.4. Phase and Amplitude Analysis

Each pixel of a SAR image contains information on the amplitude of signals that are backscattered toward the satellite, as well as on the signal phase. The amplitude is a measure of the amount of the radar pulse energy reflected, while the phase is related to the length of the path of the electromagnetic wave, from the platform to the ground and back again. Analyses of both amplitude and phase of the SAR image provide an indication of the stability of each pixel, over time, whereby it is possible to identify those pixels that are most likely to behave as permanent scatterers. Statistical methods are used extensively in this process. Among the different statistical parameters that can be computed, two are of particular interest: the Phase Stability Index (PSI), obtained from the phases of the images within the dataset, and the Multi Image Reflectivity (MIR) map, derived from the amplitude values of the available acquisitions.

After the statistical analyses of the SAR images have been completed, a set of differential interferograms is generated. This entails subtracting the phase of each "slave" image from the phase of the "master" image. In doing so, the difference in signal path length between the two images is calculated. This difference is related to possible surface change. The differential interferograms represent the starting point for applying the PSInSARTM approach.

The Phase Stability Index (PSI) indicates the variability of the signal phase for every pixel computed for every image in the archive. It ranges from 0 to 1 and can be represented in a digital image. A pixel having a high PSI value is most likely to be a PS.

The amplitude of a pixel within a SAR image is the aggregate of the backscattered energy toward the satellite from within the pixel's equivalent land area. This equivalent land area is referred to as the radar spatial resolution, and in the case of the RADAR-SAT-1 Standard Beam mode, it is about 20 m x 5 meters. It is necessary to look into the amplitude values of all the images in the dataset in order to understand exactly what was seen by the satellite at the time of each acquisition.

If a target has experienced significant change in its surface characteristics it will exhibit variation in its reflectivity (electromagnetic response) between two acquisitions. In such circumstances, the possibility of detecting surface change by means of SAR interferometry is seriously compromised. The reason is that the signal phase difference between the two images in such a case contains not only the contribution due to displacement, but also that due to the change in the reflectivity of the target. This prevents, in the worst case, the obtaining of any useful information on surface deformation.

Normally, speckle impacts negatively on the quality and usefulness of SAR images. However, the more images taken of the same area at different times or from slightly different 'look' angles are available, the easier it is to reduce the speckle effect. The purpose

of removing speckle is to increase the quality and level of details of the amplitude image enabling it to be used as a background layer for observing the presence of PS results.

The Multi Image Reflectivity (MIR) map is the means by which speckle reduction is accomplished. Averaging a number of images tends to negate the random amplitude variability, leaving the uniform amplitude level unchanged. The MIR maps derived from the ascending and descending orbit images are shown in Figures 3-10 and 3-11, respectively.

It should be emphasized that the information in the MIR map is the reflectivity of each pixel, i.e. the ability to backscatter the incident wave toward the satellite. Flat surfaces (roads, highway, rivers, lakes) act like a mirror, meaning that if their orientation is not



Figure 3-10. Ascending orbit multi-image reflectivity (MIR) map of the Salton Sea area. Source:?



Figure 3-11. Descending orbit multi-image reflectivity (MIR) map of the Salton Sea area. Source: ?

exactly perpendicular to the incident wave, negligible energy is reflected back to the sensor, so they appear dark in the images. On the other hand, because of their irregular physical shape, metal structures or buildings reflect a significant portion of the incident signal back to the radar, resulting in very bright pixels in the MIR map.

After the signal phase and reflectivity analyses are completed, differential interferograms can be generated. They are obtained by subtracting the phase values of each "slave" image from those of the "master" image. In any SAR image, there are embedded

topographic distortions that arise during image acquisition. These are removed using a reference Digital Elevation Model (DEM), leaving ground movement and the signal phase distortions arising from atmospheric effects as the only embedded variables.

3.2.5. Estimation of the Atmospheric Effects

When a radar signal enters and exits a moisture-bearing layer in the atmosphere, its wavelength can be affected, introducing potential errors into the signal path length. The removal of atmospheric impacts is fundamental for increasing the precision of ground movement measurement.

A subset of pixels, usually corresponding to buildings, lampposts, antennas, small structures and exposed rocks, is chosen from among those that have high PSI values. These are referred to as PS Candidates (PSC). PSC density is, of course, higher in towns and cities compared with forests and vegetated areas. However, it is often possible to obtain good PSC density even in those areas.

For each image, the atmospheric impacts are estimated at each PSC location. The process is statistically based and benefits in accuracy by greater numbers of available images. By comparing the atmospheric contribution on neighbouring pixels that would be experiencing the same atmospheric conditions, the atmospheric contribution can be reconstructed over the whole image.

The processed dataset allows identification of a PSC cluster dense enough to identify and extract the atmospheric contribution over the entire area of interest.

3.2.6. Post-Processing

The processed data further undergo a thorough quality control following a certified pro-



Figure 3-12. Detail of the study area as seen from an orthophoto, highlighting the high resolution of the imagery. Source: ?

cedure. The PS are aligned on an optical image layer. Ancillary data available for the PS post-processing include high resolution (50 cm) orthophotos (e.g., Figure 3-12) of the study area, a digital elevation model (DEM) with 10-m elevation postings, and a vector file describing the local road network. These data were downloaded from the USGS EROS data center. It is to be noted that the orthophotos were acquired in December 2002, while the RADARSAT images used in the analysis were acquired in the period 2006-08. So, any changes (e.g. construction) that have occurred in the period between 2002 and 2006 would show in the radar data, but not in the orthophotos used as a background layer.

3.2.7. PS Results

Benchmark S-1246 was used as a reference point for the levelling data provided by CalEnergy. Thus, for the sake of comparison with the levelling data, a similar reference is used for the PS results as well. Since the S-1246 location cannot be used in the PS analysis, two reference points were chosen from the descending and ascending orbit PS points that were as close as possible to S-1246 (Figure 3-13). Note that all three points are within 55 m of each other. Based on its proximity to the geothermal reservoir and the results of the PS analysis, there are indications that S-1246 is actually moving both downwards and eastwards (at least in the period covered by the RADARSAT data, 2006-2008). This was already independently suggested in Section 3.1 of this chapter.

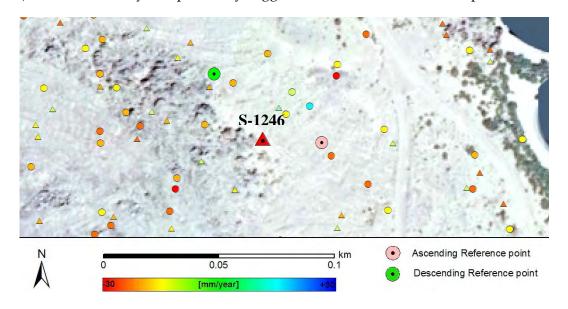


Figure 3-13. Locations of the ascending (pink circle) and descending (green circle) orbit reference points and the reference benchmark S-1246 (red triangle).

Like in Fig. 3-13, in subsequent figures the S-1246 benchmark is shown as a red triangle, the ascending orbit data reference point is shown with a green circle, and the descending orbit data reference point is marked with a pink circle.

The estimated velocity fields from the ascending and descending orbit images are shown in Figures 3-14 and 3-15, respectively. The colored markers superimposed on the ortho-

photo correspond to the locations of PS points identified in the study area and where precise differential measurements could be carried out by PS InSARTM. All displacement measurements were computed with respect to the supposed reference points assumed to be motionless.

Furthermore, Figures 3-16 and 3-17 show the PS elevation values referenced to mean sea level. The elevation of a PS point helps to identify whether it is on the top of a building or at ground level and can help to clarify topographic anomalies where ground movement is significant. Typically, the vertical resolution of elevation is around 1.5 m.

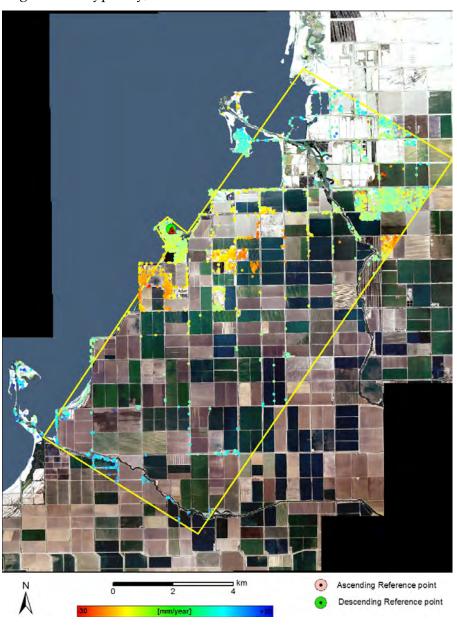
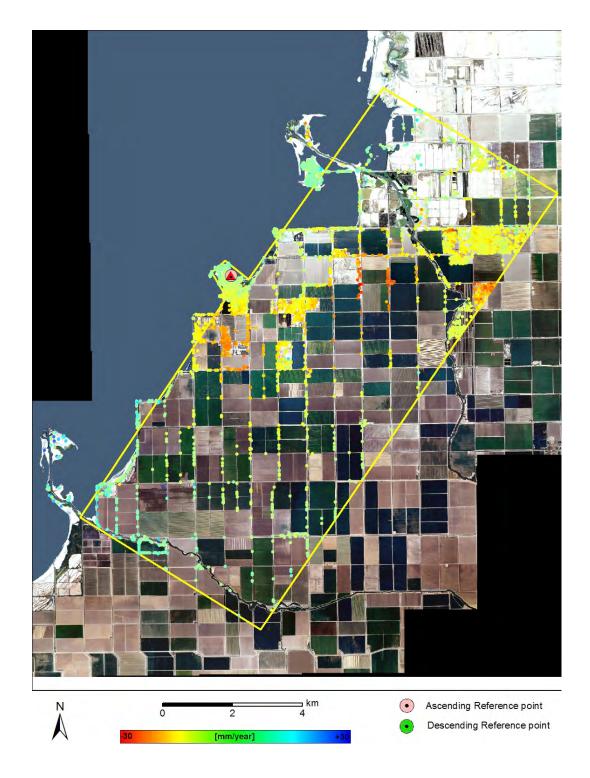


Figure 3-14. Ascending orbit PS velocity map. The red triangle shows the location of the S-1246 reference benchmark. Source: ?



 $\label{eq:Figure 3-15.} \textbf{ Pescending orbit PS velocity map. The red triangle shows the location of the S-1246 reference benchmark. Source: ?}$

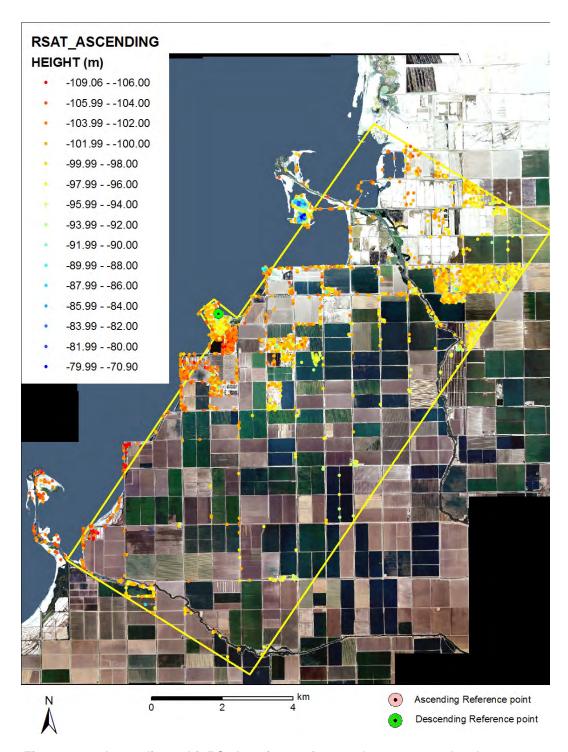


Figure 3-16. Ascending orbit PS elevations referenced to mean sea level.

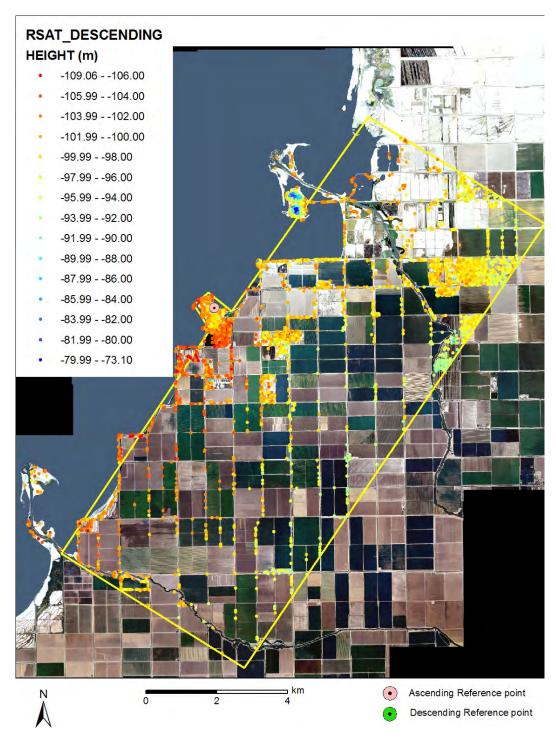


Figure 3-17. Descending orbit PS elevations referenced to mean sea level. Source: ?

3.2.8. Summary of the Characteristics of the Study

Tables 3-2-3 and 3-2-4 provide summaries of the characteristics of the analysis of the ascending and descending orbit data. Common to both data sets are georeferencing in which the PS points were aligned on 50-cm orthophotos, UTM Zone 11N /WGS-84 projection system and datum, assumption for motionlessness of the reference points used (both very close to S-1246), study area of size ~95 km², and false alarm rate of 10-5, i.e., only 1 in 100,000 PS points might be actually noise. Thus the risk that a point identified as a PS is noise is rather low in this study. The false alarm rate is the statistically derived index for the probability of this phenomenon.

The distinction between PS density in the areas where buildings or other man-made artefacts are present compared to the agricultural areas is noticeable and to be expected. PS density within the study area lies in a range of values that is typical of this setting (last rows of Tables 3-2-3 and 3-2-4). The PS points are mainly clustered in areas where little or no vegetation is present, along roads and at the geothermal plants in the study area.

Table 3-2-3. Summary of output from the ascending orbit data

Satellite / beam	RSAT / S1	
Acquisition geometry	ASCENDING	
Critical baseline [m]	1621.6	
Analysis time interval	05/20/2006 - 03/22/2008	
Number of scenes processed	18	
Reference point location	3,671,208.29 N; 627,045.14 E	
Number of PS identified	3087 points	
Number of time series estimated	3087	
Average PS density (PS/km²)	32.5 PS points / km ²	

Source:?

Table 3-2-4. Summary of output from the descending orbit data

Satellite / beam	RSAT / S6	
Acquisition geometry	DESCENDING	
Critical baseline [m]	3041.2	
Analysis time interval	05/24/2006 – 03/26/2008	
Number of scenes processed	21	
Reference point location	3,671,178.62 N; 627,091.82 E	
Number of PS identified	4441 points	
Number of time series estimated	4441	
Average PS density (PS/km²)	46.75 PS points / km ²	

3.2.9. Precision Assessment

The quality and accuracy of results obtained with the PS InSAR technique represent two of the most important goals of this type of study. Extensive analysis of various results of commercial and research projects performed by TRE and the Politecnico di Milano University have made it possible to calculate the accuracy of PS measurements.

Three parameters characterize the PS results: precision of the estimated velocities; precision of the estimated elevations; and precision of the geocoding.

Table 3-2-5 summarizes the typical precision values applicable to PS located within 2 km from a reference point when at least 45 SAR acquisitions have been processed. The standard deviations in the estimation of PS velocities and elevations are a function of distance from the reference point. In the present PS analysis, the resulting velocity standard deviation values are shown in Figure 3-18 for the ascending orbit dataset and in Figure 3-19 for the descending orbit data.

The relative positioning error is given by the resolution of the SAR system in use and equals \pm 7 m in *range* direction (east-west) and \pm 2 m in *azimuth* direction (north-south). In order to illustrate the quality of the geocoding achieved in the PS processing, an example is presented in Figure 3-20. The background layer is a high resolution (50 cm) orthophoto image downloaded from the USGS *The National Map* Seamless Server.

In Figure 3-20, the PS radar targets were identified along a section of a geothermal installation. The pixel resolution of the orthophoto image is greater than the resolution of the SAR system. This difference in resolution manifests itself by showing the PS slightly off the N-S aligned structure at the centre of the image. Figure 3-21 shows how the PS elevation coloration helps to clarify whether a PS point is on the top of a structure or at ground level. The blue PS points are likely located higher, while red points are reflections from the base of the structure.

Table 3-2-5. Measurement accuracies for PS located within 2 km from the reference point, based on the processing of at least 45 SAR images

Velocity	< 1 mm/yr
Elevation	± 1.5 m
Positioning error along W-E direction	± 7 m
Positioning error along S-N direction	± 2 m
Displacement error (single displacement)	< 5 mm

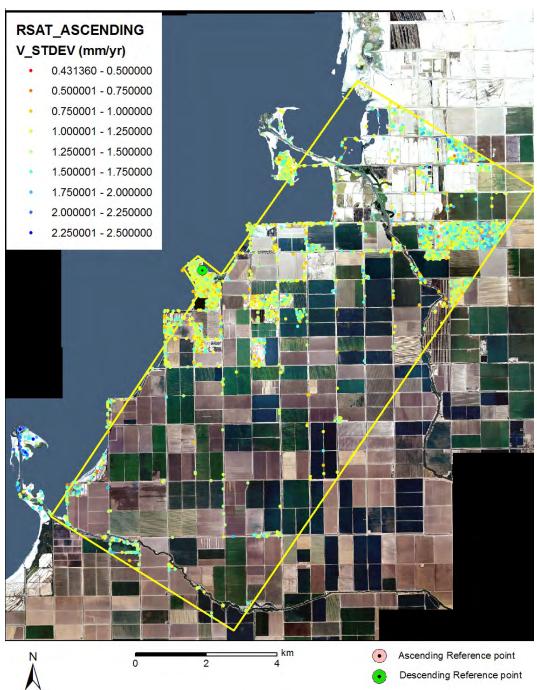


Figure 3-18. Ascending orbit PS velocity standard deviation. Values are in mm/yr. Source:?

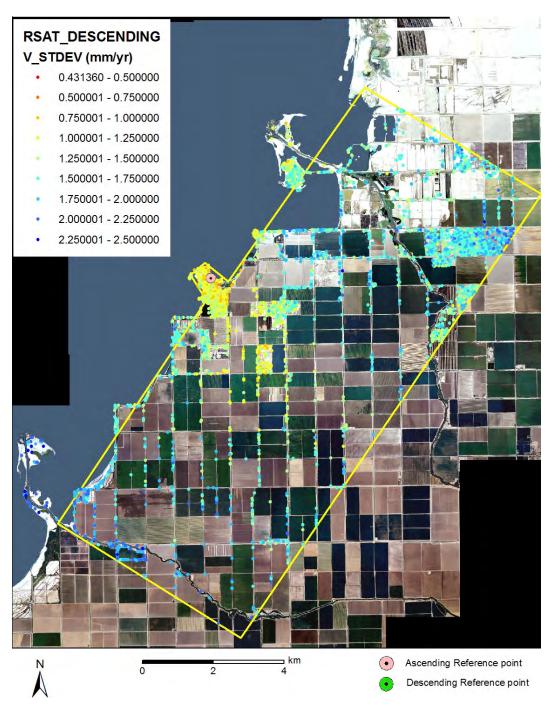


Figure 3-19. Descending orbit PS velocity standard deviation. Values are in mm/yr. Source:?



Figure 3-20. Results of the PS alignment on a 50-cm orthophoto image. Source:?



Figure 3-21. Use of PS height information to determine if a PS is on the ground or at the top of a building. Red PS are located at the base of the structure, blue PS are higher up.

3.2.10. Sensitivity Versors

It is important to point out that all PSInSAR™ displacement measurements are carried out along the satellite Line Of Sight (LOS). The properties of the unit vectors as projected

onto the LOS (versors) are related to the viewing angles for both the ascending and descending orbit acquisitions as shown in Tables 3-2-6 and 3-2-7 below.

Table 3-2-6. Components of the ascending orbit RADARSAT-1 LOS versor for this study

Direction	Component of the versor
North	-0.09255
East	-0.41725
Vertical	0.90407

Source:?

Table 3-2-7. Components of the descending orbit RADARSAT-1 LOS versor for this study

Direction	Component of the versor
North	-0.11082
East	0.71154
Vertical	0.69385

Source:?

Figure 3-22 illustrates the satellite viewing geometry. The corresponding angles are shown in Table 3-2-8. Using the angles depicted in the figure, the north, east, and vertical components in Table 3-2-6 are given by $-\sin\delta^*\!\sin\theta$, $-\sin\delta^*\!\cos\theta$, and $\cos\delta$, respectively. The components in Table 3-2-7 are determined in the same way, but the sign is reversed for the east component, $+\sin\delta^*\!\cos\theta$. This information, coupled with the ascending orbit geometry information, is used to determine the vertical and east-west (E–W) movement in the PS field.

Table 3-2-8. Satellite viewing angles for both orbit geometries

Orbit geometry	Symbol	Angle
Descending	δ	46.06
Descending	θ	8.85
Ascending	δ	25.3
Ascending	θ	12.51

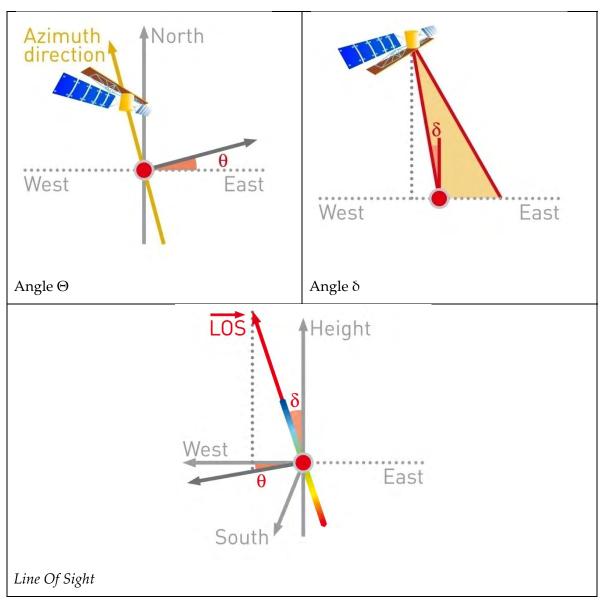


Figure 3-22. Diagram illustrating the satellite acquisition geometry. See Table 3-2-8 for the actual values of the angles.

3.2.11. Observations

The agricultural nature of the Salton Sea area led to a relatively low density of PS, compared to analyses performed in other settings. However, the density values, of 32 PS/km² for the ascending orbit data and 46 PS/km² for the descending orbit data, are normal for this type of environment. PS are mostly concentrated along roads, at the geothermal power plants, and in the arid portions of the landscape along the Salton Sea shore.

The difference in acquisition dates between the background orthophotos used to align the PS and the RADARSAT-1 imagery could possibly be the explanation for some clusters of PS that appear to be located in cropland (Figure 3-23). It is possible that additional infrastructure was constructed between the times when the orthophotos were taken and prior to the times of the RADARSAT data acquisitions, or that the fields were tilled and left uncultivated in the period covered by the radar imagery. This would explain the high number of PS (the roughness of tilled land) and their relatively high coherence. Fallow fields, for example, appear to be the best explanation in the northeastern corner of the study area where another large cluster of PS appears (Figure 3-24). The PS points here are all precisely contained within the boundaries of agricultural fields.

The two geothermal plants in the western-central portion of the study area are located in an area that appears to be subsiding. PS velocities are negative, indicating downward movement, and reach close to 30 mm/yr in the ascending orbit dataset. This can be seen from the time series shown in Figure 3-25. LOS velocities are lower in the descending data, but this is attributable to the more horizontal angle of the S6 beam mode viewing geometry.

For the interpretation of the data, it is fundamental to bear in mind the satellite viewing angles. The ascending orbit data was acquired in S1 beam mode corresponding to a viewing (look) angle of approximately 25° off the vertical. The descending orbit data was acquired in S6 beam mode, corresponding to viewing angle of over 46°. Consequently, the ascending data is more sensitive to vertical movements, while the descending data is equally sensitive to vertical and east-west horizontal movements.

An important observation concerns the distribution of the PS velocity standard deviation (Figure 3-26). In a typical PS analysis, the lowest standard deviations (STD) are located near the reference point and then increase with distance. While this is the case in this analysis as well, some anomalies can be observed. In the ascending orbit data, the STD values around the reference point (Fig. 3-26) are quite low, but the variability is higher than normal. This variability decreases somewhat in the descending orbit data (Figure 3-27) but is still higher than average. A potential explanation for this behaviour may be that the area incorporating the reference points is not static, as is the assumption in the PS analysis, but is actually subsiding or even moving laterally. This could create differential movements that would have an impact on the analysis results. It would be good to change the reference point to one that is known to be stable and reprocess the data; however, for the sake of further comparisons with the existing levelling data, in this analysis the reference points were kept very close to the S-1246 benchmark assumed motionless in the levelling surveys.

As a consequence of the aforementioned observation, and if differential movement is actually occurring in the area of the reference point, this would negatively impact the movement decomposition into the east – west and vertical components. If a lateral com-

ponent of motion is present in a reference point that is assumed to be motionless, a false lateral component will be introduced into the motion of all the PS.

 Reference point [mm/year] 0.2

Figure 3-23. The PS points on the east side of the image seem to be located in an agricultural field. This may be explained with differences between the orthophoto acquired in 2002 and the state of this area in 2006-2008 when the RADARSAT data used in the PS analysis were acquired.

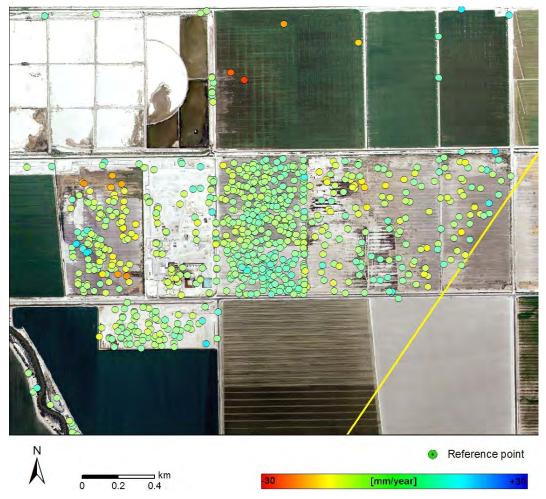


Figure 3-24. Relatively high density of PS likely due to fallow fields.

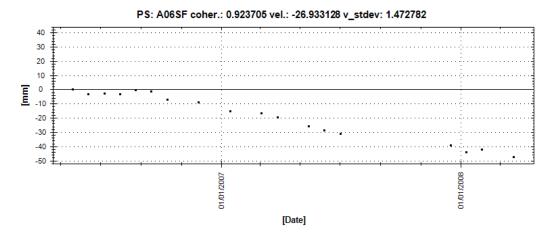


Figure 3-25. Time series of a PS near the centre of the study area that is moving downwards.

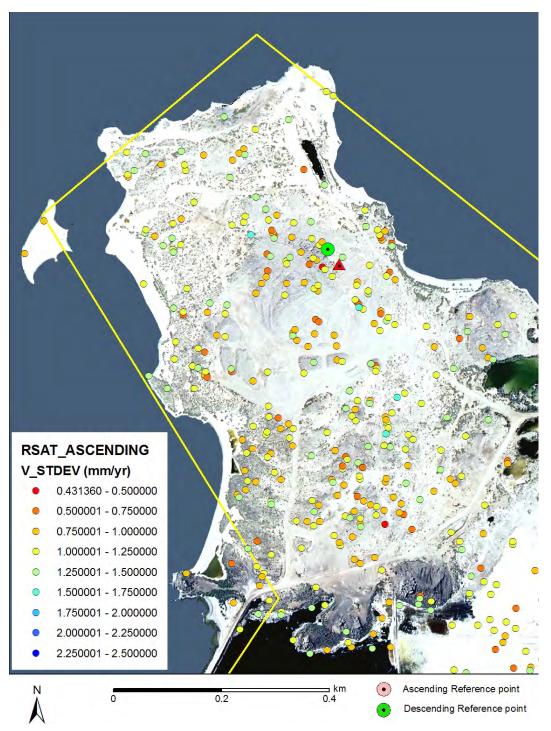


Figure 3-26. Standard deviation of PS velocity (ascending data) near the reference point (green circle), close to the S-1246 benchmark (red triangle).

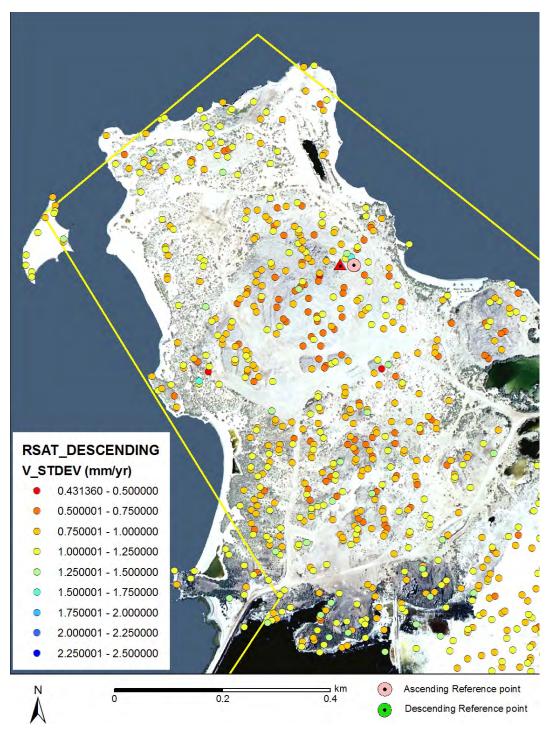


Figure 3-27. Standard deviation of PS velocity (descending data) near the reference point (pink circle), close to the S-1246 benchmark (red triangle).

3.2.12. West-East and Vertical Movement Decomposition

The processing of both ascending and descending datasets allows the LOS movement measured by each satellite to be decomposed into west-east and vertical components. Geometrical considerations were used for this purpose, involving the following steps:

- 1) Both the ascending and descending datasets are resampled to a regular grid with a 100 m cell size. All PS that are within a cell are used to calculate a mean LOS velocity for that same cell. At least one PS must be within the cell. A common reference point is used;
- 2) The two grids are superimposed, and the velocities from homologous cells are used for the decomposition. Only cells that contain values in both grids (ascending and descending) can be used. It is for this reason that the density of measurements in this case is lower than the PS density determined from either ascending or descending orbits alone.
- 3) The two LOS velocities are represented as vectors. These are added together by means of vector addition.
- 4) The resulting vector is then decomposed into W-E horizontal movement and vertical movement using simple geometric relationships involving the unit vectors of the viewing angles shown in Tables 3-2-6 and 3-2-7.
- 5) The results are shown as a regular raster grid in which the cells have a 100 m x 100 m resolution. Note that these are not PS points.

The results of the movement decomposition are shown in the following figures. Figure 3-28 shows W-E horizontal movements. Blue colors indicate eastward movement, while red colors indicate movement toward the west. The strongest eastward motion is located in the central portion of the study area, just north of one of the geothermal plants. Along the southern and northern boundaries of the study area, the pixel hues show that these areas seem to be moving westward. This is likely an artefact caused by the fact that the reference point is not actually motionless. It is possible, in fact, that the reference point is moving eastward (a logical hypothesis as it would be moving toward the depression induced by the geothermal activities). This was independently suggested in Section 3.1.

Vertical movement is shown in Figure 3-2-22. In the central portion of the study area surface deformation is mainly negative, indicating subsidence. This is particularly evident near the geothermal plants, where the PS density is higher. Both the northern and southern portions of the study area contain blue pixels, which indicate uplift. Again, this may be an artefact of the assumption that the reference point is motionless, while it may be actually subsiding, as already discussed in Section 3.1.

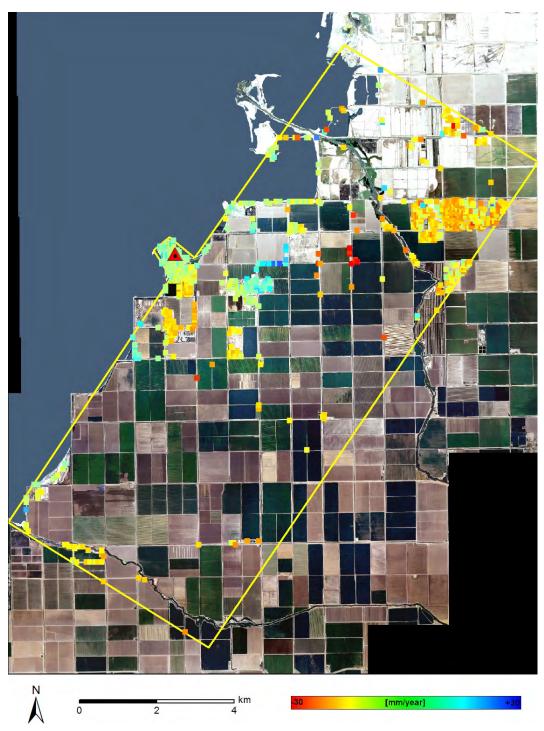


Figure 3-28. W-E component of the deformation. Positive (blue) values indicate eastward movement, while negative (red) values indicate westward movement.

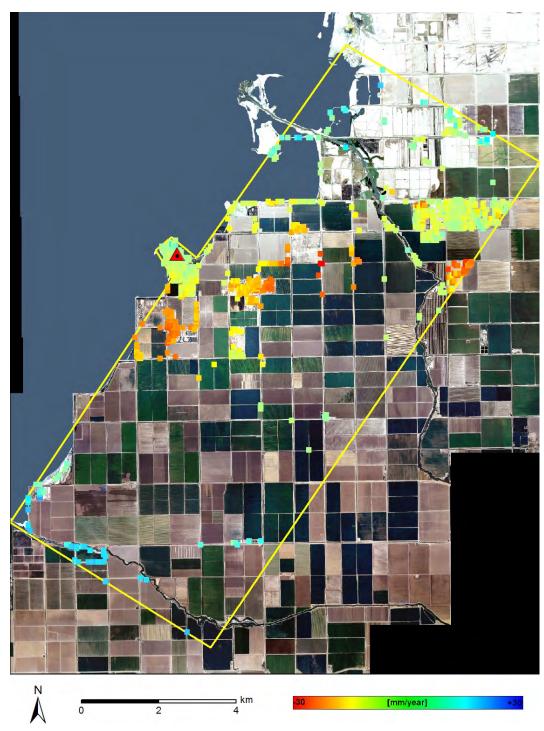


Figure 3-2-22. Vertical component of the deformation. Negative values (red) indicate downward movement, while positive values (blue) indicate uplift.

3.2.13. Comparison With Leveling Data

A comparison was further performed with the leveling data collected at the 79 benchmarks in June 2003, June 2004, June 2005, May 2006, October 2007, and March 2009. For this purpose, the InSAR measurements at PS points within 100 m and within 200 m from the benchmarks were examined. As a reminder, the RADARSAT data are from the period April 2006-April 2008. Appendix A shows all plots for the benchmarks satisfying these conditions, using the measurements at the PS points identified from the scenes with ascending orbits. Appendix B shows all plots for the PS from the descending orbits. The reader is advised to examine the plots in the appendices for more details. Here only one representative example is shown in Figures 3-29 and 3-30 for the ascending and descending data, respectively, using the same leveling benchmark (UG-80). For the sake of brevity, the two types of PS points will be called "ascending" and "descending" PS points.

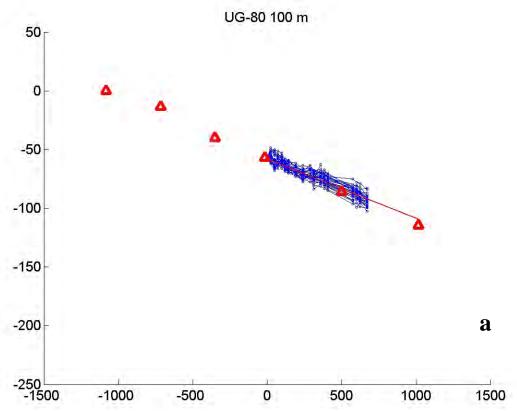


Figure 3-29. Comparison of the leveling data at benchmarkUG-80 and the surface deformation registered at ascending PS points within (a) 100 m and (b) 200 m from the benchmark. The horizontal axis shows days, where the 0 is at the time of the May 2006 leveling survey. The vertical axis shows surface change in mm, with the 0 attributed to the first survey in June 2003. Blue lines and dots show data from the RADARSAT ascending PS points in the LOS direction. Red triangles show the leveling data (i.e, ground-based measurements of vertical deformation only). Red line shows the leveling measurements projected onto the LOS in case the deformation is only vertical - see Fig. 3-31 and related text for more details. Source:?

59

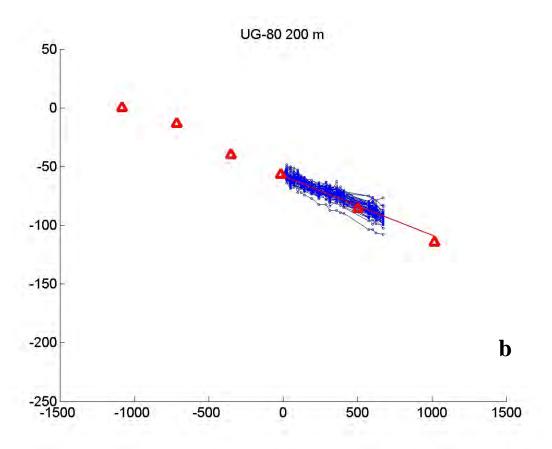


Figure 3-29. Continued (b). Source: ?

Note in Fig. 3-29b that more PS data are captured within 200 m from the benchmark than within 100 m, and they spread out more, which is not unexpected. The difference is small for this particular benchmark. Examples of larger differences can be found in Appendix A. The PS measurements (blue lines and dotes) in Fig. 3-29 agree very well with the leveling data projected onto the LOS (red line), and the noise level is very low. For this particular benchmark, the average LOS rates from the PS within 100 m is -19.1 mm/yr and from the PS within 200 m is -18.8 mm/yr, a statistically insignificant difference. The leveling change at UG-80 is -20.39 ± 0.55 mm/yr and thus, in the LOS direction for the ascending geometry (see Table 3-2-6), after a multiplication by $\cos\delta$ =0.90, is -18.35 mm/yr. This is the value with which the PS rates have to be compared, and they are not different by any significant amount. Since only vertical motion is assumed for the benchmark (red line), this means that for all practical purposes, in the ascending geometry, there is no obvious indication for horizontal movements.

Fig. 3-30 shows the same type of comparison as in Fig. 3-29, and for the same benchmark (UG-80), but with the descending PS points. In this case the PS data are also rather tightly clustered around the benchmark leveling data projected onto the LOS direction (red line). In Fig. 3-30 the red line is more obviously above the leveling measurements (red triangles) compared with Fig. 3-29, because the descending geometry captures a

smaller portion of the vertical movement. From Tables 3-2-6 and 3-2-7 above, it is easy to see that vertical movements are projected onto the LOS with a factor of 0.69 for the descending orbit. This is comparable to the factor for the east component, 0.71 (i.e., capturing a W-E horizontal movement) that is quite larger than the same factor for the ascending orbit, 0.42. So, the leveling rate of –20.39 mm/yr is projected onto the LOS direction for the descending geometry as –14.07 mm/yr. The rates from the PS points are –10.34 mm/yr and –10.56 mm/yr within 100 m and 200 m from the benchmark, respectively. (The 200 m version is not shown in Fig. 3-30, because it looks the same as that shown for 100 m.) Thus, for the descending geometry, the PS curves (blue lines) remain above the LOS leveling curve (red line), i.e., with smaller slopes, which is somewhat visible in Fig. 3-30. As it will become clear from Figure 3-31 below, this indicates a movement eastward.

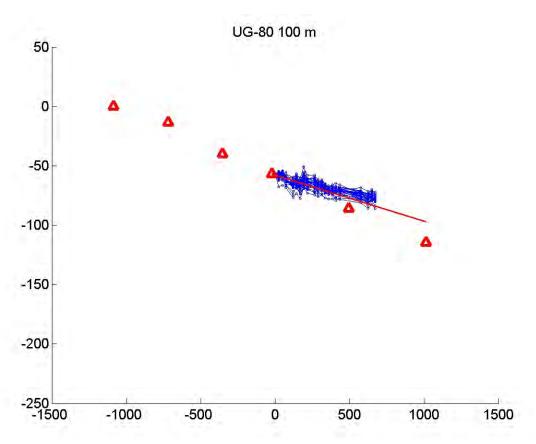


Figure 3-30. Same as Fig. 3-29, but with the descending PS points within 100 m from UG-80. This is very similar to the plot with PS within 200 m (not shown). Source:

The results presented in Figs. 3-29 and 3-30 are representative of the results for most other benchmarks in terms of the very good match between the leveling rates and the PS deformation rates and can be thus considered rather typical for the RADARSAT results. (See Appendices A and B). In addition, a number of the PS points are away from benchmarks and still show similar smooth deformation changes with little noise. This validates the value of the PS InSAR to probe areas that are not surveyed in any other way.

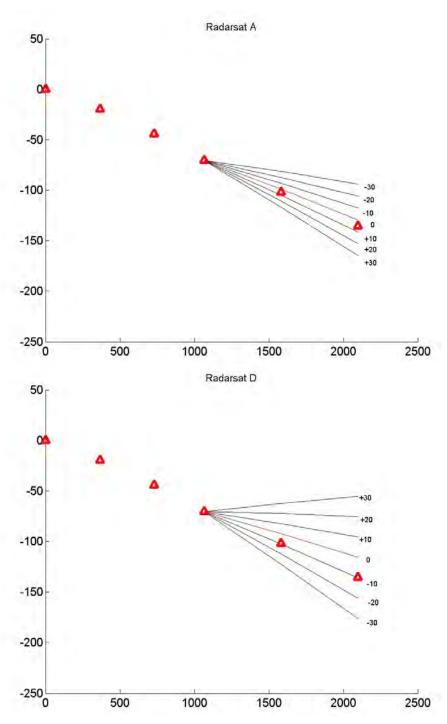


Figure 3-31. Projection of the leveling data (red triangles) onto RADARSAT LOS (red and blue lines). The numbers marking the different curves indicate hypothetical horizontal W-E movements in mm/yr, with positive numbers for movements to the east and negative numbers for movements to the west. Top - ascending, bottom - descending.

Figs. 3-29 and 3-30 showed the projection of the leveling data onto the LOS (red lines), assuming that the benchmark moves only vertically. However, as it has become clear in Section 3.1, it is quite possible that a horizontal movement also takes place for both the benchmark and the PS points. Figure 3-31 shows schematically how the projected LOS

rates change for the same vertical movement as indicated by the leveling measurements, but for different hypothetical horizontal movements to the east and to the west. The ascending geometry is shown on top of Fig.3-31 and the descending on the bottom. The spread is larger for the descending geometry because it is more sensitive to W-E movements (factor 0.69 for descending vs. 0.42 for ascending – see Tables 3-2-6 and 3-2-7). The LOS projection assuming only vertical movement (i.e., W-E horizontal movement is 0 mm) is the same as the red lines shown in Figs. 3-29 and 3-30, as well as in all figures in Appendices A and B.

In view of the above, if the PS points around a given benchmark align closely onto the red lines for both the ascending and descending geometries, it is reasonable to assume that the movement is mostly vertical. However, if there is some deviation from the red line, especially in the descending case where the W-E movement is captured more sensitively, one could use these models to estimate the possible W-E movements. Thus from the models shown in Fig. 3-31, it follows that Fig. 3-30 indicates eastward movement at that particular benchmark, as suggested by the smaller slopes of the blue curves versus that of the red line. As a reminder, all considerations so far remain relative to S-1246.

In Fig. 3-31 it is interesting to observe how complex the interplay between vertical and horizontal movements can be. The benchmark leveling rate in this example is –24.2 mm/yr, for which the LOS projection is –16.70 mm/yr. Note that for the descending geometry, the addition of a hypothetical eastward horizontal movement of +30 mm/yr (eastward) results in a LOS movement towards the satellite (i.e., the "+30" line is with a positive slope), while all other lines indicate a LOS movement away from the satellite.

Figure 3-32 shows maps of the differences between the LOS leveling rates assuming only vertical movement and the PS deformation rates, for all benchmarks with PS points within 200 m. The differences were first calculated in LOS and then projected on W-E. They are thus indicative of W-E horizontal movements in the vicinity of the benchmarks. Both the ascending and descending geometries are represented in the figure. Ideally, W-E components deduced from either the ascending or descending PS in the vicinities of the benchmarks should be the same. However, the descending geometry is more sensitive in this respect. The overall patterns from the two geometries are similar, and for the most part westward movements are grouped separately from the eastward movements, as it should be. However, there are some exceptions that would need further investigation. These plots represent a different way of presenting the more detailed information previously shown in Fig. 3-28 (using only PS points), with a focus here on the vicinities of benchmarks. The overall patterns of eastward and westward movements are similar between the two figures (Figs. 3-32 and Fig. 3-28), as expected.

In addition, in Section 3.1 an extensional model was deduced from the regional tectonic movements, indicating W-E movements between –1to –2 mm/yr (i.e., to the west) in the western part of Fig. 3-1-3 and up to +5 mm/yr (i.e., to the east) in a large part of that plot,

with increasing values eastward. Obviously horizontal movements associated with the geothermal activity would be superimposed on the regional movements – they are likely to be larger and in places, in the opposite direction of the tectonic movements, due to the traction of the overall subsidence in the geothermal field.

In view of the above, it is reasonable to assume that by bringing together the RADAR-SAT PSInSARTM results, ground-based leveling data, and GPS measurements, a more detailed model is possible for quantifying the interplay between regional tectonics and geothermally induced local movements in both the vertical and horizontal directions. However, this vast subject falls outside the scope of this report.

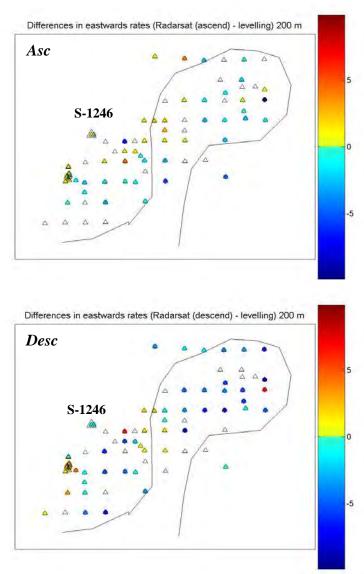


Figure 3-32. Differences between the leveling rates projected onto the LOS and the deformation rates of the PS points within 200 m from benchmarks. These differences are indicative of W-E horizontal movements. Top – ascending, bottom – descending. Benchmarks are marked with triangles. Empty triangles mean that there are no PS points within 200 m of the benchmarks. Color scale is in mm/yr. Blue colors and red-yellow colors indicate westward and eastward movements, respectively. Source:?

3.3. Results From C-band ENVISAT Data (ASAR)

Similar to the RADARSAT data, ENVISAT ASAR scenes were identified for the Salton Sea area collected from both ascending (tracks 77 and 306) and descending (tracks 84 and 356) orbits (Figure 3-33). A total of 141 scenes were ordered from the European Space Agency, as part of an approved Category-1 research data proposal. More challenges were encountered with the ENVISAT data than with the RADARSAT data. This difference is most likely due to the specific application of the PSI techniques used and not to the type of data, as the ENVISAT data are of a very high quality (Figure 3-34).

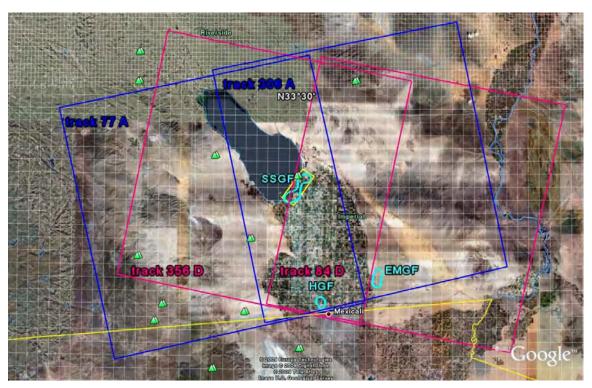


Figure 3-33. Footprints of the ASAR scenes superimposed on GoogleEarth imagery. The descending footprints (tracks 84 and 356) are shown with pink rectangles. The ascending footprints (tracks 77 and 306) are shown with blue rectangles. The outlines of the Salton Sea (SSGF), Heber (HGF) and East Mesa (EMGF) geothermal fields are shown with light blue. Yellow line shows the border between the United States and Mexico. The large water body is Salton Sea. Source:?

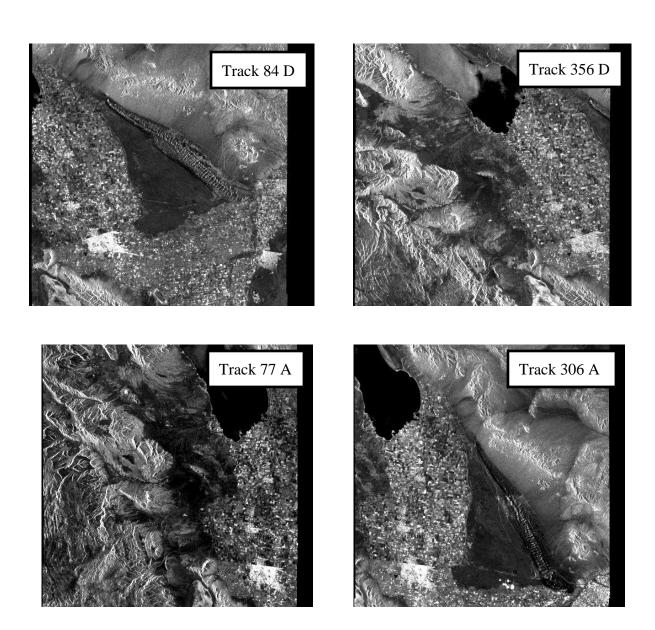


Figure 3-34. Examples of browse images from ASAR scenes from all available tracks - descending 84 and 356 and ascending 77 and 306. Footprints of the scenes are shown in Fig. 3-33. Source:?

Different InSAR applications were repeatedly attempted in order to improve on the results. Here two major attempts are discussed, featuring a PSI (permanent scatterers interferometry) technique and a SBAS (small baseline subsets) technique. Both of them were different from the PSInSAR™ method used for the RADARSAT data, including the PSI (PS interferometry) method, which although the same in concept (i.e., still using PS points), applied different algorithms. First, the PSI was used to analyze old ERS-1/2 data (1993-2000) and ENVISAT ASAR data from tracks 77 (ascending) and 84 (descending), covering the period from the beginning of ENVISAT data availability (in 2003) until mid-2007. A more recent application used longer time series of all available data, from 2003 until early 2009. Finally, a SBAS technique was also used on all available data from

tracks 77 (ascending) and 356 (descending). This last application yielded better results than the PSI, but still noisier than desired.

3.3.1. Results From the Application of the PSI Technique

Although this section describes mainly results from ENVISAT, it is worth reporting briefly on some results that were obtained from the analysis of older ERS-1/2 data (1993-2000). The first application of the PSI algorithm in this project featured these ERS data (from a descending orbit) and ENVISAT data between 2003 and mid-2007. For the latter period, 28 scenes of Track 84 (descending) and 27 scenes of Track 77 (ascending) were available. Not all of these images were used eventually, as this PSI application put a restriction of the maximum perpendicular baseline for the interferograms, in an effort to reduce noise. Table 3-3-1 shows some characteristics of the data used in this earliest application.

Table 3-3-1. Parameters of SAR scenes used in the PSI analysis

Orbit Information	ERS Track 356, Descending	ENVISAT Track 77, Ascending	ENVISAT Track 84, Descending
Start Date	2 Mar, 1993	30 Nov, 2003	4 May, 2003
End Date	15 Sep, 2000	4 Mar, 2007	4 Mar, 2007
Master Date	17 Aug, 1995	1 Aug, 2004	27 Feb, 2005
Number of Scenes Used	20	24	21
Largest Perpendicular Base- line	380 m	971 m	1264 m
Largest Temporal Baseline	1856 days	945 days	735 days
SCR Threshold	2.0	2.0	2.0

Source:?

Figure 3-35 shows an example of time series of interferograms obtained in this analysis. The PSI method used to identify PS points was first StaMPS (Hopper et al. 2004; Hooper and Zebker 2007), and then an improvement on it, a maximum-likelihood method (MLM) expected to identify more PS points (Shanker and Zebker 2007). Deformation rates at the PS points identified in the latter application are shown in Figure 3-36. They were extracted from the scenes listed in Table 3-3-1. Fig. 3-36 shows that a number of PS points were identified in and in between the agricultural fields of the study area (2163 descending PS and 726 ascending PS). Much more PS points were identified away from the agricultural areas (e.g., bottom left and top right corners of Fig. 3-36a). However, these PS points are away from the geothermal fields and are thus not of interest in this project. These relatively dry areas can be studied with regular DInSAR if necessary, and PSI application are likely not needed.

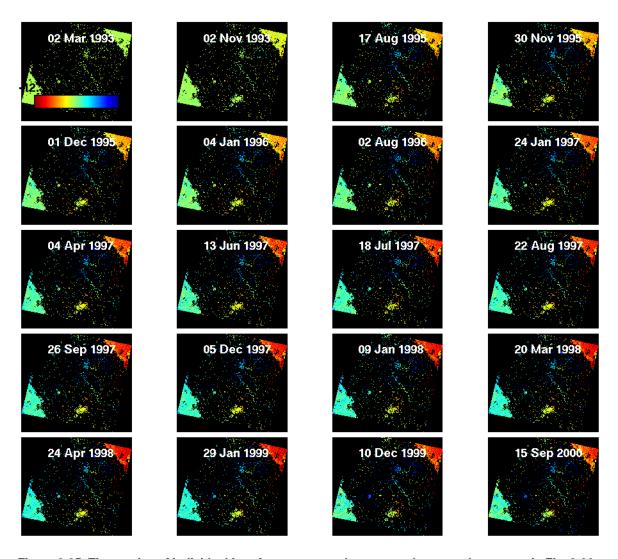


Figure 3-35. Time series of individual interferograms used to extract the rates shown next in Fig. 3-36a. Source:?

LOS Displacement Rate in mm/yr (1993-2000)

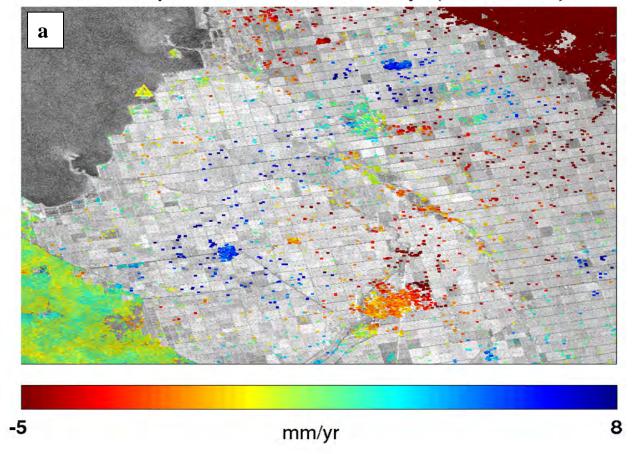
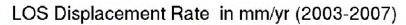
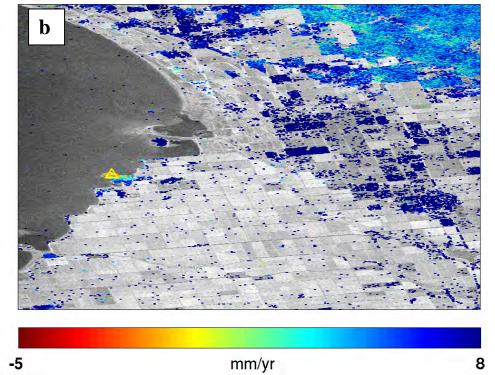


Figure 3-36. Surface deformation rates (mm/yr) in the LOS (line-of-sight) direction over the Salton Sea geothermal field, relative to S-1246 (yellow triangle). Colored points are permanent scatterers, PS. Negative values (red) imply movement towards the satellite, and positive values (blue) indicate movement away from the satellite, likely associated with subsidence. Extracted from (a) 1993-2000 ERS SAR, descending (track 356) data, look angle ~23°; (b) 2003-2207 ENVI-SAT ASAR, descending (track 84) scenes, look angle 21.7°; and (c) 2003-2007 ENVISAT ASAR, ascending (track 77) scenes, look angle 21.7°. Source:?





LOS Displacement Rate in mm/yr (2003-2007)

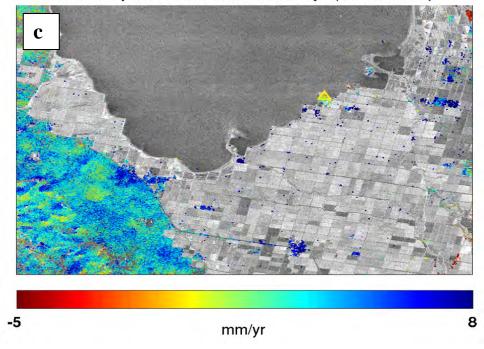


Figure 3-36. Continued (b) and (c). Source:?

The focus is placed next on the results from the ENVISAT ASAR data. The good news about these results is that a number of PS points were identified with steady deformation away from the satellite over time, just as expected in an area of predominant subsidence. Figure 3-37 shows an example where deformation rates from both descending and ascending PS points are compared with the leveling rates measured at nearby benchmarks. It is reassuring that steady movement is indicated over time away from the satellite in the LOS direction (likely mostly from subsidence), and that the results from the ascending and descending PS are similar. However, the LOS deformation rates derived from the ASAR are significantly lower than the rates from the benchmark leveling surveys. Because the look angle is so steep for the ASAR scenes, at δ =21.70 (both ascending and descending), the benchmark leveling rates projected onto LOS are decreased only by a factor of $\cos \delta$ = 0.93 and are thus not very different from the vertical deformation rates measured directly by the leveling. So, the differences between leveling and PS deformation rates cannot be accommodated by projecting on LOS.

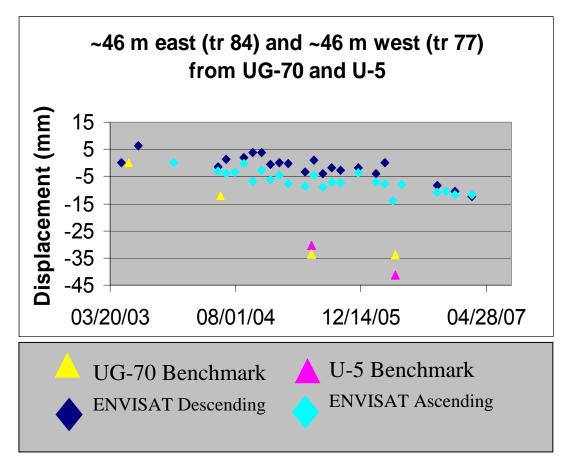


Figure 3-37. Example of subsidence measured at adjacent leveling benchmarks UG-70 and U-5, along with the nearest ENVISAT PS time series. Leveling data are also representative in the LOS direction due to the steep look angle (~22°).

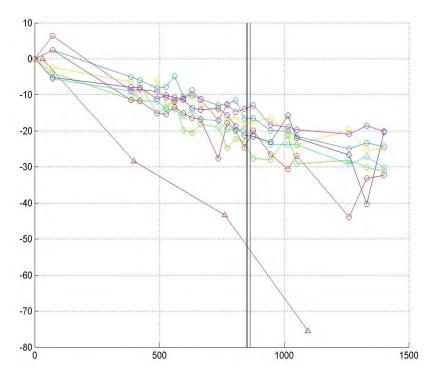


Figure 3-38. Time series of deformation (in mm) relative to S-1246). Horizontal axis is time measured in days since May 4, 2003. Benchmark observations are marked by triangles and descending PS measurements within 150 m of that benchmark are marked by lines and circles. Vertical lines mark the occurrence times of the M5.1 earthquake in September 2005 and associated fore- and aftershocks. Source:?

Similar discrepancies were observed for numerous other PS points. To simplify the comparison of PSI results and the leveling data, a linear regression was applied to the PS deformation time series for each PS point, and the respective LOS deformation rate was determined as the slope of the fitted straight line. Unlike the PS points determined for the RA-DARSAT data, a number of PS points in this PSI analysis are rather noisy and possibly random. The root mean squared error (RMSE) was used to rank the goodness-offit to straight lines and

only PS points with the least noisy time series were used for comparison with the deformation rates from leveling. Figure 3-38 shows an example of deformation time series for descending PS within 150 meters of a benchmark. The figure suggests that this benchmark subsides about twice faster than the descending PS points in its vicinity. This discrepancy is typical for other benchmarks as well. In addition, for any given benchmark, the ascending PS points in its neighborhood tend to show smaller deformation rates than the descending PS.

Figure 3-39 compares the benchmark deformation rates with the LOS deformation rates of the descending PS points, where the noisy PS (RMSE>6 mm/yr) are ignored. Two color scales are used for the PS (circles) and the benchmark (triangles) deformation rates. Since both are adjusted to the maxima and minima of their respective time series, the color hues can be directly compared to see if similar spatial patterns are suggested. The figure shows that, for most of the study area (except in its northeastern part), the spatial pattern of deformation is similar for the PS and the benchmarks. So, the differences are more systematic than random. Thus the PS results are still useful, albeit limited. Similar results are obtained for the ascending PS as well (not shown), although the difference

between PS and leveling rates is described by a different factor. Table 3-3-2 below shows estimates of the factors by which the PS and benchmark deformation rates differ.

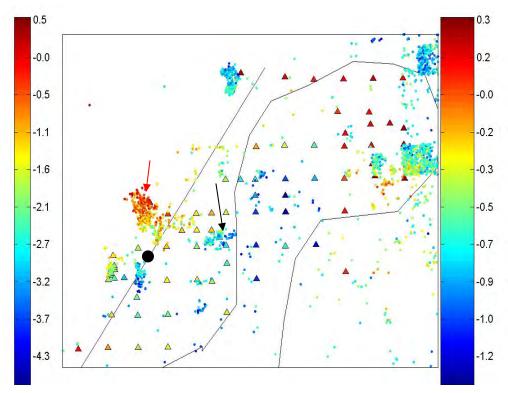


Figure 3-39. Deformation rates for benchmarks (triangles) and descending PS (circles). Only PS locations with RMSE < 6 mm/yr are plotted. Color scales on left and right show benchmark and mean PS deformation rates in cm/yr, respectively. Black circle shows M5.1 epicenter location. Gray line through it shows strike of earthquake swarm. Red arrow denotes location of the reference benchmark (S-1246). Black arrow points to a benchmark, whose deformation time series was shown in Figure 3-38.

Table 3-3-2. Factors describing the difference between leveling and PS rates

Orbit	maximum dis- tance (m)	b	95% CI of b
	300	1.62	(1.41, 1.84)
Ascending	100	1.31	(0.62, 2.01)
	50	1.91	(0.11, 3.70)
	300	2.40	(1.87, 2.93)
Descending	100	2.34	(2.08, 2.61)
	50	2.40	(1.87, 2.93)

Note: The table shows the slopes from the regression equations $\hat{y}=a+bx$, where \hat{y} are the benchmark deformation rates, and x is the observed mean of LOS deformation rates at PS locations within a specified distance from the benchmarks (300 m, 100 m, and 50 m). The 95% confidence intervals for b are shown in the last column. Source:?

Table 3-3-2 shows that the ratios of benchmark-to-PS rates over most of the study area are on average ~1.6 and ~2.4 for the ascending and descending PS points, respectively.

However, the northeastern part of the study area and two benchmarks to the southwest are exceptions.

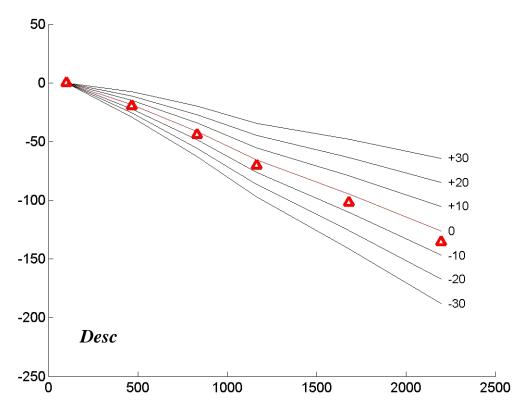


Figure 3-40. Projection of leveling data (red triangles) onto descending ENVISAT LOS (red and blue lines). The numbers marking the different curves indicate hypothetical horizontal W-E movements in mm/yr, with positive numbers for movements to the east and negative numbers for movements to the west.

Source:?

Similar to the analysis of the RADARSAT data, it is possible in principle to combine the information from the ascending and descending ENVISAT PS in order to resolve the vertical and the W-E horizontal motion. For the ENVISAT data, the sensitivities of the ascending and descending geometries to these movements are similar, with a factor of $\cos\delta$ =0.93, because the look angles in both geometries are δ =21.7 $^{\circ}$ (and not different like for the RADARSAT data). Figure 3-40 shows the sensitivity for the descending ENVI-SAT geometry, when hypothetical horizontal W-E movements are added to the vertical benchmark movements measured by the leveling. The appearance of the plot for the ascending geometry is the same (not shown): only the signs of the labels would be reversed. Both are similar to the RADARSAT ascending geometry (Fig. 3-31, top). The sensitivity to the W-E horizontal movements is measured with a factor of 0.36, i.e. close to twice lower than descending RADARSAT (0.69). Although such modeling was attempted, results are not shown due to the poor agreement between PSI deformation rates and the rates estimated from the benchmark leveling.

It was assumed that the discrepancies were due to inadequate unwrapping, so the hope was that improvements are possible in a next round of analysis, where more ASAR data were added to the time series after mid-2007 until early 2009. In general, PSI accuracy improves with longer time series. However, this did not happen in this study, and the desired results were not achieved. Instead, including more data worsened the disagreement between PS and leveling rates. For this reason, another approach, different from PSI was further attempted, SBAS, as described below.

3.3.2. Results From the Application of the SBAS Technique

In this case, all suitable ASAR data from ascending track 77 and descending track 356, covering the period March 2003-January 2009, were analyzed. An example of comparing SBAS and leveling rates is shown in Figure 3-41 (ascending) and 3-42 (descending). Instead of PS points, here SBAS cells of a 90-m spatial resolution are used. The example is for the same benchmark, UG-80, as in Figs. 3-29 and 3-30 showing the RADARSAT results in the previous section (Section 3.2). Appendices C and D include plots for all benchmarks, comparisons with the ascending and descending SBAS deformation rates, respectively.

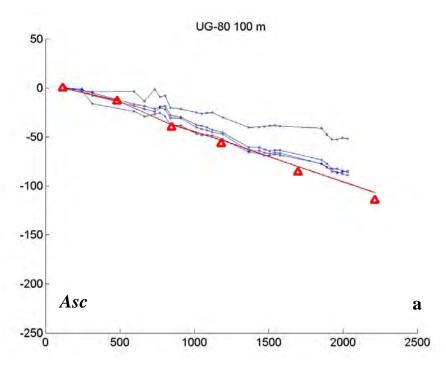


Figure 3-41. Comparison of the leveling data at benchmarkUG-80 and the SBAS ascending deformation time series within (a) 100 m and (b) 200 m from the benchmark. The horizontal axis shows days, starting from the time of the leveling survey in June 2003 and the first ASAR data used. The vertical axis shows surface change in mm. Blue lines and dots show data from the ENVISAT ascending SBAS results in the LOS direction. Red triangles show the leveling data (i.e, ground-based measurements of vertical deformation only). Red line shows the leveling measurements projected onto the LOS direction, assuming the deformation is only vertical. Refer to Fig. 3-40 for assumptions including horizontal movements.

Source:?

75

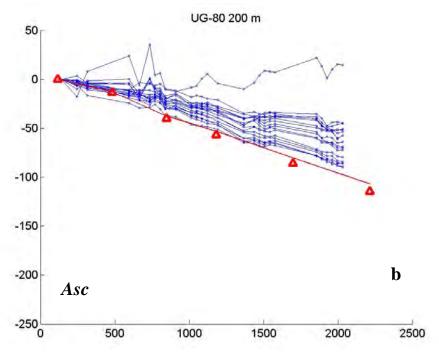


Figure 3-41. Continued (b). Source:?

Figure 3-41 shows that there are some SBAS cells near the benchmark with relatively good agreement with the LOS benchmark deformation (red line). However, the agreement rapidly deteriorates, and the spread that is seen does not necessarily correlate with distance; that is, even SBAS very close to the benchmark can exhibit very different rates, (See Fig. 3-41a, within 100 m.) Figure 3-42 shows the same as Fig. 3-41, but for the descending geometry. There is an improvement in this case, as the spread is smaller.

Although it is encouraging that some SBAS results agree with the leveling measurements, the example shown in Figs. 3-41 and 3-42 is among the best scenarios and is not particularly representative for other benchmarks. Plots like these two figures can be found in Appendices C and D for the remaining benchmarks.

Figure 3-43 shows velocity maps (deformation rates) calculated from the SBAS results. Although most features of the overall pattern agree with what is expected from previous results, many of the velocities are likely underestimated (i.e. SBAS slopes are often smaller than those of the red lines – see Figs. 3-41 and 3-42, as well as Appendices C and D).

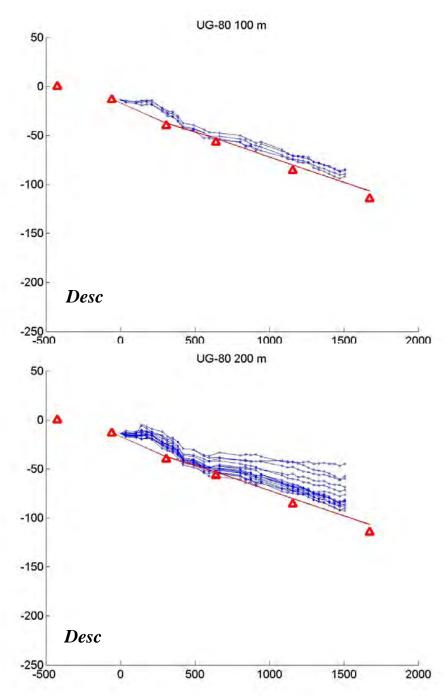


Figure 3-42. Same as Fig. 3-41, but for the descending orbits. Source:?

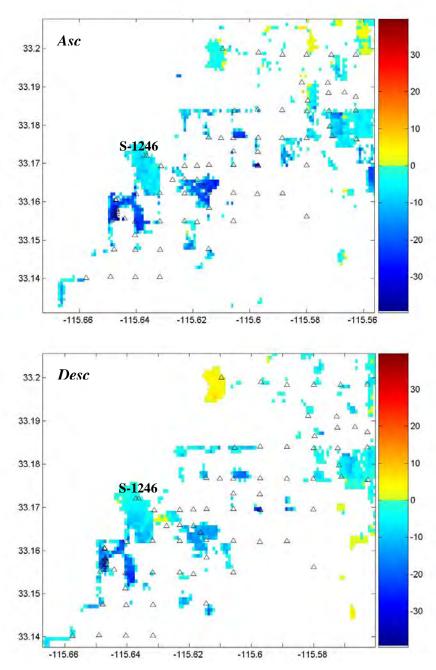


Figure 3-43. Maps of deformation rates at SBAS cells. Top – ascending, bottom – descending. Benchmarks are shown with triangles. Color scale marks LOS rates in mm/yr, referenced to S-1246. Source:?

3.4. Results from L-band PALSAR (ALOS Satellite)

The Advanced Land Observing Satellite (ALOS) is Japan's new-generation Earth Observation satellite, launched in January 2006 by the Japan Aerospace Exploration Agency – JAXA (e.g., Rosenqvist et al. 2007). In addition to two optical instruments, ALOS carries an L-band Synthetic Aperture Radar (SAR), the so called Phased Array L-band SAR (PALSAR). PALSAR is a successor of an earlier L-band SAR instrument onboard the Japanese Earth Resources Satellite (JERS-1) that operated in the period 1992-1998. Compared with JERS-1, the PALSAR instrument provides enhanced sensor characteristics, including full polarimetry, variable off-nadir viewing, and ScanSAR operations, as well as significantly improved radiometric and geometric performance. The ALOS repeat cycle is 46 days. After the initial calibration phase, the satellite started operating for real in October 2006, and since then PALSAR scenes have been available, including a number of images collected over Imperial Valley.

Because the longer wavelength (23.6 cm) of L-band penetrates vegetation much better than C-band, it was of great interest to attempt detecting surface deformation in the agricultural fields using regular differential InSAR (DInSAR). A number of data had been already collected in the period 11/05/2006 - 04/28/2008, from which 47 interferograms could be formed. Coherence turned out to be rather good in non-vegetated areas, like East Mesa, which is not surprising, because even C-band worked well in this area (Masonnet et al. 1997). However, the coherence turned out to be poor around the Salton Sea and Heber geothermal fields. Non-vegetated areas showed coherence for the longest time span available (~2 years), for perpendicular baselines < 1,500 m. Some phase fringes were visible for longer baselines as well (up to 3,600 m), but coherence was poor.

3.4.1. DInSAR Method

The freely available Sandwell/Mellors ALOS processing code (e.g., Price and Sandwell 1998) was used to create interferometric images from available ALOS data. The National Elevation dataset (NED) was used to correct for topographic effects. There are data collected over Imperial Valley from both descending and ascending orbits (Figure 3-44). The primary data used were of fine-beam single type (FBS – single polarization, 10-m resolution, 70-km swath). Fine-beam dual (FBD – dual polarization HH+HV20-m spatial resolution) data were also used when available. Table 3-4-1 shows the scenes used. Interferograms were also calculated from FBS-FBD and FBD-FBS combinations, but their quality is not good. All possible interferograms with similar polarization (HH) were generated, including FBD-FBS combinations achieved by over-sampling the FBD data in order to match the FBS data. Cross-polarimetric images (HH-HV) were also tested, but they showed lower coherence than HH-HH and are therefore not presented. Table 3-4-2 shows the interferograms formed and analyzed.

Due to the poor correlation in many interferograms, in an attempt to extract useful signal, considerable efforts were devoted to testing various filters and unwrapping schemes, especially near the Salton Sea and Heber geothermal fields.

3.4.2. Results

The East Mesa geothermal field, as well as the Cerro Prieto geothermal filed in Mexico to the south, were clearly imaged on several interferograms with time spans greater than 0.5 years. Figure 3-45 shows an example. Interferograms with a time span of 1 to 3 months showed no clear signal, even when correlation was excellent over East Mesa – likely because not much surface change occurs over such a short time span. Some indications were seen near the Heber geothermal field, but no specific signal could be extracted (Figure 3-46). It might have been possible to measure surface change if an interferometric pair existed with sufficient time span to create a measureable signal (e.g. > 0.75 year), yet short enough to allow correlation, as well as with a short vertical baseline (< 750 m). However, at present there was no such combination available, although it may be collected in the future as ALOS continues to be in operation.

Figure 3-47 shows results from the Salton Sea geothermal field. No signal could be captured here. The observation of linear streaks of high coherence suggests that it might be possible to monitor surface deformation along these streaks only. However, standard unwrapping and filtering techniques do not work for this purpose at present, even for L-band. Evidently, the longer wavelength of the L-band is less sensitive to the relatively small surface deformation, so a longer time span is necessary to capture a signal. However, this longer time span negates any improvement in coherence over time.

In summary, although clear signals could be seen over East Mesa and Cerro Prieto (where C-band has also worked before), the L-band PALSAR data from the ALOS satellite did not prove useful in the attempted DInSAR application to the geothermal fields in the vegetated areas.

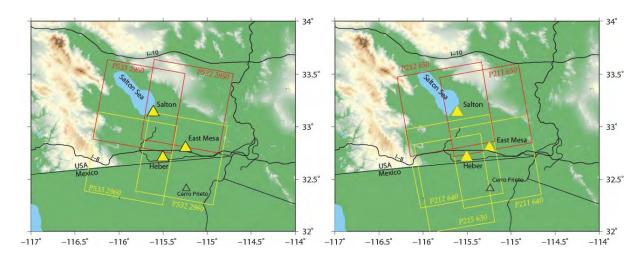


Figure 3-44.Maps showing coverage of descending data (left - paths 532 and 533) and ascending data (right - paths 211, 21, and 215). Yellow triangles denote geothermal areas in Imperial Valley. The open triangle shows the location of the Cerro Prieto geothermal field in Mexico.

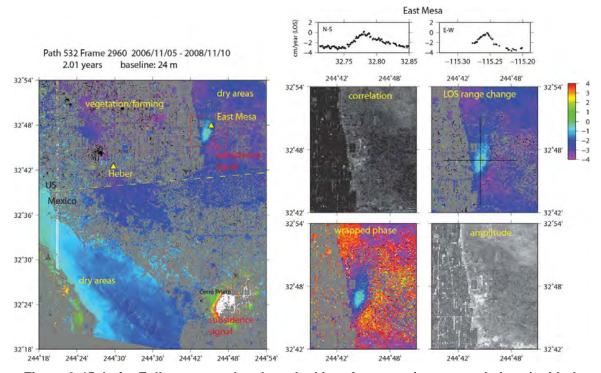


Figure 3-45. Left - Full unwrapped and masked interferogram (unwrapped phase) with the strongest signal observed. Subsidence signals associated with both East Mesa and Cerro Prieto in Mexico are clearly visible. Strong decorrelation exists over the vegetated areas, except for narrow streaks that are aligned with field edges, possibly associated with canals and streets. Right - Close-up of signal associated with the East Mesa field showing phase, correlation, amplitude, and LOS range change per year in cm/yr. The two plots on the top show deformation rates along S-N and a W-E profiles passing through the East Mesa geothermal field. Source:?

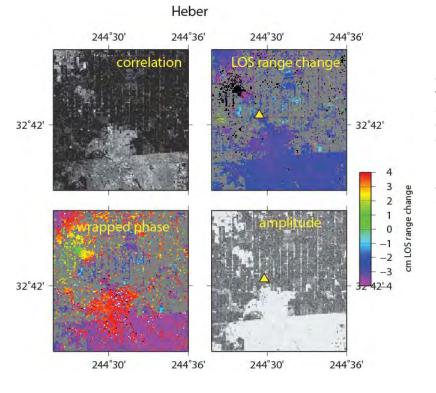


Figure 3-46. Image centered on the Heber geothermal field. The wrapped phase shows possible indications of subsidence, but it is not obvious in the unwrapped LOS signal, likely due to unwrapping difficulties in areas with isolated phase. Source:?



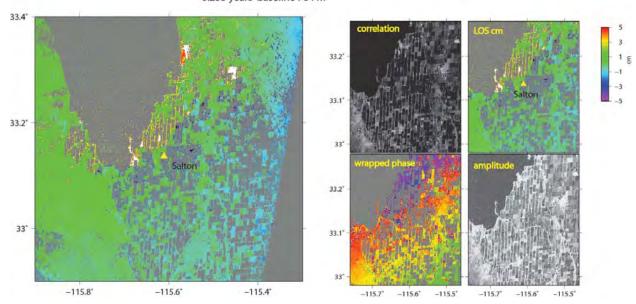


Figure 3-47. Interferogram covering the Salton Sea geothermal area. This area is particularly difficult to image due to rapid decorrelation over time. Farm fields seem to display varying elevations in images with correlation, possibly due to vegetation growth or variations in soil moisture.

Source:? Table 3-4-1. Primary ALOS data used in the study (A and D – ascending and descending orbits, respectively)

path	frame	orbit	beam	orb.	date	cen. lat	cen. long
211	640	10447	FBS	Α	JAN-10-2008 06:09:16	32.69	-115.15
211	640	7763	FBD	Α	JUL-10-2007 06:10:23	32.67	-115.15
211	640	5079	FBS	Α	JAN-07-2007 06:10:14	32.69	-115.19
211	650	10447	FBS	Α	JAN-10-2008 06:09:24	33.18	-115.25
211	650	7763	FBD	Α	JUL-10-2007 06:10:31	33.17	-115.26
211	650	5079	FBS	Α	JAN-07-2007 06:10:22	33.18	-115.29
212	640	12037	FBD	Α	APR-28-2008 06:09:47	32.69	-115.67
212	640	10024	FBS	Α	DEC-12-2007 06:11:41	32.66	-115.68
212	640	8682	FBD	Α	SEP-11-2007 06:12:20	32.67	-115.69
212	640	7340	FBD	Α	JUN-11-2007 06:12:34	32.67	-115.70
212	650	12037	FBD	Α	APR-28-2008 06:09:55	33.18	-115.77
212	650	10024	FBS	Α	DEC-12-2007 06:11:49	33.16	-115.78
212	650	8682	FBD	Α	SEP-11-2007 06:12:28	33.16	-115.79
212	650	7340	FBD	Α	JUN-11-2007 06:12:42	33.16	-115.80
532	2950	10877	FBS	D	FEB-08-2008 18:09:24	33.19	-115.22
532	2950	9535	FBS	D	NOV-08-2007 18:10:19	33.18	-115.21
532	2950	5509	FBD	D	FEB-05-2007 18:10:49	33.19	-115.19
532	2950	4167	FBS	D	NOV-05-2006 18:10:06	33.18	-115.18
532	2960	14903	FBS	D	NOV-10-2008 18:09:42	32.69	-115.28
532	2960	10877	FBS	D	FEB-08-2008 18:09:33	32.69	-115.32

532	2960	9535	FBS	D	NOV-08-2007 18:10:27	32.69	-115.31
532	2960	5509	FBD	D	FEB-05-2007 18:10:57	32.70	-115.30
532	2960	4167	FBS	D	NOV-05-2006 18:10:14	32.68	-115.28
533	2950	11125	FBS	D	FEB-25-2008 18:11:20	33.18	-115.76
533	2950	10454	FBS	D	JAN-10-2008 18:11:54	33.18	-115.75
533	2950	9783	FBS	D	NOV-25-2007 18:12:20	33.21	-115.74
533	2950	4415	FBS	D	NOV-22-2006 18:12:24	33.18	-115.71
533	2960	11125	FBS	D	FEB-25-2008 18:11:28	32.69	-115.86
533	2960	10454	FBS	D	JAN-10-2008 18:12:02	32.69	-115.85
533	2960	9783	FBS	D	NOV-25-2007 18:12:28	32.71	-115.84
533	2960	4415	FBS	D	NOV-22-2006 18:12:32	32.69	-115.82

Table 3-4-2. Interferograms generated

Path	Frame	Pair (yyyymmdd)	Time Span, yrs	Perp. Base (m)	Orb	Mode 1	Mode 2	Pol/angle
P532	2960	20061105_20081110	2.014	24	D	FBS	FBS	HH/34.3
P533	2960	20071125_20080110	0.129	275	D	FBS	FBS	HH/34.3
P533	2950	20071125_20080110	0.129	279	D	FBS	FBS	HH/34.3
P533	2960	20080110_20080225	0.126	489	D	FBS	FBS	HH/34.3
P533	2950	20080110_20080225	0.126	497	D	FBS	FBS	HH/34.3
P212	640	20070911_20071212	0.252	560	Α	FBD	FBS	HH/34.3
P212	650	20070911_20071212	0.252	568	Α	FBD	FBS	HH/34.3
P212	640	20070611_20070911	0.252	586	Α	FBD	FBD	HH/34.3
P212	650	20070611_20070911	0.252	588	Α	FBD	FBD	HH/34.3
P533	2960	20071125_20080225	0.255	765	D	FBS	FBS	HH/34.3
P533	2950	20071125_20080225	0.255	776	D	FBS	FBS	HH/34.3
P211	640	20070710_20080110	0.507	870	Α	FBD	FBS	HH/34.3
P211	650	20070710_20080110	0.507	884	Α	FBD	FBS	HH/34.3
P532	2960	20071108_20080208	0.254	946	D	FBS	FBS	HH/34.3
P532	2950	20071108_20080208	0.254	955	D	FBS	FBS	HH/34.3
P532	2960	20070205_20071108	0.756	1048	D	FBD	FBS	HH/34.3
P532	2950	20070205_20071108	0.756	1067	D	FBD	FBS	HH/34.3
P212	640	20070611_20071212	0.504	1146	Α	FBD	FBS	HH/34.3
P212	650	20070611_20071212	0.504	1156	Α	FBD	FBS	HH/34.3
P212	640	20071212_20080428	0.377	1439	Α	FBS	FBD	HH/34.3
P212	650	20071212_20080428	0.377	1452	Α	FBS	FBD	HH/34.3
P532	2960	20070205_20081110	1.762	-1641	D	FBD	FBS	HH/34.3
P532	2960	20061105_20070205	0.252	1655	D	FBS	FBD	HH/34.3
P532	2950	20061105_20070205	0.252	1659	D	FBS	FBD	HH/34.3
P212	640	20070911_20080428	0.629	1994	Α	FBD	FBD	HH/34.3
P532	2960	20070205_20080208	1.01	1994	D	FBD	FBS	HH/34.3
P212	650	20070911_20080428	0.629	2015	Α	FBD	FBD	HH/34.3
P532	2950	20070205_20080208	1.01	2022	D	FBD	FBS	HH/34.3
P211	640	20070107_20070710	0.504	2518	Α	FBS	FBD	HH/34.3

P211	650	20070107_20070710	0.504	2523	Α	FBS	FBD	HH/34.3
P212	640	20070611_20080428	0.881	2579	Α	FBD	FBD	HH/34.3
P212	650	20070611_20080428	0.881	2602	Α	FBD	FBD	HH/34.3
P532	2960	20061105_20071108	1.008	2703	D	FBS	FBS	HH/34.3
P532	2950	20061105_20071108	1.008	2726	D	FBS	FBS	HH/34.3
P533	2960	20061122_20071125	1.008	2940	D	FBS	FBS	HH/34.3
P533	2950	20061122_20071125	1.008	2960	D	FBS	FBS	HH/34.3
P533	2960	20061122_20080110	1.137	3215	D	FBS	FBS	HH/34.3
P533	2950	20061122_20080110	1.137	3239	D	FBS	FBS	HH/34.3
P211	640	20070107_20080110	1.011	3389	Α	FBS	FBS	HH/34.3
P211	650	20070107_20080110	1.011	3408	Α	FBS	FBS	HH/34.3
P532	2960	20061105_20080208	1.262	3649	D	FBS	FBS	HH/34.3
P532	2950	20061105_20080208	1.262	3681	D	FBS	FBS	HH/34.3

3.5. Potential of L-band UAVSAR

In this project, the initial intention was to demonstrate the use of airborne SAR in addition to SAR data collected from satellites. The airborne SAR instruments date back to the 1950's, starting from the military and moving onto the commercial scene. Details on airborne SAR are given in Jakowatz et al. (1996). It was previously assumed that while airborne InSAR is more accurate for topographic measurements than the spaceborne InSAR, DInSAR used for surface deformation works only from spaceborne platforms as in the absence of winds their trajectories are much more stable and better defined than those of airplanes. However, contemporary GPS systems make it quite possible to apply DInSAR using airborne data as well.

There exist a number of airborne SAR systems. An example of recent advances is the Lynx system, designed to be mounted on both manned and unmanned (e.g., Predator) aerial vehicles. The operating wavelength is ~2 (i.e., so-called Ku-band), providing ~10 cm resolution imagery at distances of up to 55 km, with the Lynx flown at an altitude of ~7,600 m. This fine resolution makes it possible to detect very small surface changes, such as footprints in sand. Most of the interest of the military for airborne SAR has stemmed from its capability to identify target movement with high accuracy.

In this project the initial intention was to have SAR airborne data collected by the above Ku-band system over a small area of the Imperial Valley for demonstration purposes. Such systems, however, are likely to be with limited applications for surface changes that take place over longer periods of time (e.g., 6-12 months), because loss of coherence occurs much faster for shorter wavelengths. Since it became clear in the beginning of the project that an L-band (i.e., much longer wavelength) airborne SAR system (Madsen et al. 2005) would become available as a result of a JPL project, UAVSAR (Uninhabited Aerial Vehicle), the research team changed its plans in the expectation that scenes will be collected over the Salton Sea area.

Although UAVSAR images have been indeed collected over the Salton Sea, they have not been made available yet to the public and thus their analysis could not be included in this report. However, future opportunities for data collection and analysis were discussed with the UAVSAR project's Principal Investigator Dr. Scott Hensley from JPL. For the time being, brief information on UAVSAR is provided here. The reader is referred for details to the UAVSAR website (http://uavsar.jpl.nasa.gov/).

The UAVSAR project has been funded by the NASA Earth Science Technology Office (ESTO). UAVSAR is a reconfigurable, polarimetric L-band synthetic aperture radar (SAR), specifically designed to acquire airborne repeat track SAR data for differential interferometric measurements of importance for the monitoring of dynamically changing phenomena. Using precision real-time GPS and a sensor controlled flight management system, the UAVSAR is able to fly predefined paths with great precision (within 10-m diameter tube around the desired flight track). The radar is fully polarimetric, with

a range bandwidth of 80 MHz (2-m range resolution), and supports a ~15 km range swath. The antenna is electronically steered along track to assure that the antenna beam can be directed independently, regardless of speed and wind direction. The UAVSAR system nominally operates at an altitude of 45,000 ft (13,800 m).

Planning flight lines for the UAVSAR Synthetic Aperture Radar (SAR) has to be done rather carefully. Like the spaceborne SAR systems, UAVSAR is a side-looking instrument, and thus, the location of the image swath is a function of the altitude of the instrument, the elevation of the ground, and the angle at which the desired swath is to be illuminated, as well as the swath width given by the radar operating mode. For the UAVSAR airborne instrument, the image swath is quite narrow (~ 16 km), so a relatively small error in position can result in missing a large portion of the desired image swath. UAVSAR collected the first data in September 2007. So far 37 past flight missions have been listed (http://uavsar.jpl.nasa.gov/past_flights.html). Several of these flights have been planned to include the Salton Sea geothermal plants: March 3 and March 21, 2008; May 16 and May 29, 2008. Future flights will also include coverage of the Salton Sea area, and it may be then possible to evaluate the capability of UAVSAR to capture surface deformation within the geothermal field.

An example from the May 3, 2008, flight is shown in Figure 3-48. The altitude of the flight was 12,497 m, the ground speed 221 m/s, the actual ground swath width \sim 22.46 km, and the look angles near and far range \sim 210 and 660, respectively.

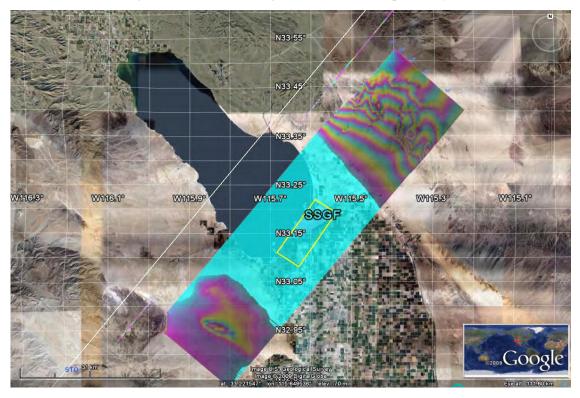


Figure 3-48. Example of UAVSAR coverage of Salton Sea from May 3, 2008. Yellow rectangle shows study area. Flight Line ID 22001 - http://uavsar.jpl.nasa.gov/flightplans/mar0308/.

4.0 Conclusions and Recommendations

In this project InSAR techniques were applied to satellite data from several sources in an effort to identify surface deformation within the geothermal fields of the Imperial Valley in Southern California. Despite some challenges, it was possible to extract valuable surface displacement information from the SAR data, using a permanent scatterer InSAR method (PSI). The research team is not aware of any similar published results prior to this project, possibly because the agricultural fields in the study region represent a significant obstacle to the application of any InSAR technique. To complicate the subject further, surface changes caused by the extraction of geothermal fluids in the Imperial Valley are superimposed on significant tectonic movements.

The analysis in this project turned out to be extensive and complex. Although very good results were obtained using one particular technique, a limited success with two other techniques was also achieved. Because of the extensive testing of various methods, and the emergence of various technical problems, only the area including the Salton Sea geothermal field was fully tested, for which all possible existing satellite data were analyzed. These included C-band SAR (i.e., 5.6-cm wavelength) data from the Canadian RADARSAT-1 and the European ENVISAT satellites, as well as L-band SAR (i.e., 23.6-cm wavelength) data from the Japanese ALOS satellite.

The particular PSI technique used with the C-band RADARSAT-1 data was PSInSAR™ (permanent scatterers interferometric synthetic aperture radar) developed and patented at Politecnico di Milano (Italy) and further improved at Tele-Rilevamento Europa (TRE), which participated in this part of the project. Interferometric techniques of the PS type make use of deformation time series extracted for numerous PS (permanent scatterers) points in the study area. They can work in vegetated areas where conventional DInSAR (differential InSAR) fails, especially for C-band data. The time series extracted from the PSInSAR $^{\text{TM}}$ analysis were compared with leveling data provided by *CalEnergy* operating the Salton Sea geothermal field. A very good agreement was obtained between these leveling data and the satellite results in the vicinity of most leveling benchmarks. Since RADARSAT-1 SAR data from both ascending and descending orbits have been collected in the period 2006-2008, the different viewing geometries made it possible to make inferences for horizontal movements in the west-east direction, in addition to the vertical movements. Data from GPS stations in the greater area of the Salton Sea were also used to get an idea of both horizontal and vertical tectonic movements, on which geothermally related displacements are superimposed. In particular, it was established that a reference benchmark used as a stable point for the leveling data is in fact likely moving both vertically and horizontally. This may be one of the reasons that although the RADAR-SAT-1 results obtained here are very good, the movements detected at PS points separated by small distances exhibit significant variability. Another major reason for such variability is the challenging conditions imposed by the extensive agriculture in the study area.

It is important to note that the PSInSAR™ technique applied here to the RADARSAT-1 SAR imagery is not at all data specific. As long as adequate time series of SAR scenes exist, it can be successfully used with any other C-band SAR data, such as those from the European ERS-1/2 and ENVISAT satellites, and even with the L-band data from the Japanese ALOS satellite.

The analysis of the C-band ENVISAT data carried out in this project included the application of two techniques. One of them was another PSI method, developed at Stanford University, using algorithms different from the technique applied to the RADARSAT-1 data. The second method was a SBAS (small baseline interferometry) technique. Although both methods have been very successful at identifying surface deformation time series in other study areas, the particular application in the agricultural area of the Salton Sea geothermal field had limited success in terms of match to the ground-based leveling data. These applications preceded the analysis of the RADARSAT-1 data in this project, and to a large extent, the unsatisfactory ENVISAT results prompted the research team to apply a different method with the RADARSAT scenes. However, it is most likely that neither the ENVISAT data nor the techniques applied in that case were intrinsically inferior. There are many skill- and experience-dependent steps included in this type of analysis, with subtleties and considerations to be taken into account. Given more time for multiple runs with varying parameters, it is reasonable to assume that the PSI method, and perhaps the SBAS technique, attempted here with the ENVISAT data, would eventually produce results comparable to those obtained with the RADARSAT-1 data using the PSInSARTM method.

In light of the above, the good results from the RADARSAT-1 data analysis in this project can serve as a generic proof of the concept, that is, that PS interferometry (PSI) can be successful in extracting informative and precise deformation time series from all existing C-band satellite data for this area. Moreover, even though only data collected over the Salton Sea geothermal field were analyzed in this project, there is nothing intrinsically different for the Heber geothermal field, in terms of similar coverage with agricultural fields. Therefore, PS interferometry is expected to be very successful at depicting surface deformation in both geothermal fields. As far as East Mesa is concerned, since it is in a dry non-vegetated area, conventional DInSAR works there as well, with both C- and L-band SAR data.

The above conclusion is important because the RADARSAT-1 data were collected over a limited two year time period (2006-2008) as part of a larger campaign that happened to include the Imperial Valley region. Such data are not being currently collected over Salton Sea and do not exist prior to 2006. Also, these data were used at no cost to this project as a special arrangement with the Alaska Satellite Facility (ASF), due to the research nature of the study. However, images from RADARSAT-1 are otherwise quite expensive. Thus even if it turns out that data acquisitions can be ordered from both RADARSAT-1 (to be decommissioned in 2012) and its successor RADARSAT-2 (already in

operation), this option may not be commercially attractive. The cost of a single standard RADARSAT-1 SAR scene like the 39 scenes used in this study is shown at \$3,600 CAD http://gs.mdacorporation.com/products/sensor/RADARSAT/rs1 price ca.asp). This is currently ~\$3,060 U.S. Although discounts are possible if buying scenes in bulk, the cost of data will still be high, especially with the addition of the cost of their analysis.

Therefore, if PS interferometry (PSI) is to be used in the future, the more viable commercial option is to purchase and analyze ENVISAT data that have been collected over the Imperial Valley since 2003 and continue to be collected. Such data will likely continue to be acquired also by ENVISAT's successor, the Sentinel satellite (planned for launch in 2011). The current commercial price of ENVISAT data is significantly lower than that of the RADARSAT data, and older data become cheaper with time. The current price list shows the cost of one ASAR scene at 400 Euro (currently ~\$540 U.S.) - price quote from http://www.eurimage.com. Discounts are available for multi-temporal and interferometry-related data.

Regular DInSAR analysis of L-band ALOS data was also attempted in this project, hoping to detect surface deformation because longer wavelengths penetrate vegetation much better than the shorter-wavelength C-band. Since DInSAR is not as computationally intensive as the PS interferometry methods, a much larger area could be studied in a reasonable amount of time, including all three operating geothermal fields in the Imperial Valley, and even the Cerro Prieto geothermal field further south in Mexico. No signals were detected over the Salton Sea and Heber geothermal fields. Deformation was detected in East Mesa and Cerro Prieto, but even C-band DInSAR has previously yielded results, due to the relatively dry and less vegetated surroundings of these geothermal fields. Since quite a few ALOS SAR (PALSAR) scenes have been and continue to be collected over the Imperial Valley, it may be possible in the future to detect deformation over Salton Sea and Heber by applying a PSI technique to these data as well. Mostly C-band PS interferometry applications have been reported in the literature, but if a time series of L-band ALOS data exists (at least 15 scenes), nothing precludes the application of the PS techniques to L-band. The price of the ALOS PALSAR data is comparable or lower than that of the ENVISAT ASAR data.

It is also conceivable that useful L-band SAR data from the airborne UAVSAR system may become available in the near future over the study area that might make it possible to detect surface deformation. With time, it is possible to envision collecting data on demand over areas of interest. If commercial systems of this type become available, their data will likely be more expensive than the data from the ENVISAT satellite and its successors. However, costs may decrease in the future with more widespread use and demand for such data.

The agricultural fields of the Imperial Valley rendered traditional DInSAR useless for C-band, but they presented a challenge even to the PSI techniques. So, it is reasonable to

expect that if PSInSARTM has worked under those challenging conditions, it will likely produce valuable results in most geothermal fields in other areas as well. For the purpose of continued monitoring using a PS interferometry technique, a plausible commercial scenario for any geothermal field is as follows. First acquire all, most, or some of the available ENVISAT data collected since 2003 as a one-time investment. Then purchase up to 10 scenes per year for each of a descending and ascending orbit (i.e., a total of up to 20 scenes), where available. This estimate is based on the fact that scenes can be only collected at 35-day intervals and not all data may be suitable for the analysis. However, in any case, there will likely be more scenes per year compared with only one annual leveling survey currently carried out at the geothermal fields of the Imperial Valley. The combination of ascending and descending ENVISAT data, where possible, can provide information on both horizontal and vertical movements, while the leveling measurements are only informative for the vertical movements at the benchmark locations. In the case of the Imperial Valley, data from both geometries have been so far available and will likely continue to be acquired even without special ordering. However, if necessary, future data acquisitions can be specifically ordered. In this scenario, once a year, both the data purchase and the PS interferometry processing, would be contracted out by the geothermal company interested in such analysis. The data processing would have to be performed by professionals specifically trained in such type of analysis. Not only commercial software is expensive, but the use of any algorithms of this type is rather complex and their application internally at the geothermal companies seems unlikely. This is especially true because such analysis is likely to be needed only once per year for any geothermal field.

It is conceivable that if satellite SAR data are available over an area of interest, as they are over the Imperial Valley, and a satisfactory density and spatial distribution of PS points is achieved, an annual PS interferometry processing of the newly accumulated SAR scenes each year can completely replace the need for leveling surveys. However, if PS analysis and ground-based measurements are to complement each other, it may be good to coordinate the installation of benchmarks in such a way, that more of them are placed where PS points are lacking, and fewer of them are installed where there is an abundance of PS points. Better yet, GPS stations can be installed in order to provide ground-based information on both vertical and horizontal movements, unlike the leveling measurements that reflect only the vertical movements. Even one GPS station to be used as a reference in a geothermal field can be very valuable. Furthermore, if PS points are lacking in areas of interest and it is desirable to increase their density, it is possible to create such PS by installing specifically designed objects, such as corner reflectors.

Most of the above recommendations are not specific to any particular geothermal field. A recommendation specific to the Salton Sea geothermal field concerns the choice of the benchmark used as a reference (S-1246) in the leveling surveys. The same point was assumed to be motionless also in the PS interferometry analyses, so that satellite results and leveling measurements could be compared. As discussed before, there is evidence

that this benchmark is not stable, but both subsides and moves horizontally. The amount by which S-1246 moves was deduced, with uncertainty, from the measurements at GPS stations outside the Salton Sea geothermal field and from a discrepancy between the relative measurements at another leveling benchmark (RED-1) and a nearby GPS station (P507 from the regional PBO GPS network). Since it is unlikely that a truly motionless point could be found in or near the geothermal field, perhaps it will be better to use RED-1 as reference in the future leveling surveys instead of S-1246. It is assumed that if absolute measurements were possible at RED-1, they would be very close to those registered at the nearby P507 GPS station.

In conclusion, permanent scatterer interferometry (PSI) appears to be a valuable and accurate tool for measuring deformation rates at geothermal fields, with the potential for much denser temporal and spatial coverage than that provided by ground-based measurements. It is thus recommended that geothermal operators look seriously into this new technology, as it is capable of providing better observations than those supplied by ground-based surveys. A comparative cost analysis is outside the scope of this project, but cost may be comparable between the two approaches or even lower for PS interferometry, while better coverage is achieved.

Since good results were obtained in a challenging agricultural area such as that where the Salton Sea geothermal field is located, it is reasonable to assume that most fields in vegetated areas of California can greatly benefit from the application of similar PSI techniques. Thus, this study is beneficial to the planning of deformation monitoring in any other geothermal fields in California, and in particular fields amidst vegetation, that might have been so far considered out of reach for InSAR.

5.0 References

- Analysis of Potential Surface Subsidence and Uplift From the Proposed Second Imperial Geothermal Project, Heber Geothermal Field, Imperial County, California, Environmental Management Associates Report No. 0432-01, 1992.
- Bell, J.W., F. Amelung, A. Ferretti, M. Bianchi, and F. Novali. "Permanent Scatterer In-SAR Reveals Seasonal and Long-Term Aquifer-System Response to Groundwater Pumping and Artificial Recharge." *Water Resources Research* **44**, W02407, doi:10.1029/2007WR006152, 2008.
- Bennet, R.A., W. Rodi, and R.E. Reilinger. "Global Positioning System Constrains on Fault Slip Rates in Southern California and Northern Baja, Mexico." *J. Geophys. Res.* **10**, 21943-21960, 1996.
- Berardino, P., G. Fornaro, R. Lanari, and E. Sansosti. "A New Algorithm for Surface Deformation monitoring Based on Small Baseline Differential SAR Interferograms." *IEEE Trans. Geosci. Remote Sensing* **40** (11), 2375-2383, 2002.
- Boardman, T.S., Roadlog. "Geothermal Resources in Coachella and Imperial Valleys." in *Geology and Geothermal Resources of the Imperial and Mexicali Valleys*, eds. L. Lindsay and W.G. Hample, San Diego Association of Geologists, 1998.
- Brune, J.N., and C.R. Allen. "A Low-Stress-Drop, Low Magnitude Earthquake and Surface Faulting The Imperial." California, Earthquake of March 4, 1966, *Bull. Seism. Soc. Amer.* 57, 501-514, 1967.
- Bürgmann, R., P. A. Rosen, and E. J. Fielding. "Synthetic Aperture Radar Interferometry to Measure Earth's Surface Topography and its Deformation." *Ann. Rev. Earth Planet. Sci.* **28**, 169-209, 2000.
- Bürgmann, R., G. Hilley, A. Ferretti, and F. Novali. "Resolving Vertical Tectonics in the San Francisco Bay Area from GPS and PSInSAR Analysis." *Geology* **34**, 221-224, 2006.
- Burroughs, C., Sandia, "General Atomics Unveil New Fine Resolution Synthetic Aperture Radar System," EurekAlert, Public Release date: 30 August, 1999.
- Carnec, C., and H. Fabriol. "Monitoring and Modeling Land Subsidence at the Cerro Prieto Geothermal Field, Baja California, Mexico, using SAR Interferometry." *J. Res. Lett.* **26**, 1211-1214, 1999.
- Elders, W.A., and J.H. Sass. "The Salton Sea Scientific Drilling Project." *J. Geophys. Res.* **93**, 12953-12968, 1988.
- Eneva, M. and Shanker, P. "Subsidence Monitoring in Imperial Valley, California Using Satellite Radar Interferometry." *Geothermal Research Council Trans.* **31**, 551-554, 2007.
- Eneva, M., D. Adams, G. Falorni, J. Allievi, and F. Novali. "Application of PSInSAR™ to the Detection of Surface Deformation in the Salton Sea Geothermal Field, Imperial Valley, California." *Geothermal Research Council Trans.* **33**, 2009 (accepted for publication).
- Erwin, S. I. Airborne radar: "Military Systems Redesigned for Commercial Applications." <u>National Defense</u>
 (http://nationaldefensemagazine.org/issues/2001/Aug/Airborne_Radar.htm), 2001.

- Ferretti, A., C. Prati, and F. Rocca. "Nonlinear Subsidence Rate Estimation Using Permanent Scatterers in Differential SAR Interferometry." *IEEE Trans. Geosci. Remote Sens.* **38**, 2202-1212, 2000.
- Ferretti, A., C. Prati, and C. Rocca. "Permanent Scatterers in SAR Interferometry." IEEE *Trans. Geosci. Remote Sens.* **39** (1), 8 –20, 2001.
- Ferretti, A., G. Savio, R. Barzaghi, A. Borghi, S. Musazzi, F. Novali, C. Prati, and F. Rocca (2007). "Sub-Millimeter Accuracy of InSAR Time Series: Experimental Validation." *IEEE Trans. Geosci. Remote Sens.* **45** (5), 1142–1153, 2007.
- Fialko, Y. "Interseismic Strain Accumulation and the Earthquake Potential on the Southern San Andreas Fault System." *Nature* **441**, doi:10.1038/nature04797, 968-971, 2006.
- Fialko, Y., and M. Simmons. "Deformation and Seismicity in the Coso Geothermal Area, Inyo County, California: Observations and Modeling Using Satellite Radar Interferometry." *J. Geophys. Res.* **105**, 21781-21793, 2000.
- Funning, G., R. Bürgmann, A. Ferretti, F. Novali, and A. Fumagalli. "Creep on the Rodgers Creek fault from PS-InSAR measurements, *Geophys." Res. Lett.* **34**, doi:10.1029/2007GL030836, 2007.
- Furuya, M., K. Mueller, and J. Wahr. "Active Salt Tectonics in the Needles District, Canyonlands (Utah) as Detected by Interferometric SAR and Point Target Analysis: 1992-2002." *J. Geophys, Res.* **112**, B06418, doi:10.1029/2006JB004302, 2007.
- Glowacka, E., and F.A. Nava. "Major Earthquakes in Mexicali Valley, Mexico, and Fluid Extraction at Cerro Prieto Geothermal Field." *Bull. Seism. Soc. Amer.* **86**, 1996.
- Glowacka, E., J. González, and H. Fabriol. "Recent Vertical Deformation in Mexicali Valley and its Relationship With Tectonics, Seismicity, and the Exploitation of the Cerro Prieto Geothermal Field, Mexico." *Pure Appl. Geophys.* **156**, 591-614, 1999.
- Hanssen, R.F. Radar Interferometry: Data Interpretation and Error Analysis, Kluwer Acad. Publ., London, 2001.
- Hirose, K., Y. Maruyama, D. Murdohardono, A. Effendi, and H. Z. Abidin. "Land Subsidence Detection Using JERS-1 SAR Interferometry." in *Proc.* 22nd Asian Conf. Rem. Sens., 5-9 November, Singapore, 2001.
- Hooper, A., H. Zebker, P. Segall, and B. Kampes. "A New Method for Measuring Deformation on Volcanoes and Other Natural Terrains Using InSAR Persistent Scatterers." *Geophys. Res. Lett.* **31**, doi:10.1029/2004GL021737, 2004.
- Hooper, A. and Zebker, H. (2007). "Phase Unwrapping in Three Dimensions with Application to InSAR Data." *JOSA A* **24** (9), 2737-2747, 2007.
- Hulen, J. B., and F. S. Pulka (2001). "Newly-discovered, Ancient Extrusive Rhyolite in the Salton Sea Geothermal Field, Imperial Valley, California" presented at 26th Workshop on Geothermal Reservoir Engineering, Stanford Univ., Stanford, Calif., 2001.
- Jakowatz, C.V. Jr., D.E. Wahl, P.H. Eichel, D.C. Ghiglia, and P.A. Thompson. "Spotlight-Mode Synthetic Aperture Radar: A Signal Processing Approach." Kluwer Academic Publishers, Boston, pp. 429, 1996.
- Johnson, C. E., and D. M. Hadley. "Tectonic Implications of the Brawley Earthquake Swarm, Imperial Valley, California, January 1975." *Bull. Seismol. Soc. Am.* **66**, 1133–1144, 1976.

- Lachenbruch, A.H., J.H. Sass, and S.P. Galanis, Jr. "Heat Flow in Southernmost California and the Origin of Salton Trough." J. Geophys. Res. 90, 6709-6736, 1985.
- Lauknes, T.R. Long-Term Surface Deformation Mapping Using Small-Baseline Differential SAR Interferograms. Ph.D. Thesis, Department of Physics, University of Tromsø, Norway, pp.100, 2004.
- Lohman, R. B., and J. J. McGuire. "Earthquake Swarms Driven by Aseismic Creep in the Salton Trough, California." *J. Geophys. Res.* **112**, B04405, doi:10.1029/2006JB004596, 2007.
- Madsen, S. N., S. Hensley, K. Wheeler, G. A. Sadowy, T. Miller, R. Muellerschoen, Y. Lou, and P. A. Rosen. "UAV-based L-band SAR with Precision Flight Path Control," in *Enabling Sensor and Platform Technologies for Spaceborne Remote Sensing, Proc. SPIE*, **5659**, Ed. Komar, G. J.; J. Wang, Jinxue, and T. Kimura, , pp. 51-60, 2005.
- Magistrale, H. "The Relation of the Southern San Jacinto Fault Zone to the Imperial and Cerro Prieto Faults," in *Contributions to Crustal Evolution of the Southwestern United States*, Ed. A. Barth, Geol. Soc. Amer Special Paper 365, 271-278, 2002.
- Massonnet, D. and K.L. Feigl. "Radar Interferometry and its Applications to Changes in the Earth's Surface." *Rev. Geophys.* **36**, 441-500, 1998.
- Massonnet, D., T. Holzer, and H. Vadon. "Land Subsidence Caused by the East Mesa Geothermal Field, California, Observed Using ASR Interferometry." *Geophys. Res. Lett.* **24**, 901-904, 1997.
- Mellors, R. J., and A. Boisvert. "Deformation Near the Coyote Creek Fault, Imperial County, California: Tectonic or Groundwater-Related?" *Geochemistry, Geophysics, and Geosystems* **4** (2), 1012, doi:10.1029/2001GC000254, 2003.
- Mossop, A., and P. Segall. "Subsidence at the Geysers Geothermal Field, N. California From a Comparison of GPS and Leveling Surveys." *Geophys. Res. Lett.* **24**, 1839-1842, 1997.
- Narasimhan, T.N., and K.P. Goyal. "Subsidence due to Geothermal Fluid Withdrawal, in *Man-Induced Land Subsidence*." Rev. Eng. Geol. VI, Geol, Soc. Amer., Boulder, CO, 35-66, 1984.
- Nikolaidis, R. *Observation of Geodetic and Seismic Deformation with the Global Positioning System*, Ph.D. Thesis, University of California, San Diego, 2002.
- Okada, Y. "Surface Deformation Due to Shear and Tensile Faults in a Half Space." *Bull. Seism. Soc. Am.* **75**, 1135-1154, 1985.
- Pepe, A., E. Sansosti, E., P. Berardino, and R. Lanari, "On The Generation of ERS/ENVISAT DInSAR Time-Series Via The SBAS Technique." *IEEE Geosci. Remote Sensing Lett.* **2** (3), 265- 269, doi: 10.1109/LGRS.2005.848497, 2005.
- Petersen, M.D., and S.G. Wesnousky, "Fault Slip Rates and Earthquake Histories for Active Faults in Southern California." *Bull. Seism. Soc. Amer.* **84** (5), 1608-1649, 1994.
- Petersen, M.D., L. Seeber, L.R. Sykes, J.L. Nabelek, J.G. Armbruster, J.Pacheco, and K.W. Hudnut. "Seismicity and Fault Interaction, Southern San Jacinto Fault Zone and Adjacent Faults, Southern California: Implications for Seismic Hazard." *Tectonics* **10**, 1187-1203, 1991.

- Price, E.J., and D.T. Sandwell. "Small-Scale Deformations Associated With the 1992 Landers, California, Earthquake Mapped by InSAR Phase Gradients." *J. Geophys. Res.* 11, 27,001-27,016, 1998.
- Rosen, P.A., S. Hensley, I.R. Joughin, F. Li, S.N. Madsen, E. Rodrigez, and R.M. Goldstein. "Synthetic Aperture Radar Interferometry." in *Proc. IEEE* **88**, 333-382, 2000.
- Rosenqvist, A., M. Shimada, N. Ito, and M. Watanabe. "ALOS PALSAR: A Pathfinder mission for global-scale monitoring of the environment." *IEEE Trans. Geosci. Remote Sens.*, **45** (11), 3307 3316, 2007.
- Scharroo, R. and P.N.A.M. Visser. "Precise Orbit Determination and Gravity Field Improvement for the ERS Satellites." *J. Geophys. Res.* **103** (C4), 8113 8127, 1998.
- Shanker, P. and Zebker, H. "Persistent Scatterer Selection Using Maximum Likelihood Estimation." *Geophys. Res. Lett.* **34**, L22301, doi:10.1029/2007GL030806, 2007.
- Signorotti, V., and C.C. Hunter. "Imperial Valley's Geothermal Resource Comes of Age." *Geoth. Res. Council Bull.* Sep/Oct, 277-288, 1992.
- Stancliffe, R.P.W., and M.W.A. van der Kooij. "The Use of Satellite-Based Radar Interferometry to Monitor Production Activity at the Cold Lake Heavy Oil Field, Alberta, Canada." *AAPG Bull.* **85**, 2001.
- Strozzi, T., L. Tosi, L. Carbognin, U. Wegmüller, and A. Galgaro. "Monitoring Land Subsidence in the Euganean Geothermal Basin with Differential SAR Interferometry." in *Proc. FRINGE'99, Liege, Belgium, 10 -12 November,* 1999.
- Sturz, A., D. German, and D. Putnam. "Salton Sea Geothermal Area Mud Pots: 1991-1998" in *Geology and Geothermal Resources of the Imperial and Mexicali Valleys*, eds. L. Lindsay and W.G. Hample, San Diego Association of Geologists, 1998.
- Wicks, C., W. Tatcher, F. Monastero, and M. Hasting. "Steady-State Deformation of the Coso Range, East-Central California, Inferred from Satellite Radar Interferometry." *J. Geophys. Res.* **106**, 13,769-13,780, 2001.
- Zebker, H.A., P.A. Rosen, R.M. Goldstein, A. Gabriel, and C. Werner. "On the Derivation of Coseismic Displacement Fields Using Differential Radar Interferometry: the Landers Earthquake." *J. Geophys. Res.* 99 (B10), 19,617-19,634, 1994.

APPENDICES

The following pages show individual plots for all leveling benchmarks used by *CalEnergy* at the Salton Sea geothermal field.

Horizontal axes show time in days, and vertical axes show displacement in mm. The 0 on the horizontal axes is around the time of the leveling survey closest to the time of the first SAR image used. The deformation at those times is considered 0, and all subsequent measurements are adjusted accordingly. The benchmark names are given in the plot titles. The red triangles in each plot show the time series of vertical movements recorded by leveling at the benchmark location, relative to the reference benchmark, S-1246. The leveling surveys have been performed in June 2003, June 2004, June 2005, May 2006, October 2007, and March 2009. Some of the red triangles may be missing in a leveling time series – this is when there is no measurement at this benchmark from the survey that year.

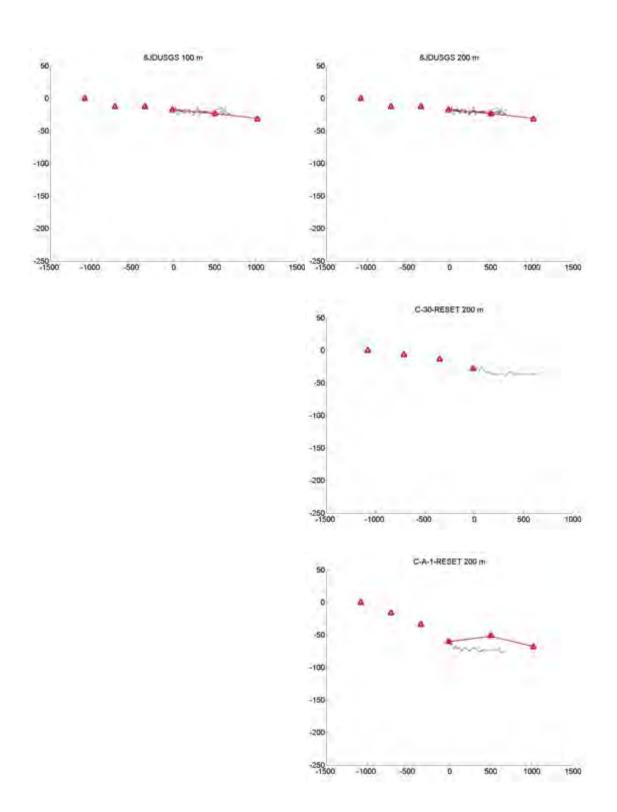
The blue lines trace InSAR measurements at times marked with blue dots, according to the dates of SAR data used in the analysis. The InSAR measurements are from PSIn-SAR™ for RADARSAT in Appendices A and B and SBAS for ENVISAT in Appendices C and D. These measurements are within 100 m (plots on the left) and 200 m (plots on the right) from the individual benchmarks. Like the benchmark leveling measurements, the InSAR measurements are referenced to S-1246. In time, they are referenced to the first one in the time series. In some cases, there are InSAR measurements within 200 m from a benchmark, but none within 100 m, so the plots on the right do not have counterparts on the left in these cases.

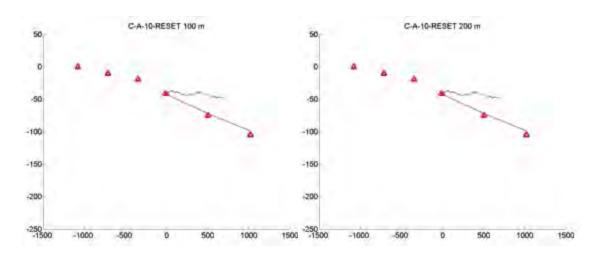
The solid red lines tracing the red triangles show the benchmark displacements projected onto the line-of-sight (LOS) direction to the satellite (d_{LOS}), provided that the benchmarks had only moved in the vertical direction (d_V) and not in the horizontal direction d_H =0). This makes it possible to compare the InSAR measurements with the leveling ones. Thus, d_{LOS} = d_V *cos δ , where δ is the look angle. The reason these lines are very close to the red triangles for ENVISAT ascending/descending and RADARSAT ascending, is because cos δ in those cases is close to 1 ($\cos\delta$ = 0.93 for ENVISAT and 0.90 for RADARSAT ascending), so that the displacement in the LOS direction is very close to that in the vertical direction There is a larger difference for RADARSAT descending, because in that case the displacement in the LOS is less sensitive to vertical motion ($\cos\delta$ = 0.69).

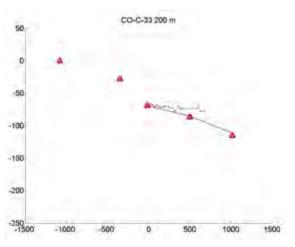
The best fit between the InSAR measurements and the leveling data is seen in the RA-DARSAT results. There are some good matches in the ENVISAT results as well, but the noise level is much higher. This is likely due to the very challenging study area, the different PSI techniques used, and the methods used for post-processing. In the future it should be possible to get results from ENVISAT that are comparable with those from RADARSAT.

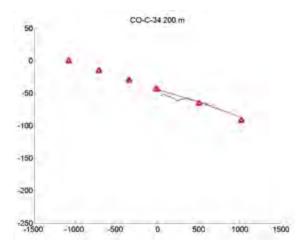
Note that RADARSAT data collected over the study area are available from only two years, April 2006-2008, while ENVISAT data are available since early 2003 and continue to be collected.

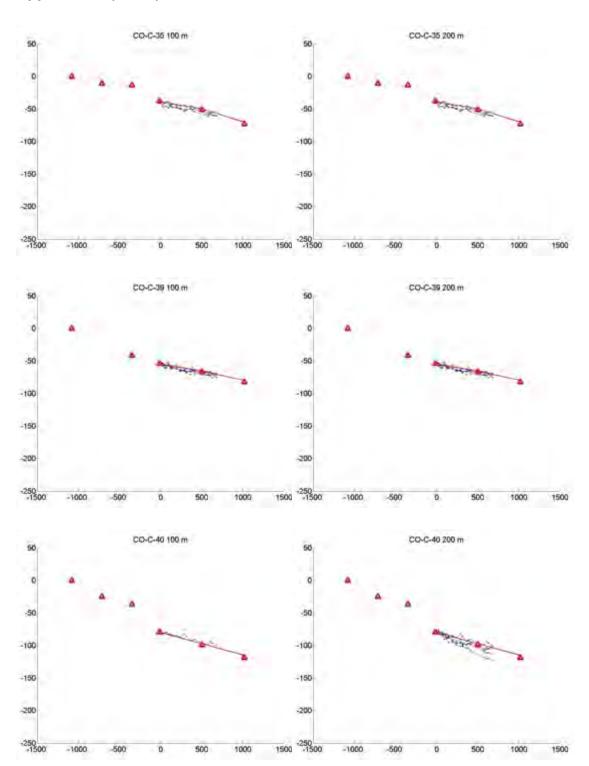
Appendix A. PS InSAR[™] results from the RADARSAT ascending orbit data

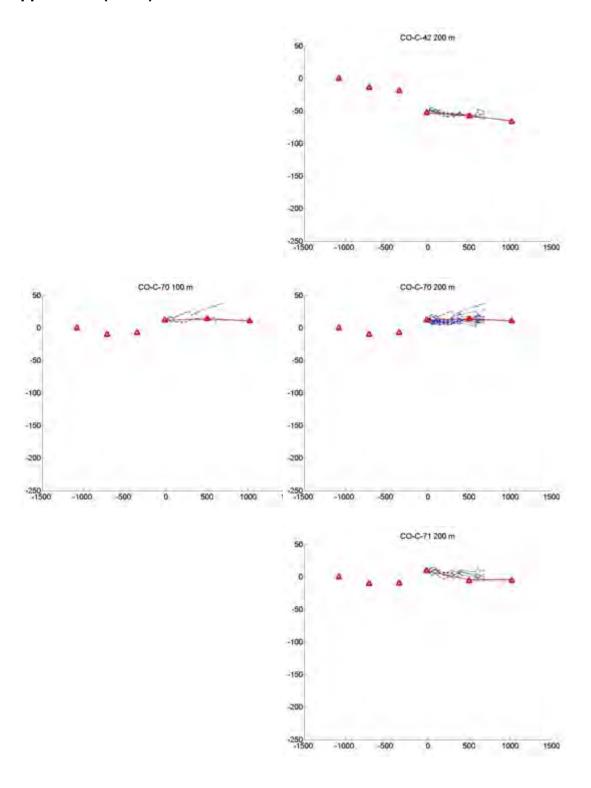


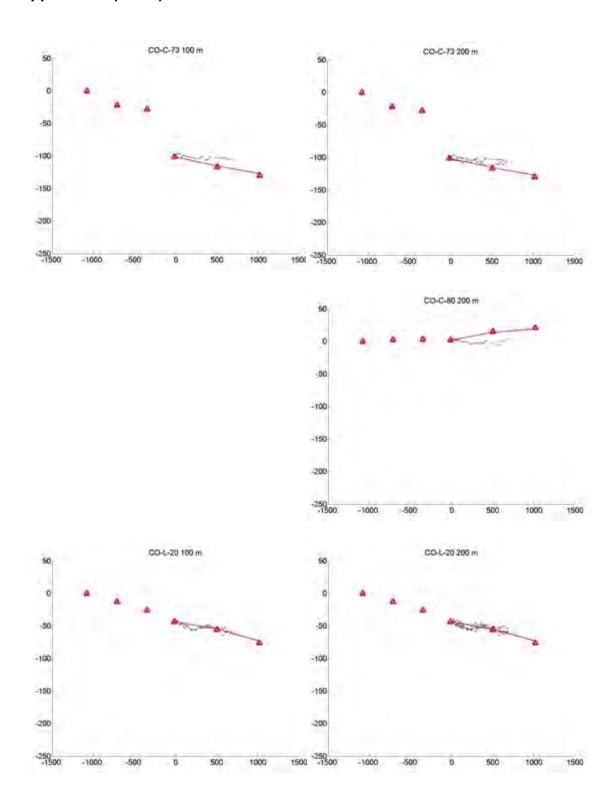


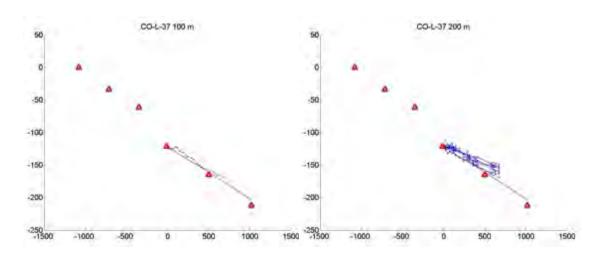


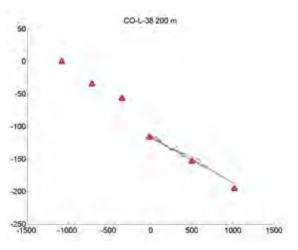


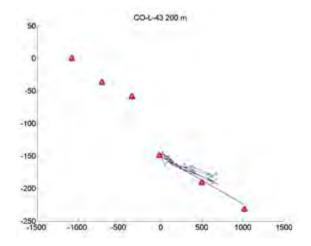


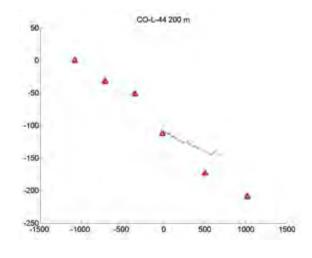


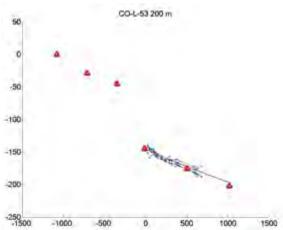


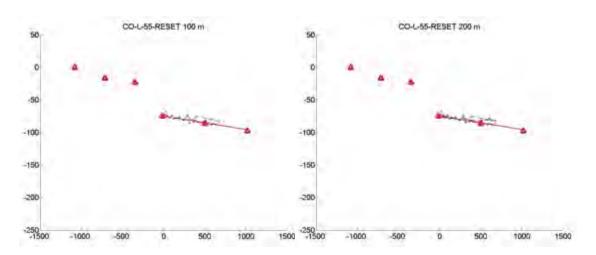


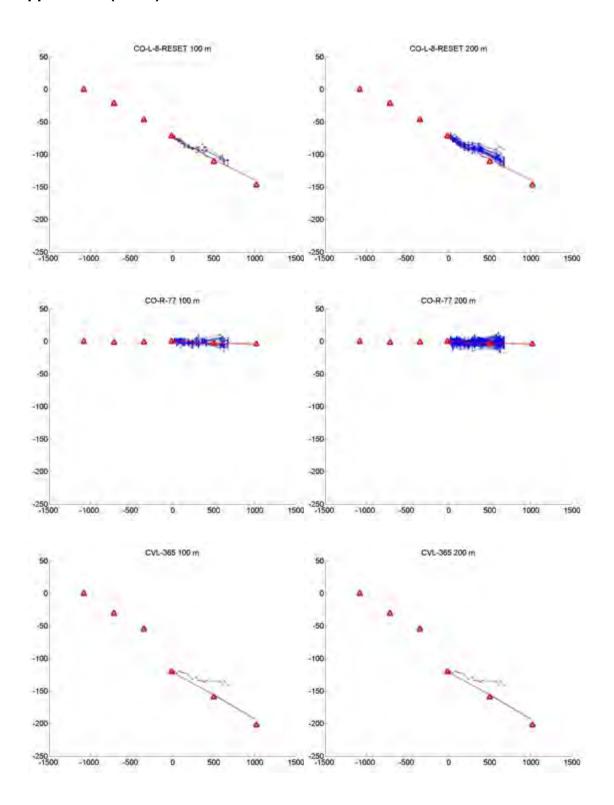


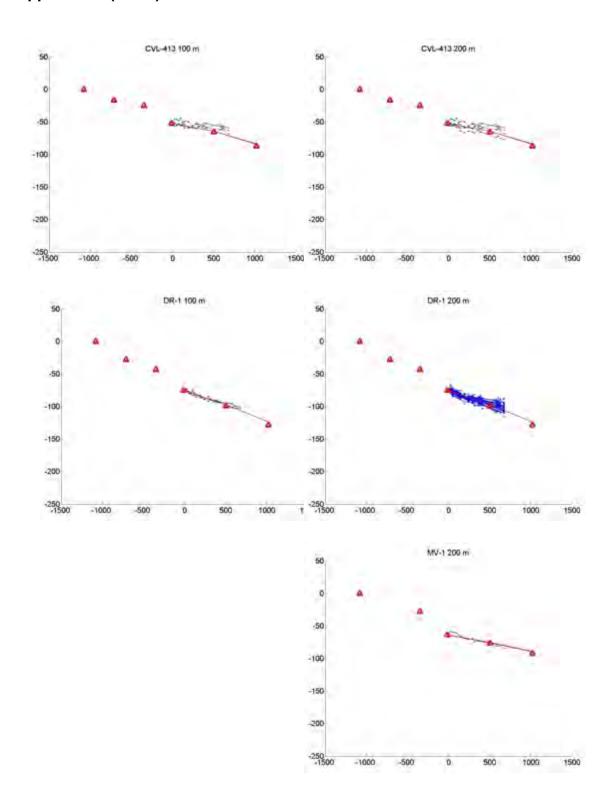


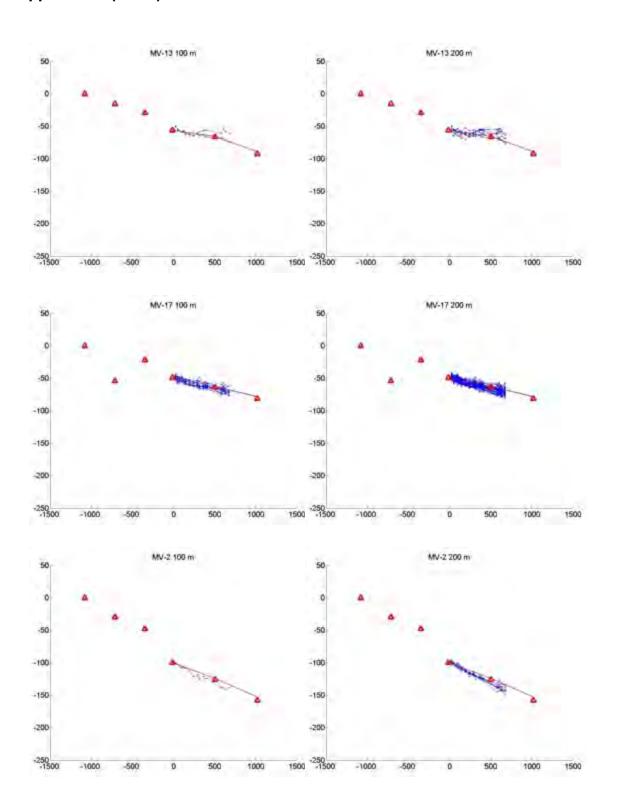


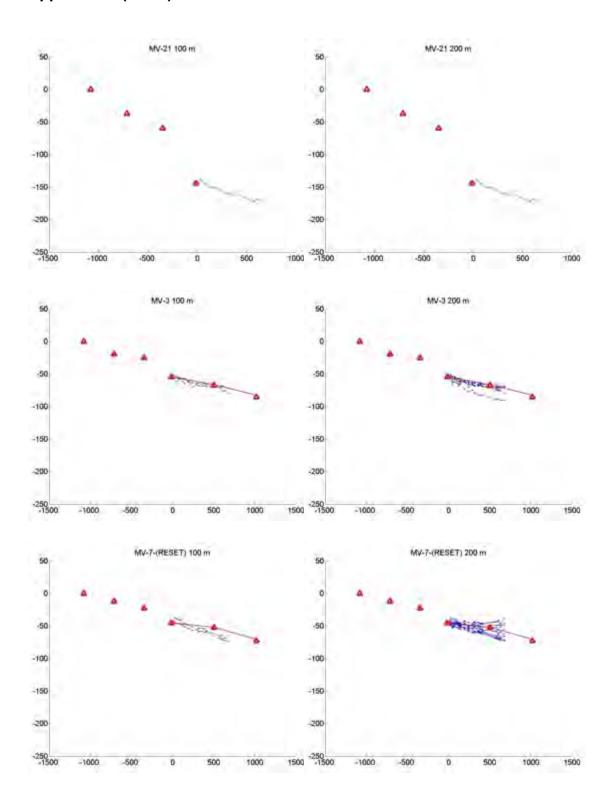


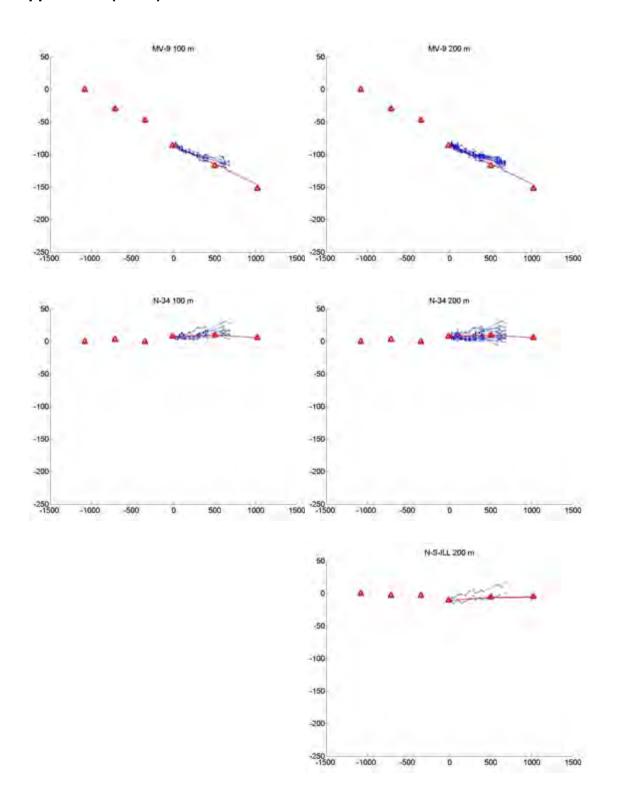


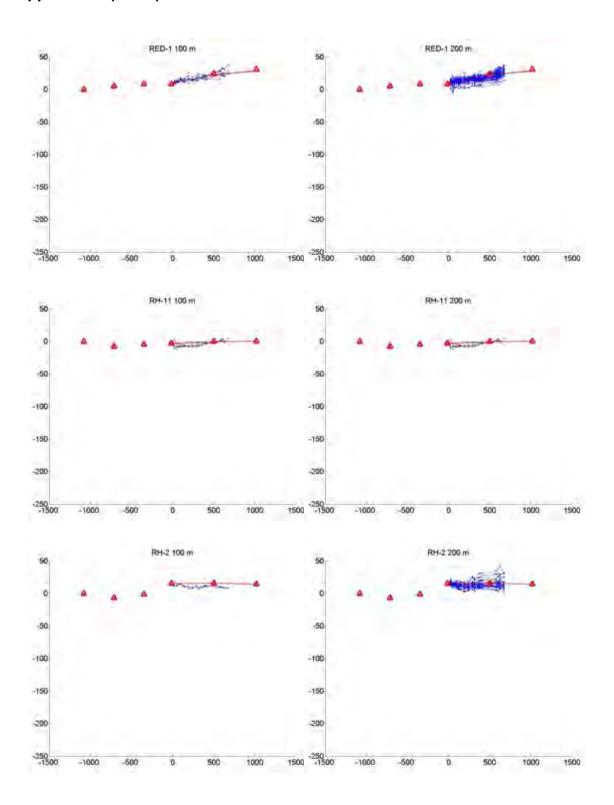


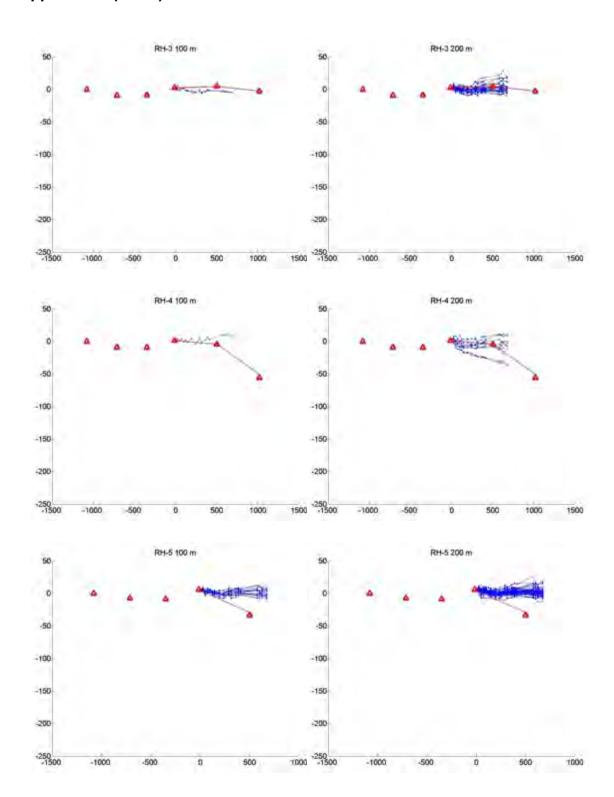


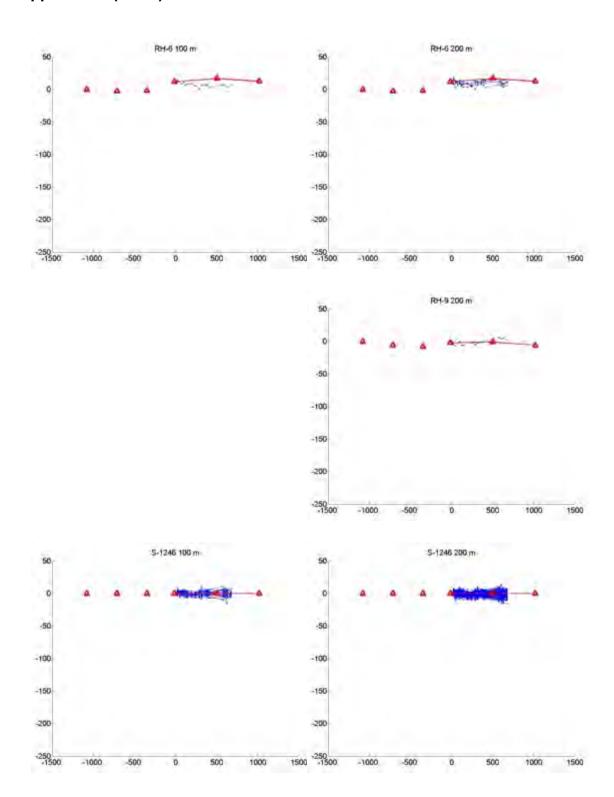


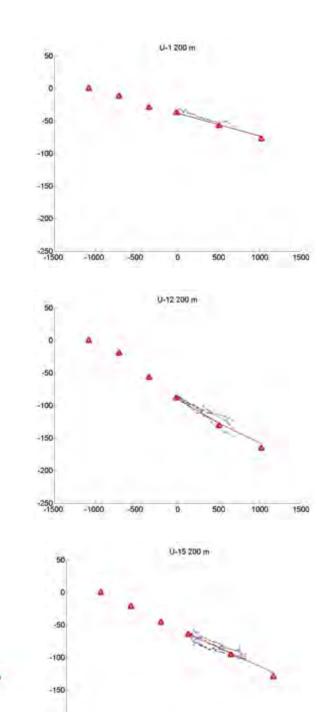












1000

-200

-250 -1500

-1000

-500

0

1000

1500

1500

U-15 100 m

50

0

-50

-100

-150

-200

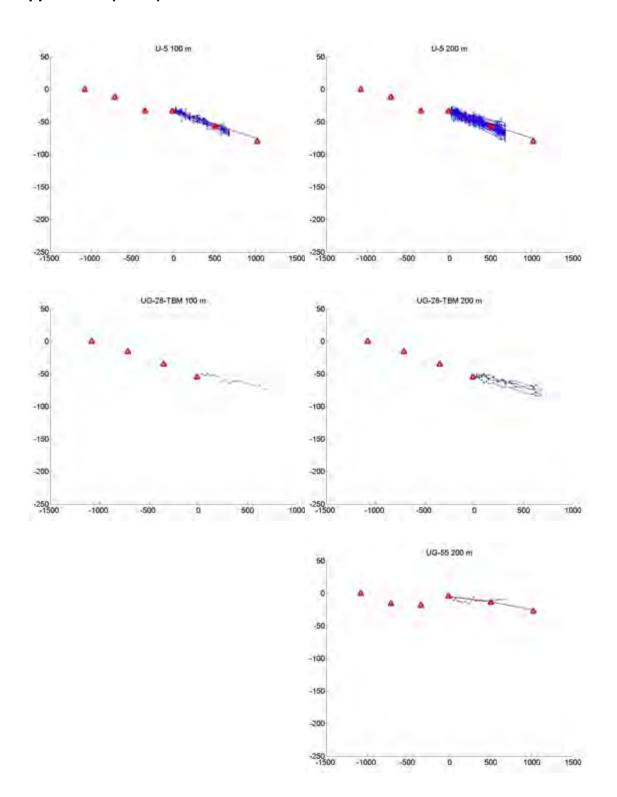
-250 -1500

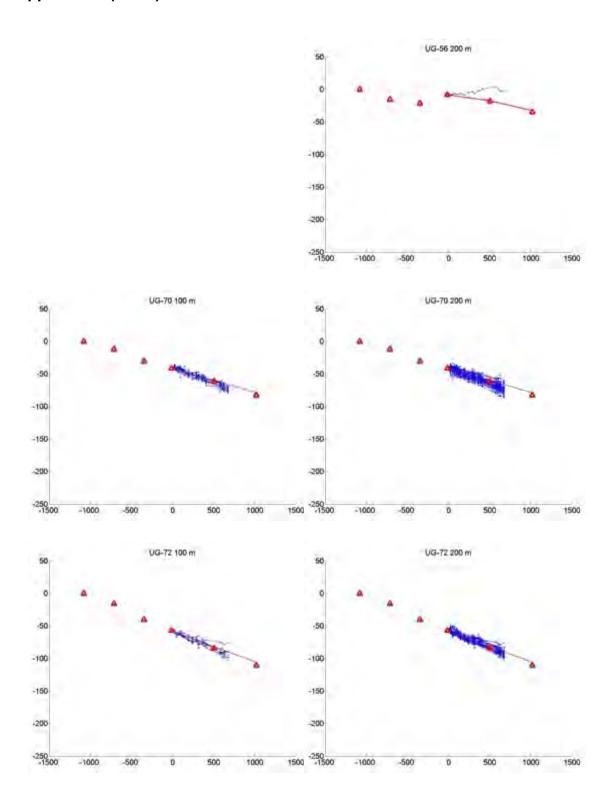
-1000

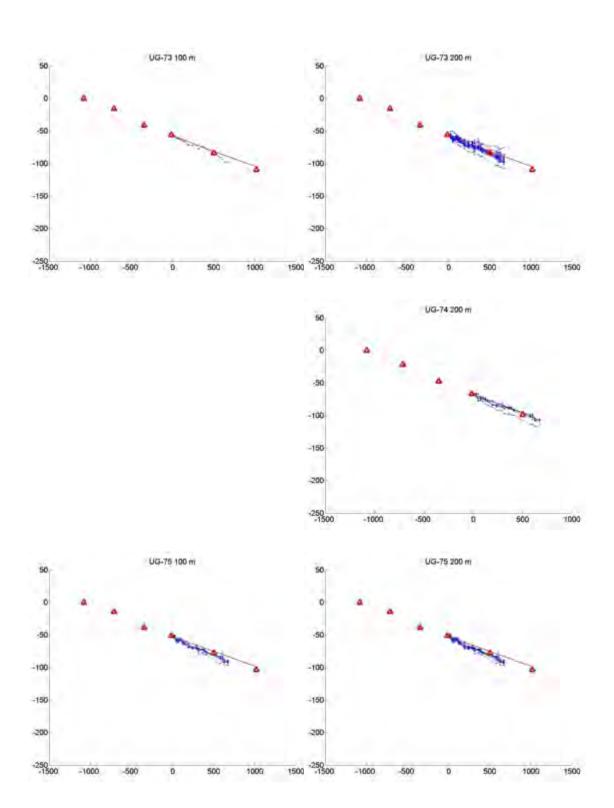
-500

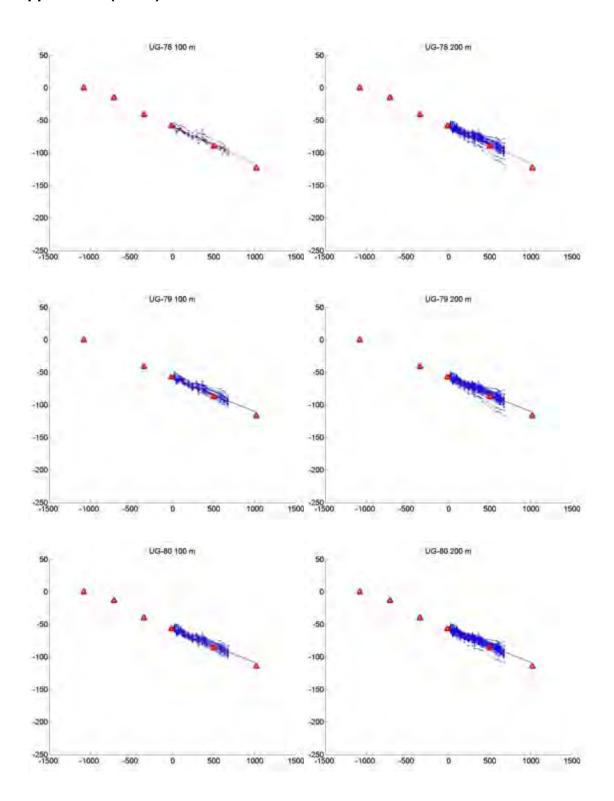
0

500

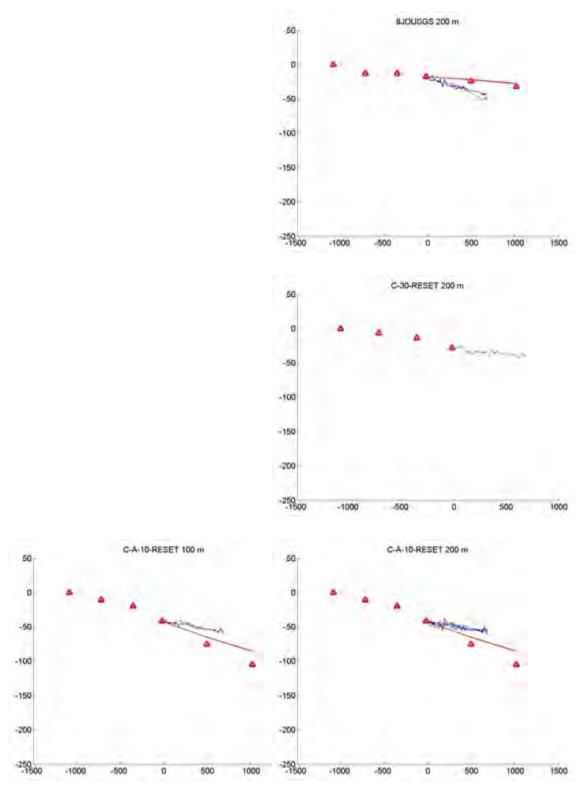


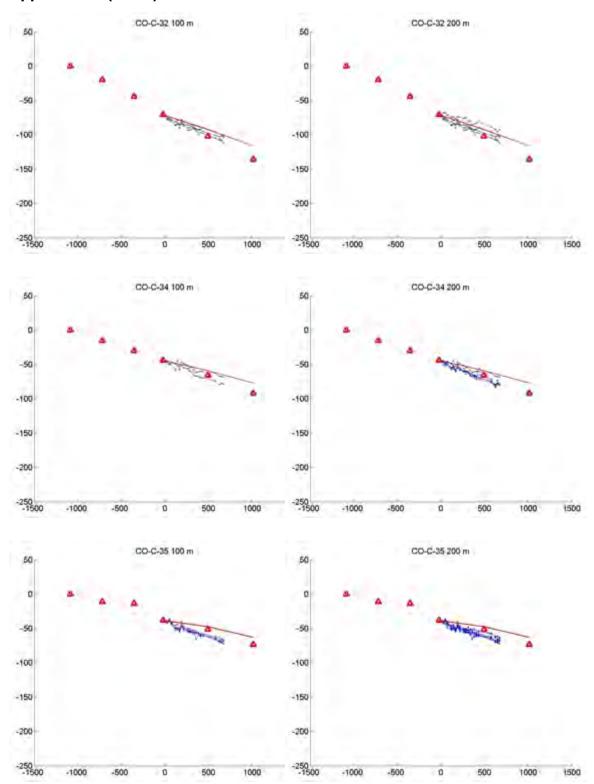




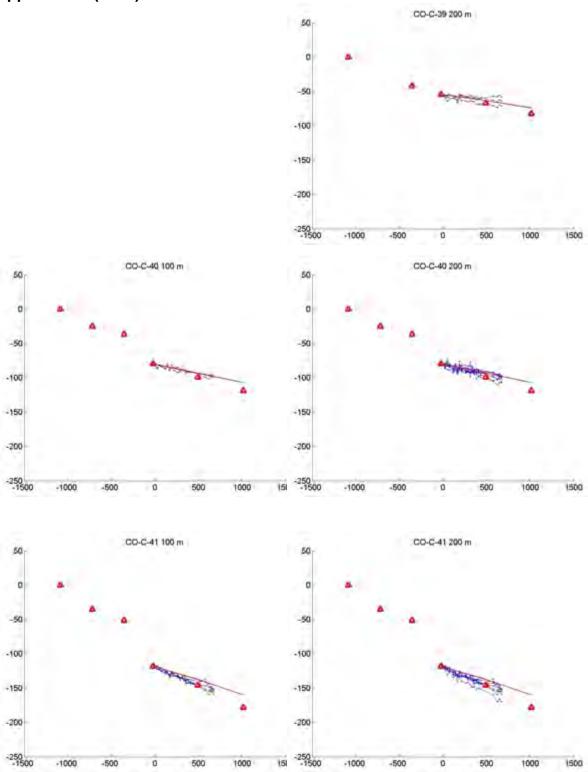


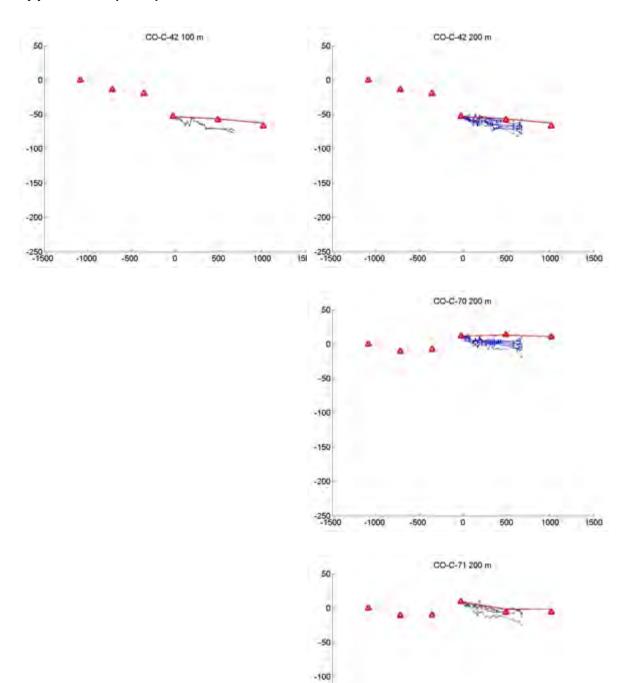
Appendix B. PSInSAR[™] results from the RADARSAT descending orbit data





Appendix B. (Cont)
Appendix B. (Cont)





-150

-200

-250

-1000

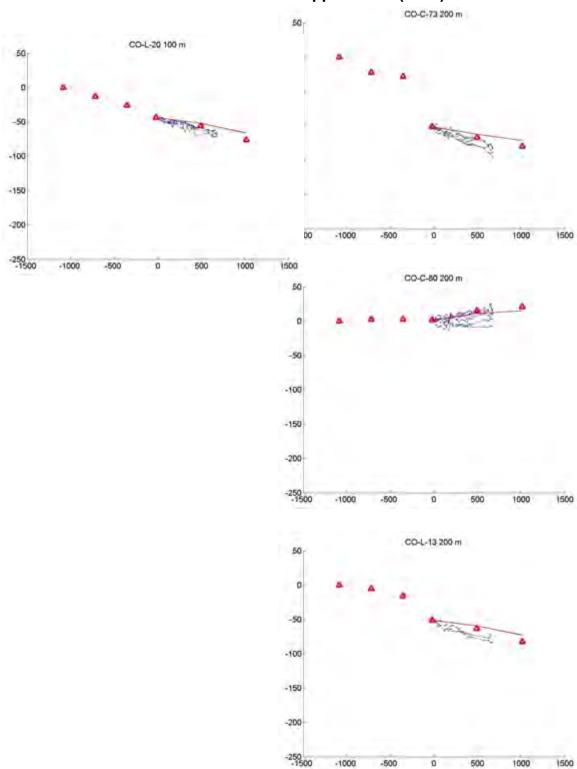
-500

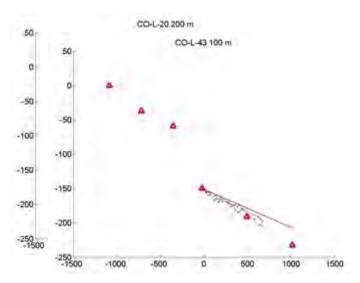
0

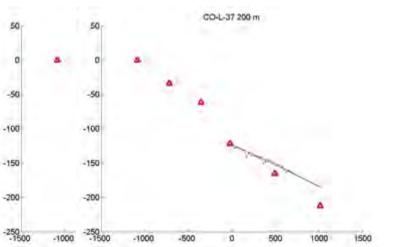
500

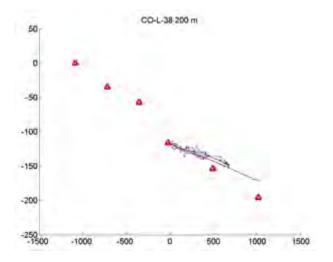
1000

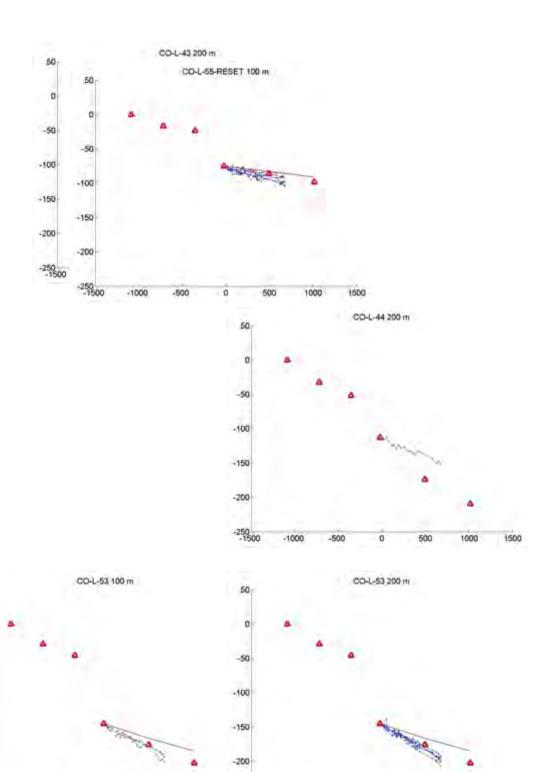
1500











-250 -1500

-1000

1000

50

0

-50

-100

-150

-200

-250 -1500

-1000

-500

0

500

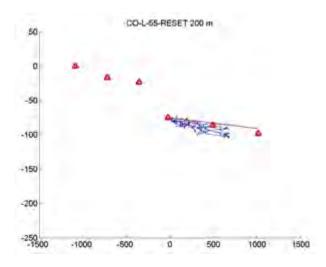
-500

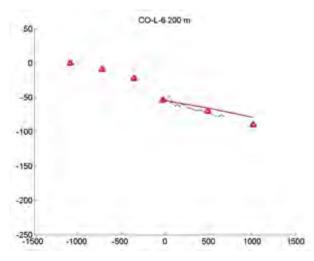
0

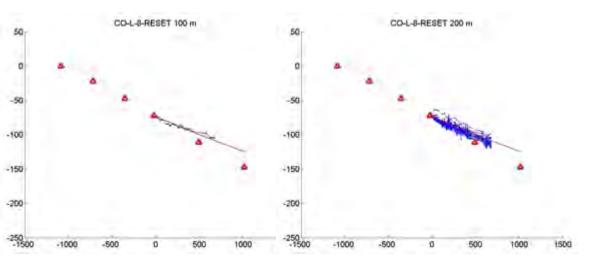
500

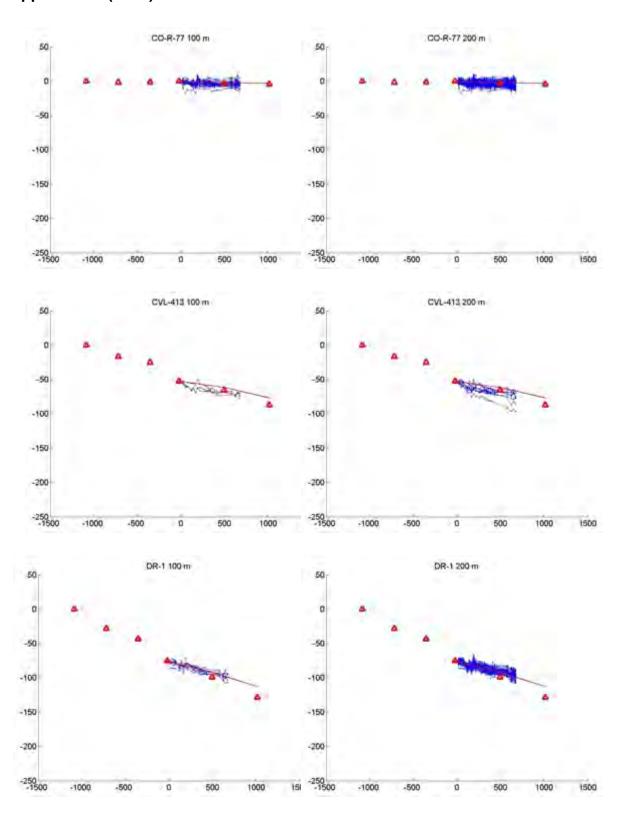
1500

1000





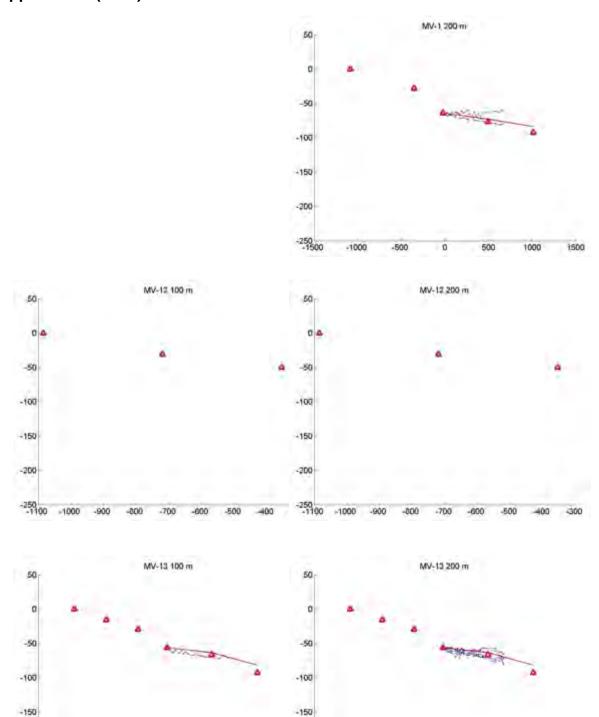




-200

-250 -1500

-1000



-200

-250 -1500

-1000

-500

0

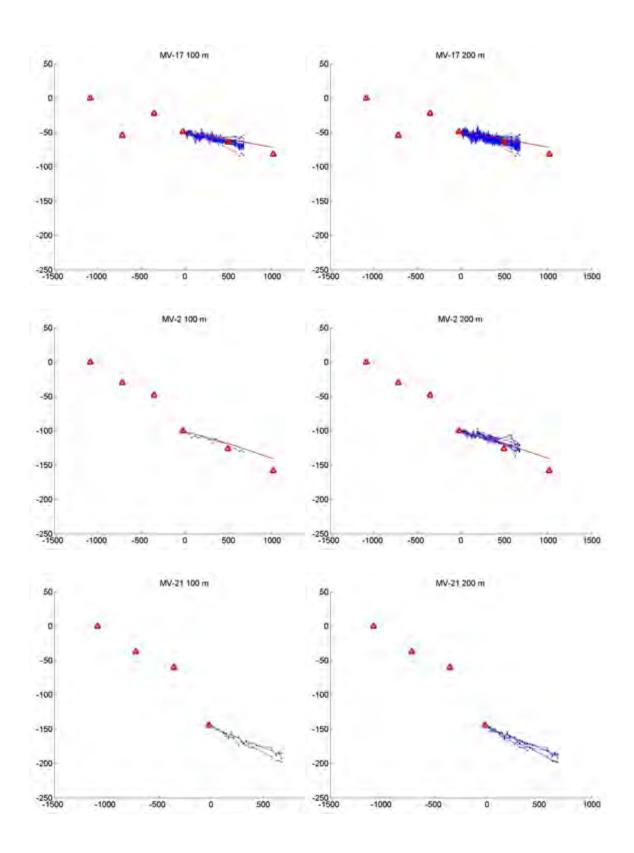
500

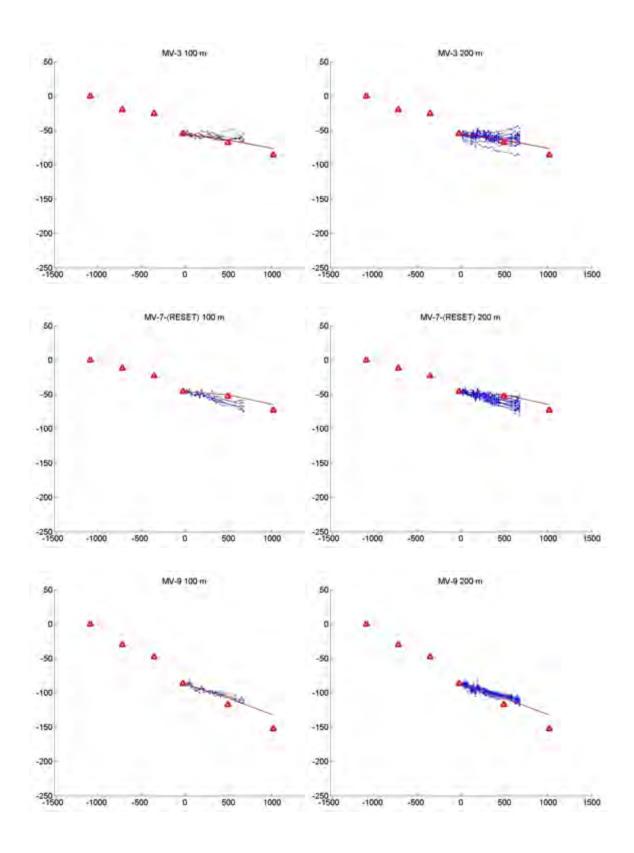
1000

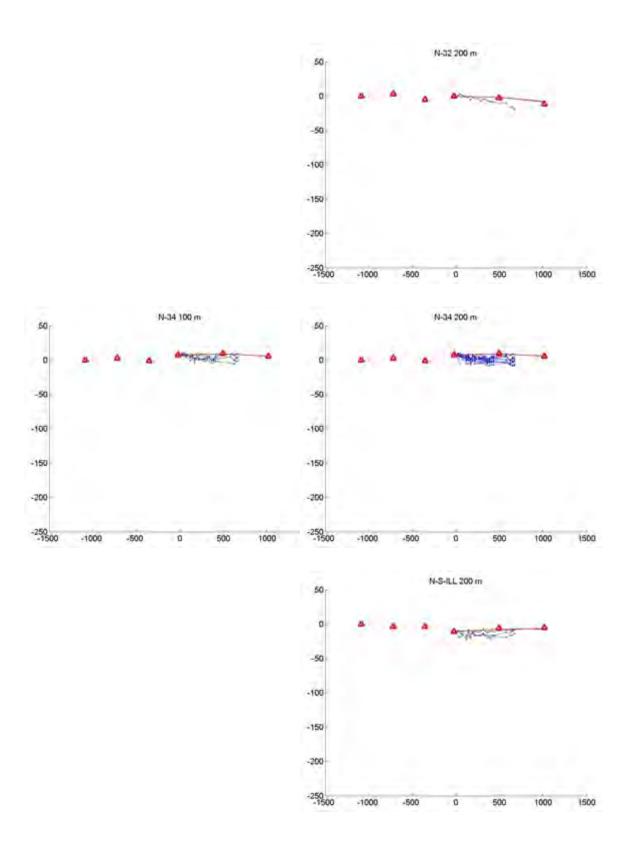
1500

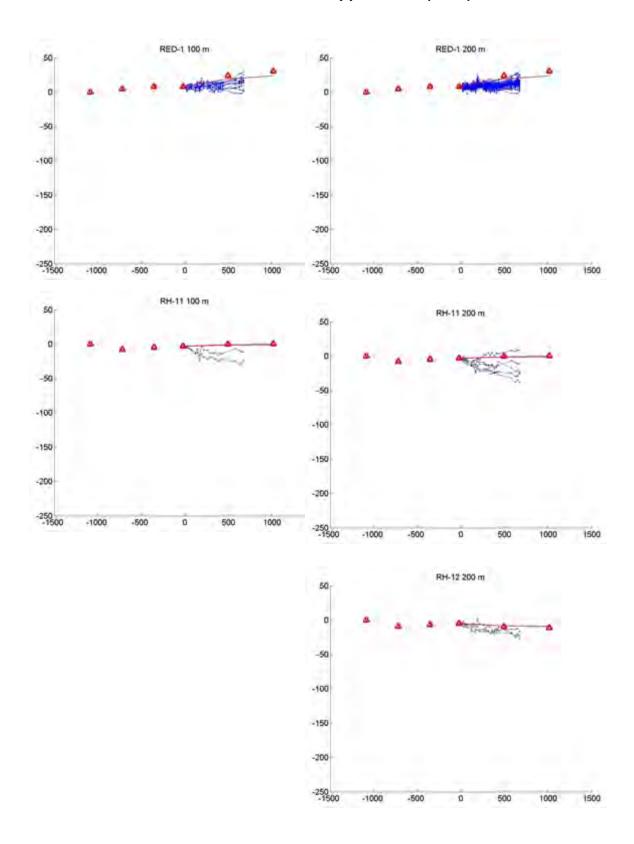
500

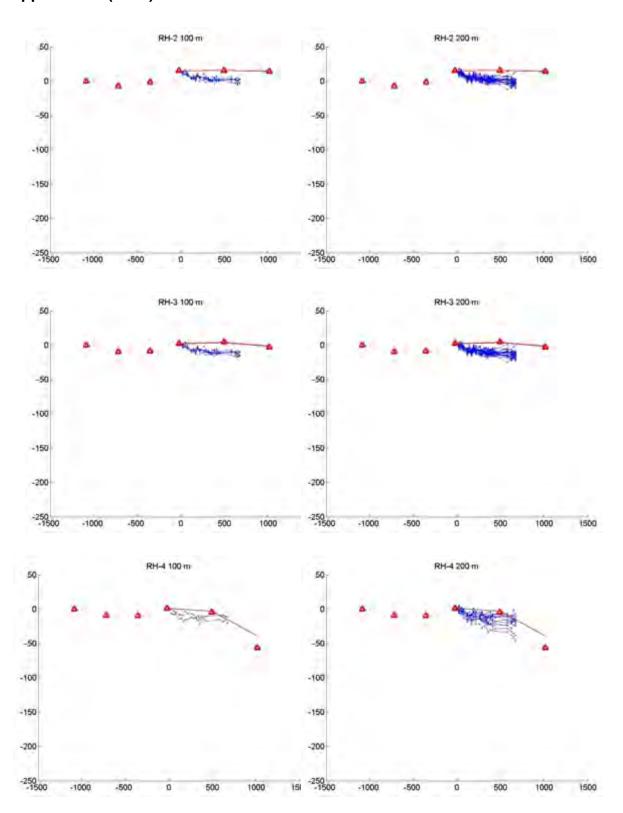
1000

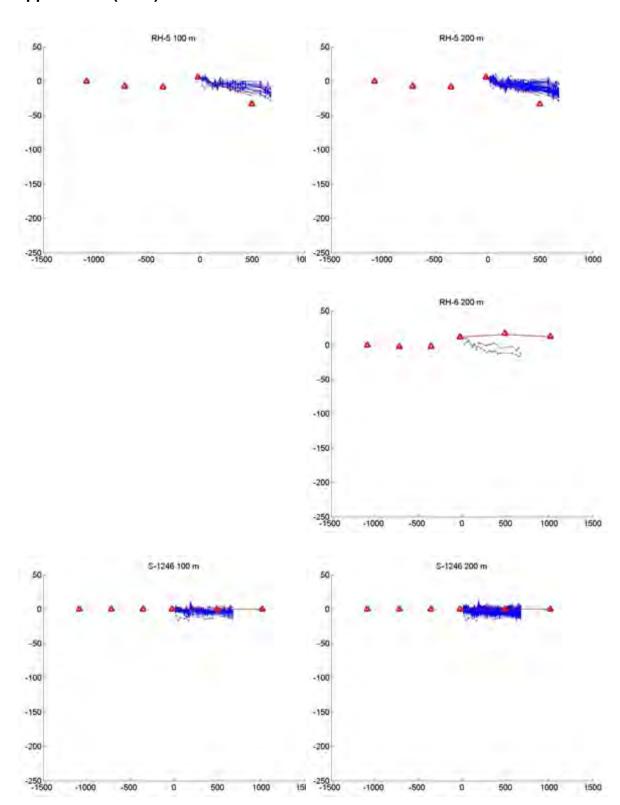


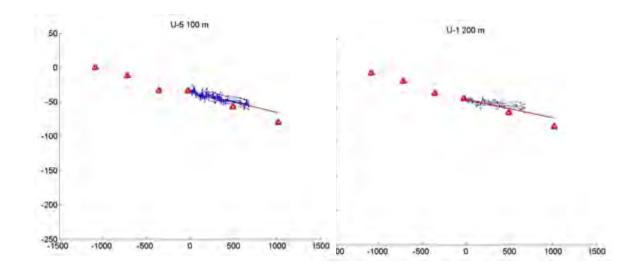


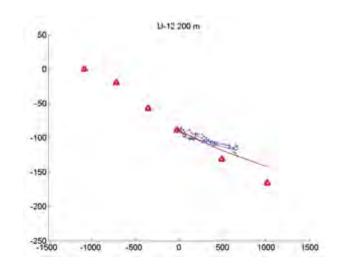


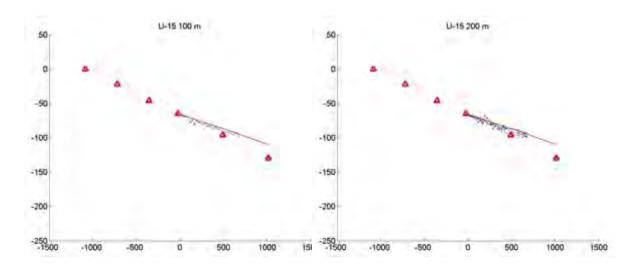


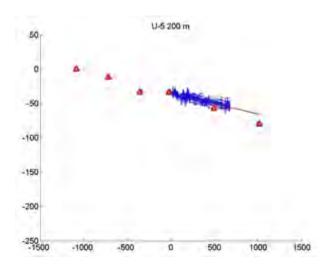


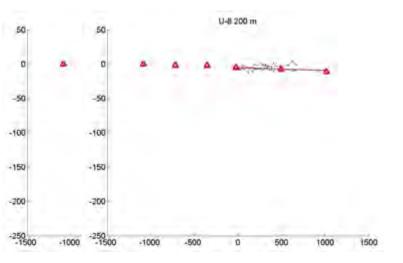


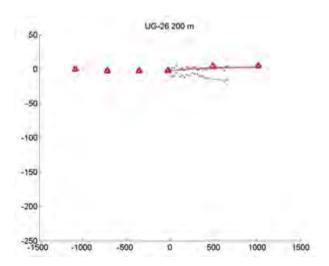












UG-70 100 m

0

500

-50

-100

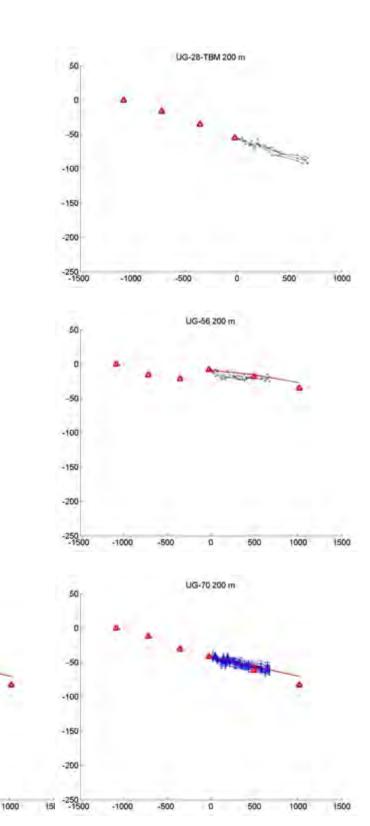
-150

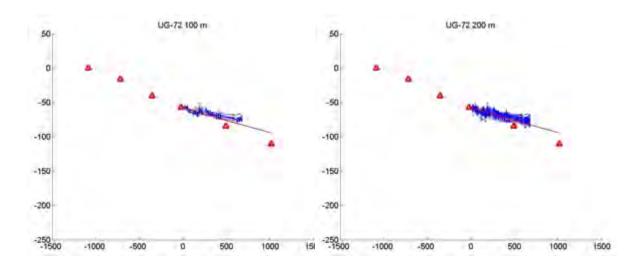
-200

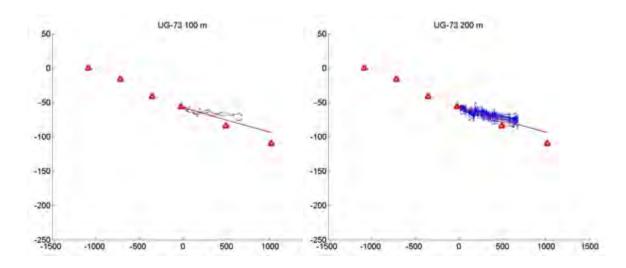
-250 -1500

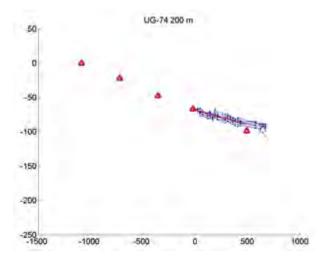
-1000

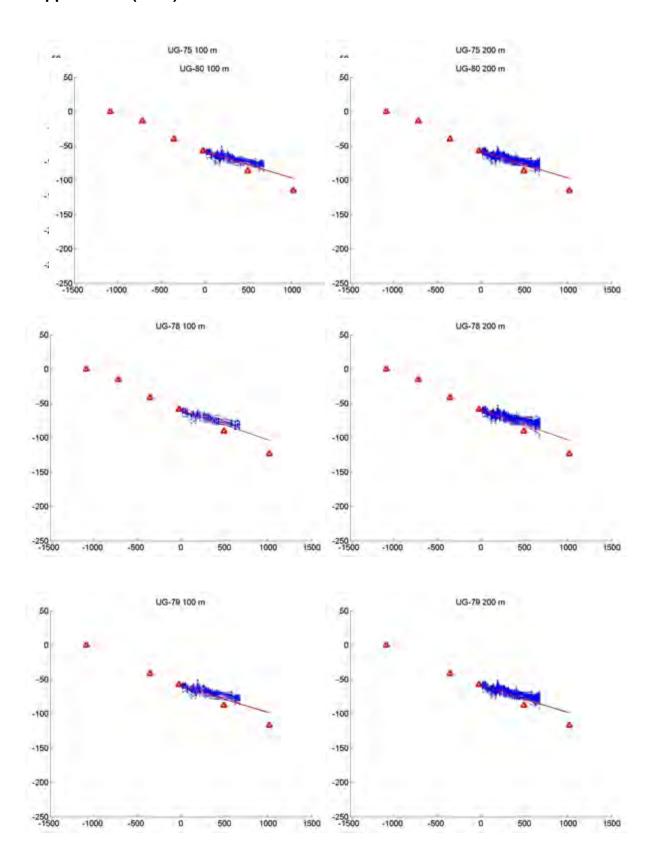
-500



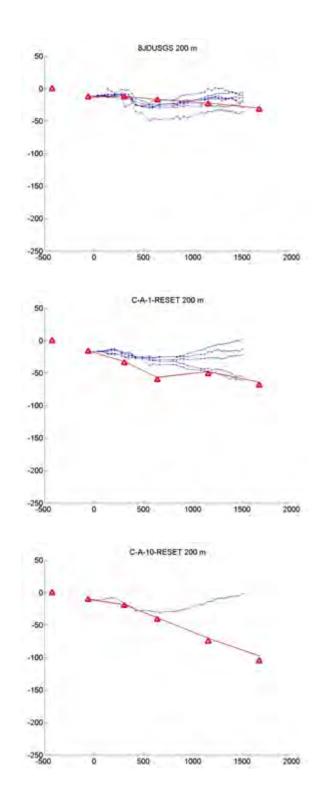


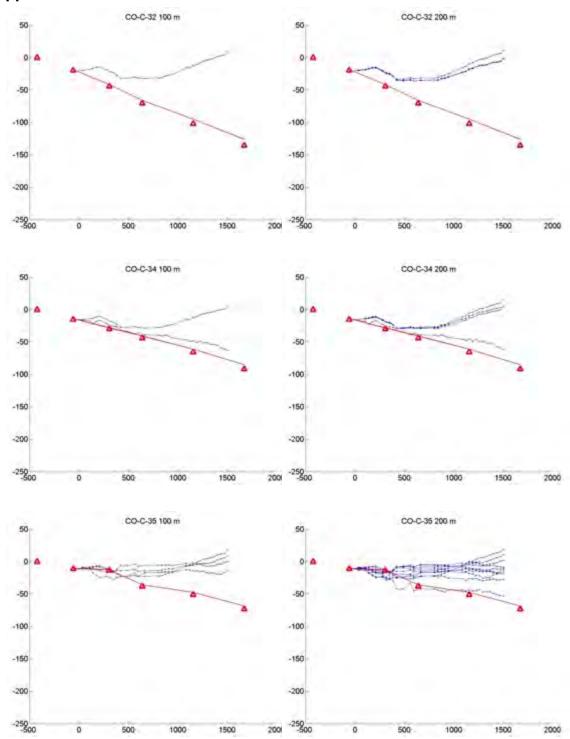


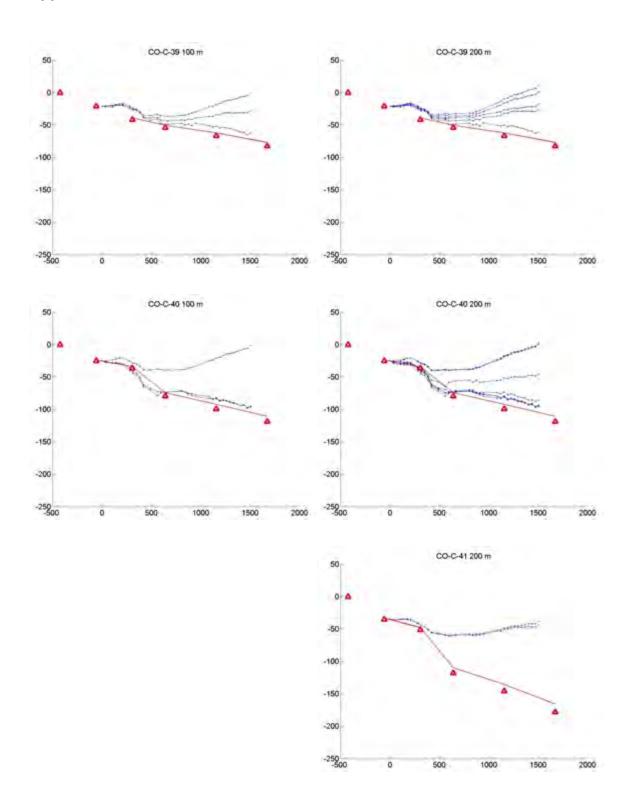


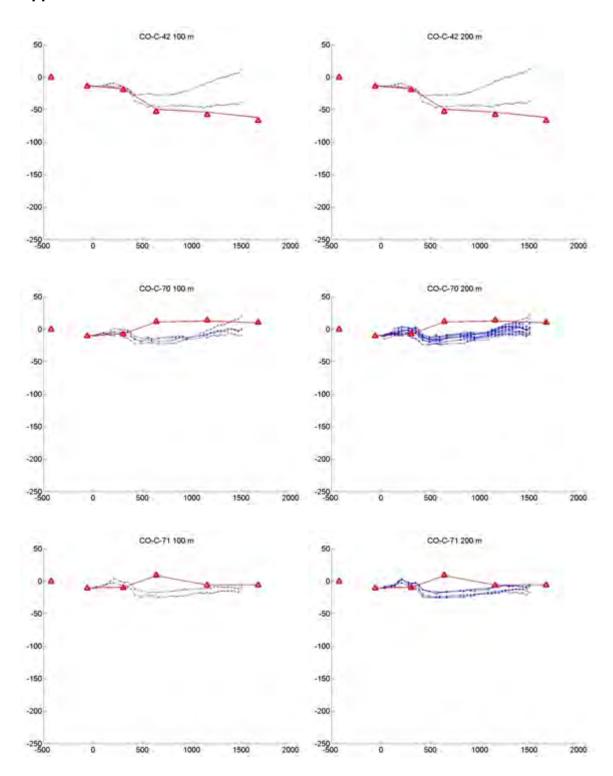


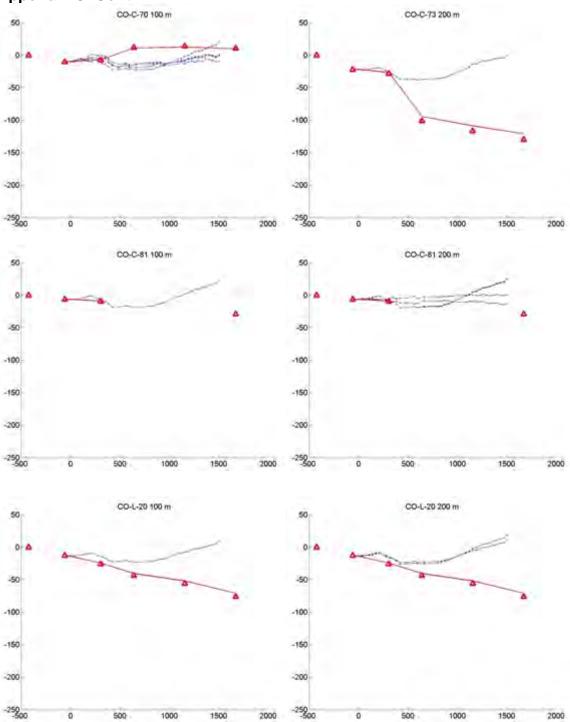
Appendix C. SBAS results from the ENVISAT ascending orbit data

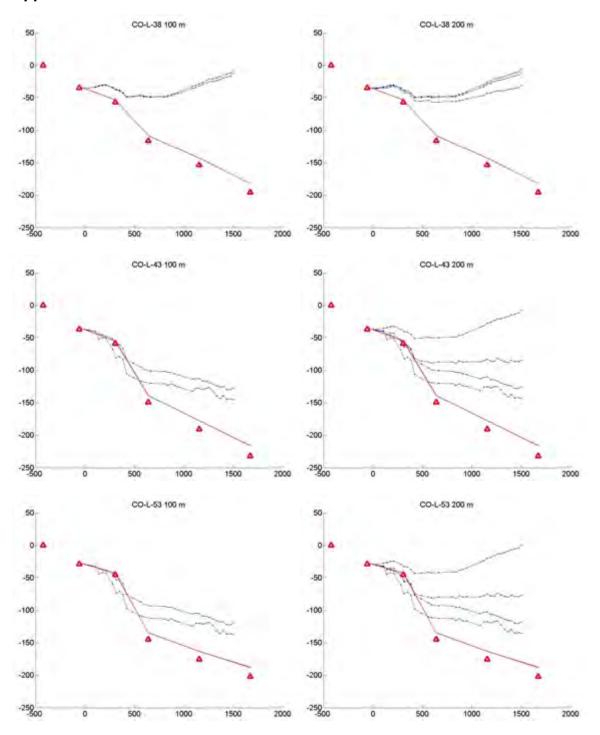


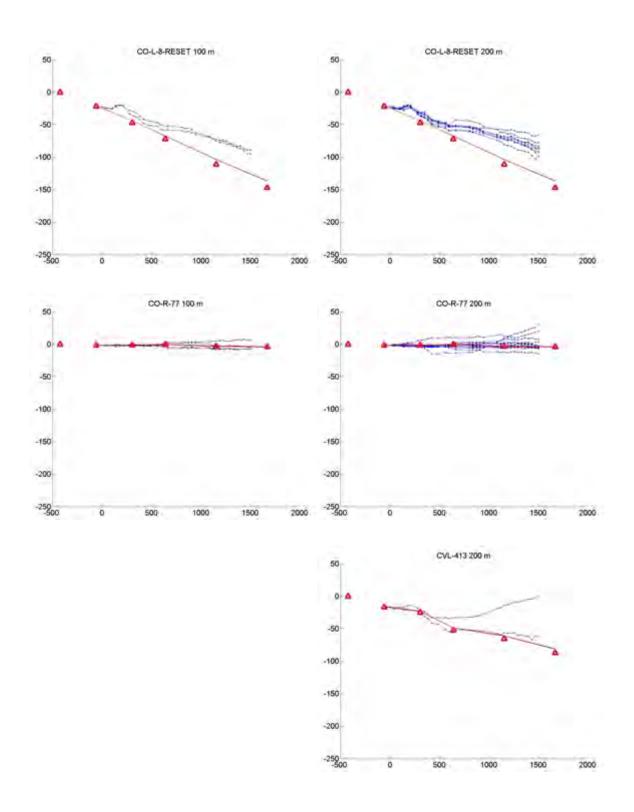


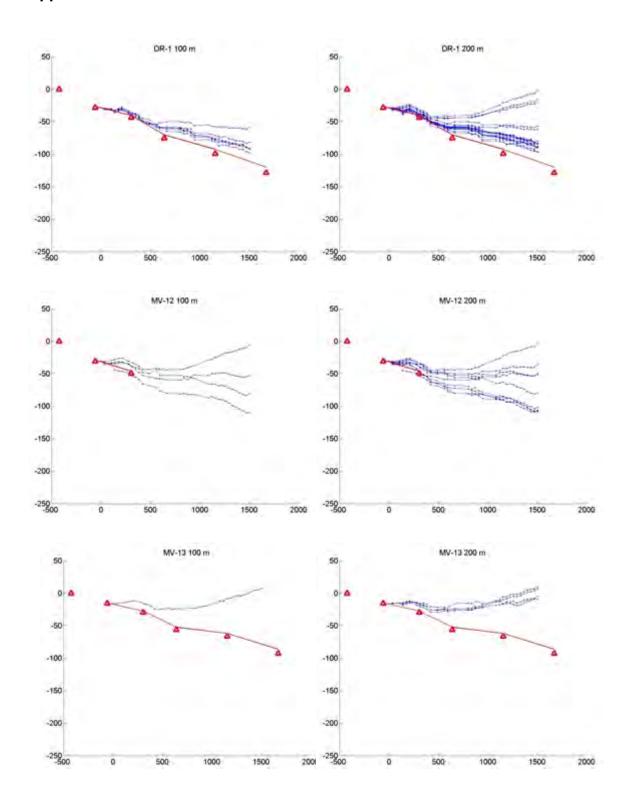


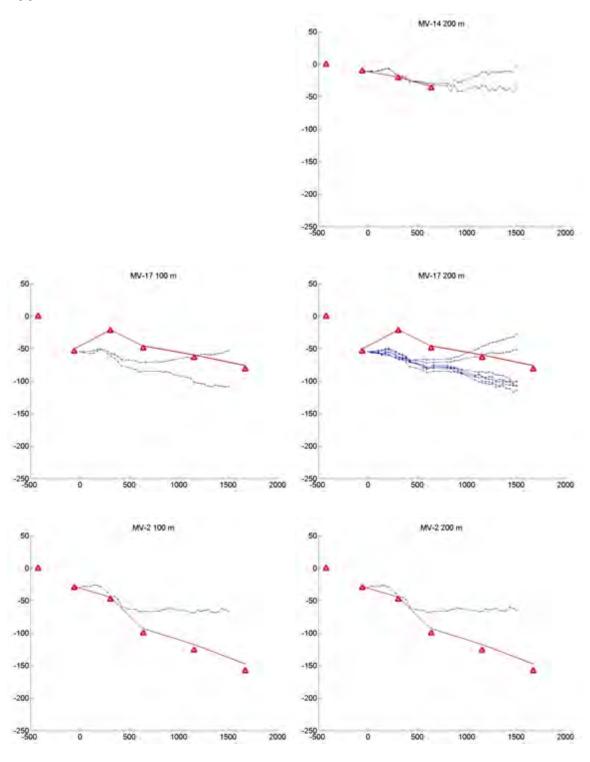


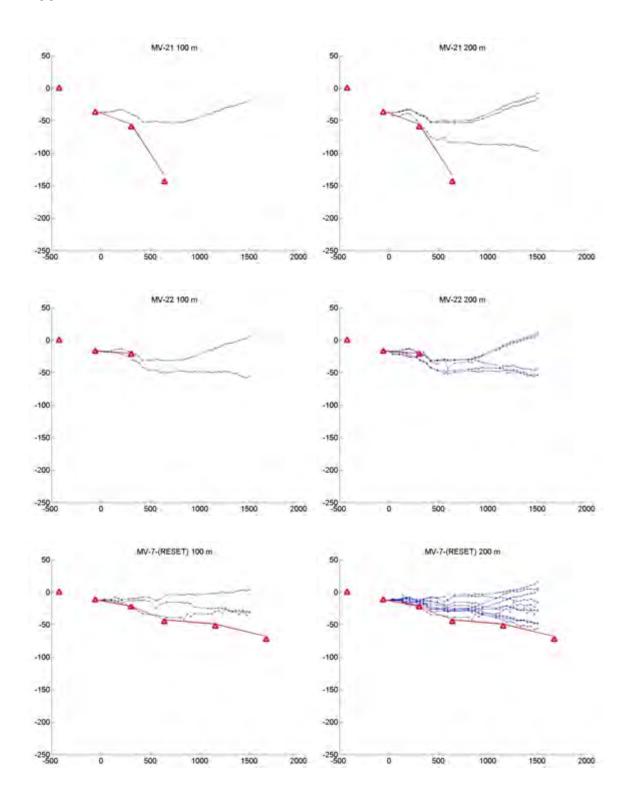


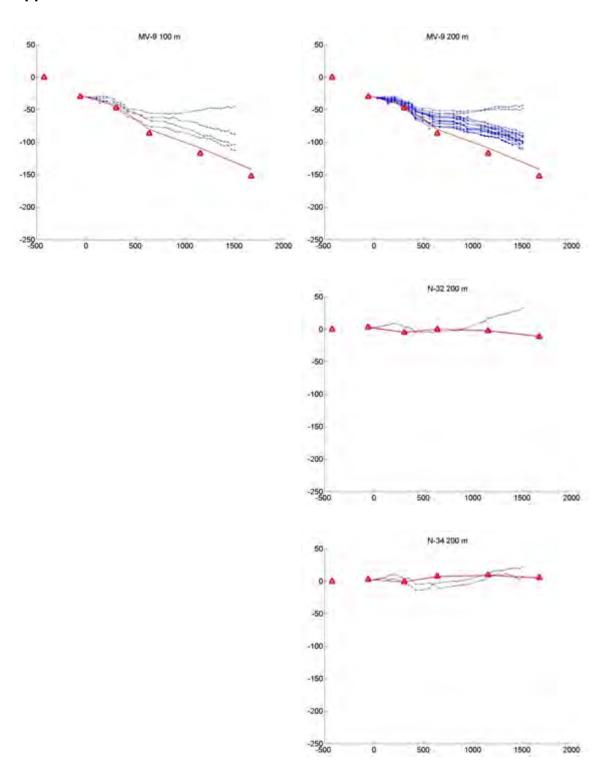


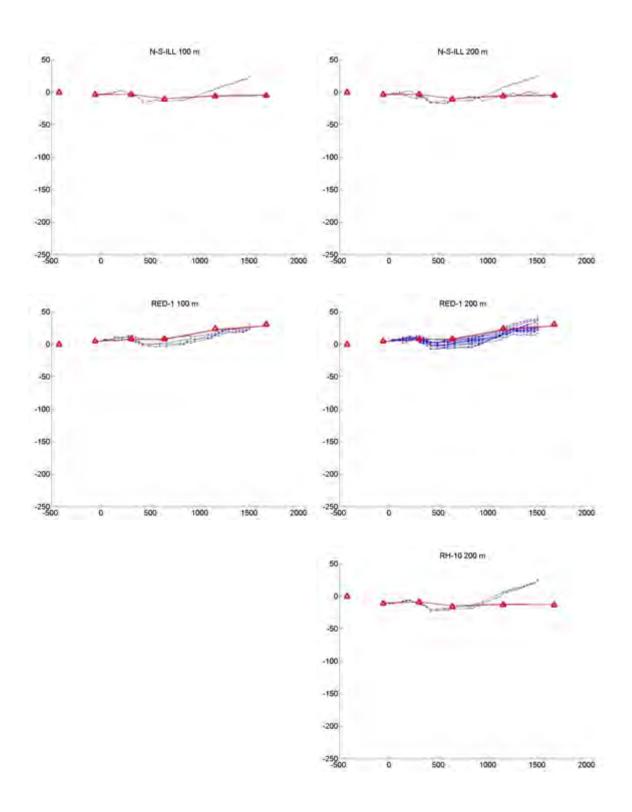


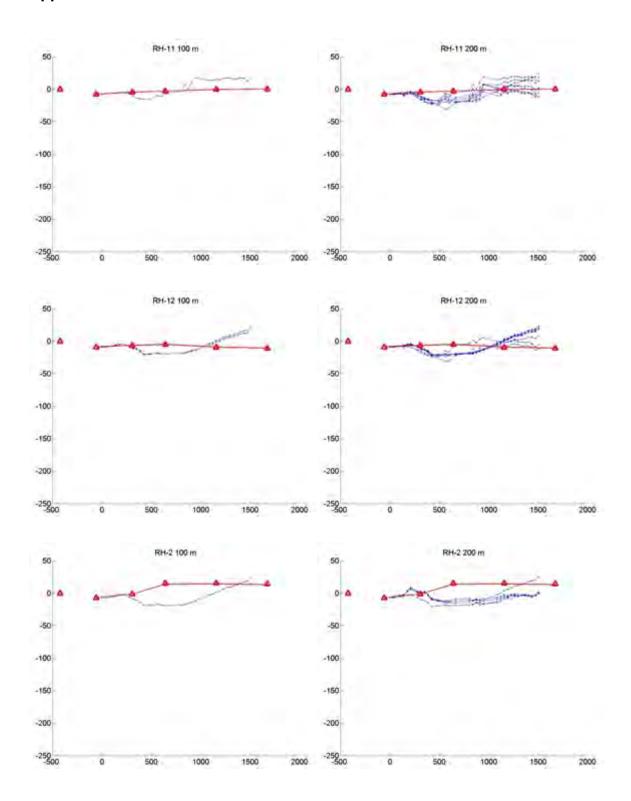


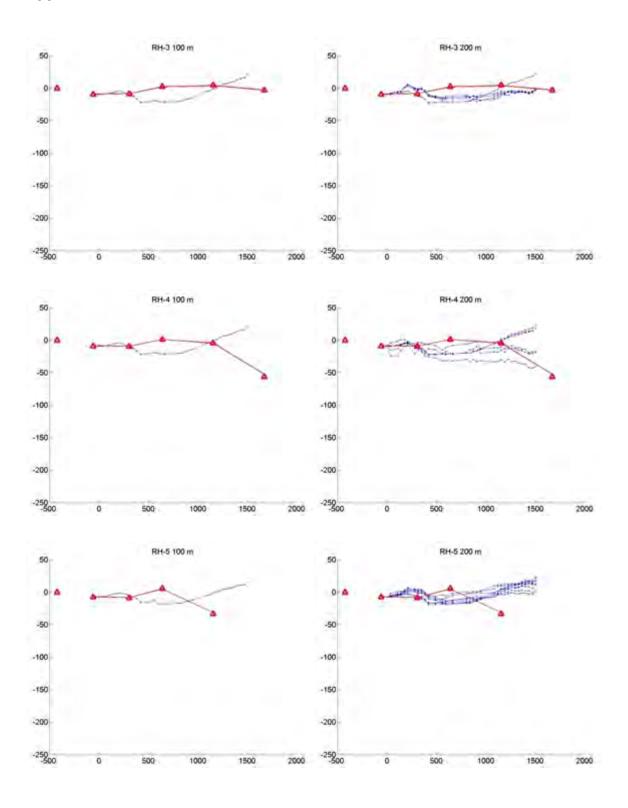


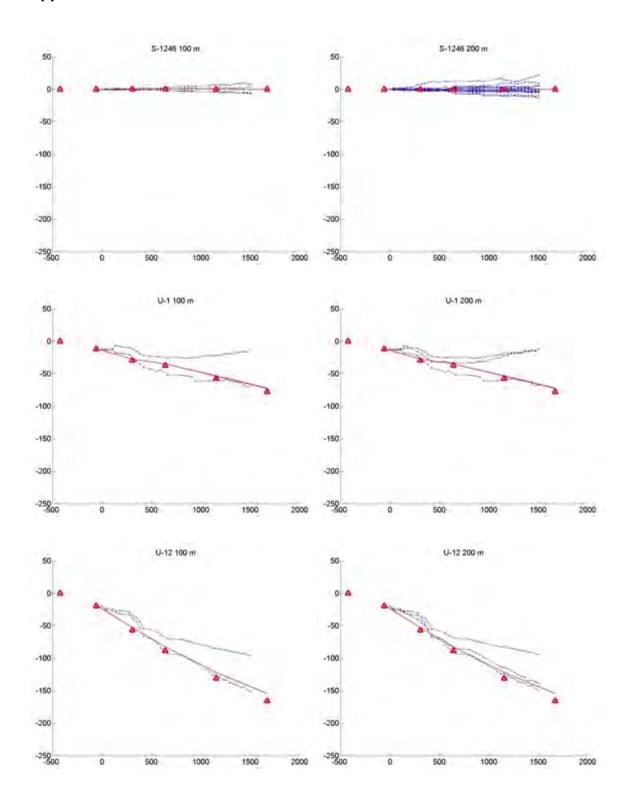


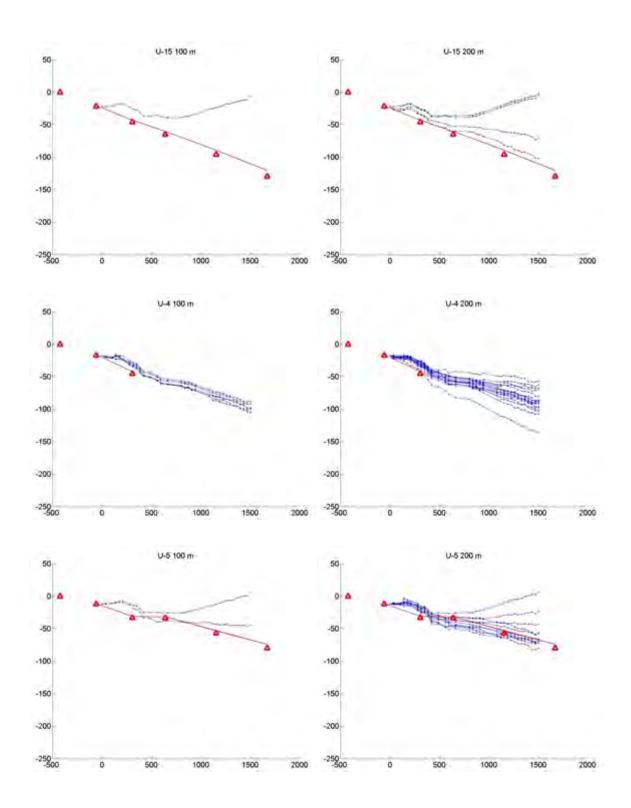


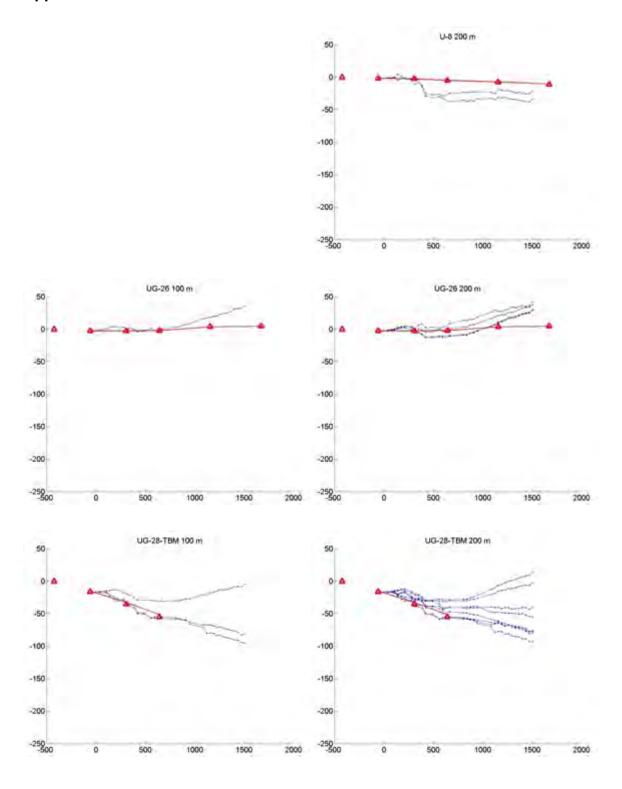


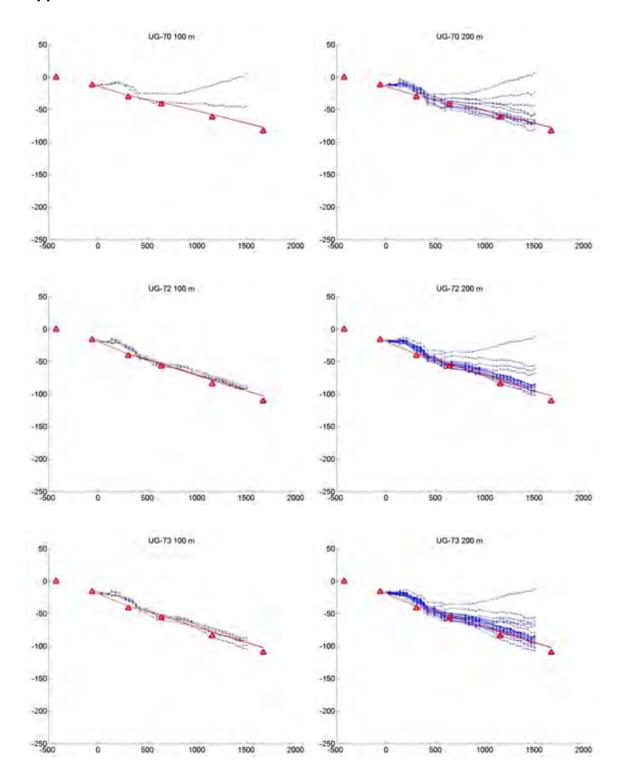


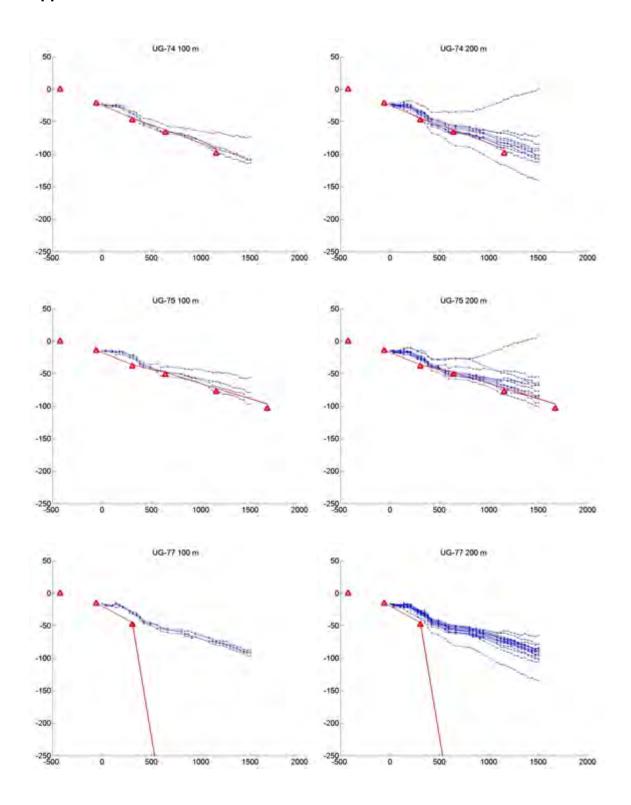


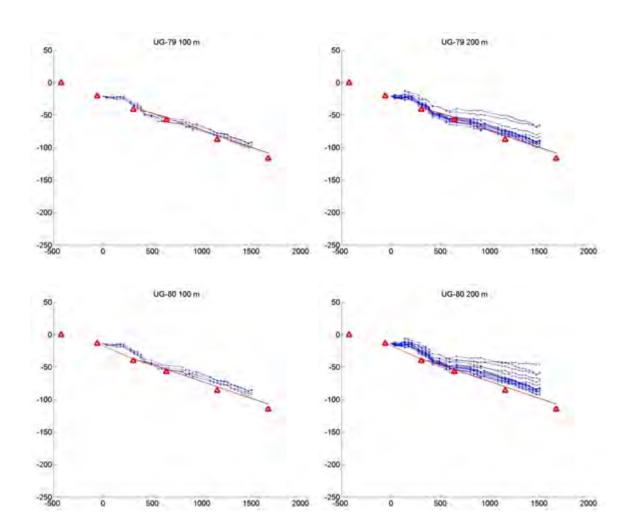












Appendix D. SBAS results from the ENVISAT descending orbit data

